

A study of high viscosity oil displacement from a curved solid in aqueous solutions

by

Rui Li

A thesis submitted in partial fulfillment of the requirements for the degree of

Doctor of Philosophy

in

Chemical Engineering

Department of Chemical and Materials Engineering
University of Alberta

© Rui Li, 2019

Abstract

The spontaneous displacement of a fluid in another immiscible one on a solid surface is essential for many technical applications, such as painting, detergency, bitumen extraction and enhancing oil recovery. This project was motivated by exploring a process of high viscosity bitumen displaced by aqueous phase over sand grains during the water-based oil sands extraction. For the experimental investigation, a microscopic control and image system was adopted to observe the microscale spontaneous displacement of high viscosity model oil droplets over highly curved surfaces in aqueous media. Relevant characterizations (e.g., the three-phase contact angle and the three-phase contact line velocity) were extracted via digital image analysis and the corresponding methodology was discussed in detail. The interfacial tension between the high viscosity oil and aqueous solutions, was determined by the drop shape relaxation method due to the difficulty of measurements using conventional techniques of tensiometry. The experimental results showed that both static and dynamic behavior of the oil displacement could be significantly changed by surface wettability alternation or surfactant addition. On the other hand, only the displacement dynamics strongly depended on oil viscosity, surface curvature, and droplet volume. An interesting observation of the dynamic droplet shape deviating from a spherical segment has been found to originate from the relative significance of the viscous stress to the capillary stress on the interface near the three-phase contact line. The quantitative data analysis using the generally accepted models of dynamic wetting indicated that the displacement dynamics could be controlled by different mechanisms at different stages, and additional mechanisms could be introduced by surfactant additions. The findings from this study are expected to improve the general knowledge of spontaneous liquid-liquid displacement as well as offer some practical implications to optimize the bitumen liberation process during industrial operations.

Preface

This Ph.D. project was conducted by the author under the supervision of Dr. Zhenghe Xu and Dr. Tony Yeung. Excluding small parts of the work mentioned below, the author was responsible for the bulk of the contribution covered in this dissertation.

- The author performed the experiments of the microscale high viscosity oil displacement using the existing modified micropipette experimental system and procedures set up by Dr. Feng Lin and Mr. Bauyrzhan Primkulov.
- The drop shape relaxation analysis for the interfacial tension measurement discussed in Chapter 5, particularly, the algorithms regarding the theoretical least square method, was instructed by Dr. Tony Yeung. The author was responsible for coding Matlab programs to implement the algorithms as well as conducting relevant experiments and data analysis.

The contribution mentioned in Chapter 6 has been published as a jointly authored paper stated below:

Li, R.; Manica, R.; Yeung, A.; Xu, Z. Spontaneous Displacement of High Viscosity Micron Size Oil Droplets from a Curved Solid in Aqueous Solutions. *Langmuir* **2019**, *35* (3), 615–627.

The contribution and discussions contained in Chapter 7 are being considered for publication and the corresponding manuscript is in preparation.

The author was responsible for the manuscript preparation, while Dr. Rogerio Manica, Dr. Tony Yeung and Dr. Zhenghe Xu were thoroughly involved in the manuscript revision.

Acknowledgments

First of all, I would like to convey my sincere gratitude to my respected supervisor Dr. Zhenghe Xu and co-supervisor Dr. Tony Yeung, who offered countless guidance and support during my entire Ph.D. study. Their insightful advice, crucial comments and inspiring encouragements help me overcome a lot of difficulties in my research. I really benefited a lot from every talk and discussion with them.

I would like to give grateful acknowledgment to Dr. Rogerio Manica for the routine in-depth discussion on my research and comprehensive instruction on my scientific writing skill. I would also emphasize his generous and patient help on the revision, correction and proofreading of my manuscript preparation.

I am grateful to Dr. Feng Lin and Mr. Bauyrzhan Primkulov who showed instructive views on my project and provided systematic training for my experimental investigation when I just started my Ph.D. project.

I really appreciate valuable comments and suggestions from Professor John Ralston who has enormous knowledge and rich experience in the field of my research.

Many thanks go to all the fellow members of our Oil Sands Research Group. Through working and sharing with them, my experimental ability was considerably improved, and my scientific view was extensively broadened as well.

I express my deepest gratitude to my family who tried their best to create a great living environment for me and provided selfless and firm support all the way during my journey to pursue my Ph.D. degree.

Last but not least, I would like to acknowledge National Sciences and Engineering Research Council of Canada (NSERC)-Industrial Research Chair (IRC) Program in Oil Sands Engineering for the financial support of my research.

Contents

Chapter 1 Introduction and motivation	1
1.1 Historical overview of wetting phenomena investigations	2
1.2 Wetting phenomena in water-based oil sands extraction	3
1.3 Objectives of this research	6
1.4 Outline of the Thesis	7
Chapter 2 Fundamentals	9
2.1 Static wetting.....	9
2.2 Dynamic wetting and singularity problem.....	11
2.3 Common approaches for wetting dynamic investigation.....	12
2.3.1 HD approach	13
2.3.2 MK approach	16
2.3.3 Combination of HD and MK approaches	19
2.3.4 Experimental validation	20
2.3.5 Limitations of these approaches.....	21
2.4 Surfactant	22
2.4.1 Basic concepts of surfactant.....	22
2.4.2 Surfactant adsorption at the interface	25
2.5 Wettability alteration in the presence of surfactant.....	27
2.5.1 Water/air/solid system	27
2.5.2 Water/oil/solid system	28
2.6 Influence of surfactant on wetting dynamics	29
Chapter 3 Experimental methods.....	32
3.1 Materials.....	32

3.1.1	Preparation of solid substrates	33
3.1.2	Preparation of surfactant aqueous solutions and the CMC determination.....	34
3.2	Viscosity measurement of the oil sample.....	35
3.3	Measurement of interfacial tension	36
3.4	Measurement of surfactant adsorption at the solid surface	37
3.5	Spontaneous microscale oil displacement tests.....	38
Chapter 4	Digital image analysis	41
4.1	Introduction	41
4.2	Methodologies of digital image analysis.....	43
4.3	Error analysis of contact angle measurement.....	46
4.4	Summary	50
Chapter 5	Drop shape relaxation analysis.....	52
5.1	Introduction	52
5.2	Axisymmetric drop shape relaxation analysis.....	55
5.2.1	Review	55
5.2.2	Theoretical calculation with boundary least squares method	56
5.2.3	Calculation results and validation.....	58
5.3	Interfacial tension measurement.....	62
5.3.1	Micrometer-sized drop shape relaxation experiments	62
5.3.2	Digitized initial drop shape extraction.....	63
5.3.3	Interfacial tension evaluations	66
5.4	Summary	68
Chapter 6	Oil displacement in pure water.....	69
6.1	Introduction and motivation.....	69
6.2	Results and discussion.....	71

6.2.1	Degree of liberation.	71
6.2.2	Non-spherical cap shape of the droplets	73
6.2.3	Dynamic contact angle.....	79
6.2.4	Quantitative description with theoretical models	81
6.3	Summary	88
Chapter 7 Oil displacement in surfactant aqueous solutions		90
7.1	Introduction	90
7.2	Results and discussions	91
7.2.1	Interfacial tension between oil and water	91
7.2.2	Adsorption of surfactants at the solid-water interface	92
7.2.3	Experimental result of oil displacement	94
7.2.4	Final static contact angle.....	95
7.2.5	Temporal evolution behavior.....	97
7.2.6	Dependence of U on θ_d	101
7.3	Summary	105
Chapter 8 Conclusions and implications.....		107
8.1	Conclusions	107
8.2	Practical implications for water-based oil sands extraction.....	108
Appendix A Numerical implementation of the BLS method		111
Bibliography		114

List of Tables

Table 2-1: Summary of the relationship between α and the corresponding mechanisms.....	31
Table 5-1: The measured interfacial tension between the high viscosity oils and water.....	68
Table 6-1: Static contact angle of N450000 on various solid surfaces with wettability modification in water.....	72
Table 6-2: Contact angles obtained using the local circle fitting methods with various pixel ratios for fitting.....	79
Table 6-3: Adjustable parameters extracted from MK and HD models	84
Table 7-1: Ultimate adsorbed surfactant densities (nmol/cm ²) on the silica sensor	93
Table 7-2: Values of θ_s (deg) in SDBS, CTAB and TX-100 solutions at different concentrations	96
Table 7-3: The ζ extracted by fitting Equation (7-5) to the experimental data points at the linear regime in Figure 7-8	104

List of Figures

Figure 1-1: Schematic of a typical water-based oil sands extraction process.	4
Figure 1-2: Conceptual steps of bitumen liberation during the water-based oil sands extraction. 5	
Figure 1-3: A simplified representation of the equilibrium of the naphthenic acid in an immiscible hydrocarbon-water system.	6
Figure 2-1: Schematic of a typical gas-liquid-solid three phase system and the interfacial tensions between the respective two phases.	10
Figure 2-2: Schematics of (a) forced wetting and (b) spontaneous wetting	12
Figure 2-3: Schematic of three hypothetical regions of moving meniscus in Cox’s hydrodynamic analysis.....	14
Figure 2-4: Schematic of the microscopic elementary motion described in the MK approach... 16	
Figure 2-5: Schematics of the major four categories of surfactants based on the ionic group of hydrophilic head.....	23
Figure 2-6: Schematics of structures of surfactant micelles in (a) aqueous and (b) oil media. ...	25
Figure 3-1: General molecular structures of high viscosity polybutene oil.....	32
Figure 3-2: Molecular structures of (a) SDBS; (b) CTAB; and (c) TX-100 (n=9-10).	33
Figure 3-3: (a) A tapered end glass tip produced by hot wire pipet puller; (b) a glass tip with a microscale spherical cap.	33
Figure 3-4: The plot of measured surface tension vs. logarithmic concentration of surfactants. 35	
Figure 3-5: Schematic of viscosity measurement with a rotational rheometer.....	36
Figure 3-6: Measured viscosities of the high viscosity oil samples at the various shear rate	36
Figure 3-7: Photograph of micropipette system.	39
Figure 3-8: Photograph illustrating the sample delivery to the spherical cap surface of the glass tip.	39

Figure 3-9: Snapshots of oil droplet receding on a solid surface in aqueous solution. The solid red lines indicate the arc length ($2r_c$) of the droplet wetted area on the curved surface between the TPCL lines observed from the side view image at an experimental time (t). The subscript 0 for r_c in (a) denotes the initial time ($t = 0s$).	40
Figure 4-1: Schematic of contact angle determination by $\theta/2$ method	42
Figure 4-2: Visual demonstration of some critical steps during the digital image analysis.	44
Figure 4-3: Visual demonstration of the contact measurement for the case of low TPCL velocity by adopting (a) the circle fitting, (b) local circle fitting and (c) apex circle fitting algorithms....	45
Figure 4-4: Visual demonstration of the contact measurement for the case of high TPCL velocity by adopting (a) circle fitting, (b) local circle fitting and (c) apex circle fitting algorithms.....	45
Figure 4-5: The detected edge profiles by adopting various $N_{threshold}$. The zoomed region of the meniscus near the TPCL enclosed in the red square is shown in the inset.	46
Figure 4-6: The measured contact angles by adopting various threshold grayscale intensities for the edge detection	47
Figure 4-7: Images of the displaced oil droplet at the same state captured using exposure times of (a) 10 ms; (b) 35 ms; (c) 60 ms; (d) 85 ms; (e) 135 ms; (f) 160 ms; (g) 185 ms and (h) 210ms. The exposure time for the image in Figure 4-5 is 110 ms.....	48
Figure 4-8: The contact angles measured from the captured digital images at different exposure time.	49
Figure 4-9: Images of the displaced oil droplet at the same state captured under out-of-focus conditions, where the location of the objective lens was shifted from the on-focus one in (a) -2 mm; (b) -4 mm; (c) $+2$ mm and (d) $+4$ mm. The on-focus image is shown in Figure 4-5	49
Figure 4-10: The contact angles measured from the digital images captured at different location of the objective lens as shown in Figure 4-9	50
Figure 5-1: The process of a highly deformed drop breakup.	53
Figure 5-2: The process of a gently deformed drop retraction.	54

Figure 5-3: The theoretical drop profile at several dimensionless times during the relaxation from an initial spheroid shape using the BLS method.....	59
Figure 5-4: The results of two self-consistent checks for the BLS method: (a) the dimensionless drop volume in the calculation changes as function of t_c and (b) the plots of the dimensionless length of the drop on symmetric axis (H) versus t_c obtained in the calculations with adopting different Δt_c for the Euler-type integration.	60
Figure 5-5: Comparison between the temporal evolution of D_d/D_{d0} calculated from the BLS method and that predicted from Equation (5-4) at various viscosity ratios.....	61
Figure 5-6: The theoretical drop profile at several dimensionless times during the relaxation from an initial shape of (a) “flower” and (b) spherocylinder using the BLS method.	62
Figure 5-7: Snapshots illustrating the micrometer-sized oil drop shape relaxation in the micropipette system.	63
Figure 5-8: Visual demonstration of some major steps to extract the experimental drop shape from the digital image for the BLS method. The zoomed region of the directly extracted drop profile at the apex is shown in the inset of (d).	64
Figure 5-9: The calculated numerical curvature along the nodal points. The detailed description of the evaluation of J_c refers to Appendix A	65
Figure 5-10: Comparison of the extracted drop profile without and with smoothing process from (a) an overall view and (b) an enlarged view at the apex.	66
Figure 5-11: The theoretical drop profile at several dimensionless times during relaxation from the extracted initial shape from the experiment with performing the BLS method.....	67
Figure 5-12: Determination of the interfacial tension by matching experimental data with the theoretical curve obtained by the BLS method.....	67
Figure 6-1: Semi-logarithmic plots of D_L versus time under variable experimental conditions: (a) surface wettability, (b) oil viscosities, (c) surface curvatures and (d) oil volumes. The error bars are not presented for clarity.	73

Figure 6-2: Demonstration of the deviation of the dynamic drop shape from a spherical cap on the snapshot of the oil displacement experiment. The zoomed region of the meniscus shape near the TPCL enclosed in the red square is shown in the inset..... 75

Figure 6-3: Comparison of dynamic contact angles determined using four different approaches for the same oil receding process..... 75

Figure 6-4: Deviation factor as a function of displacement time with various (a) surface wettability and (b) oil viscosities. 78

Figure 6-5: Snapshots of receding oil droplet configurations at the time with maximum deviation factor on a set of surface with variable wettability, showing progressive less deviation of the oil droplets on increasingly high hydrophobicity of solid surfaces: (a) $\theta_s=28^\circ$; (b) $\theta_s=39^\circ$; (c) $\theta_s=58^\circ$; (d) $\theta_s=91^\circ$ and (e) $\theta_s=104^\circ$ 78

Figure 6-6: Best local fit of circles with various pixel ratios in fitting of local oil droplets for the ε values of the droplets to be (a) 2.93% and (b) 0.24%. 80

Figure 6-7: Cosine functions of local dynamic contact angles as a function of the TPCL speed at various surface (a) wettability, (b) oil viscosities, (c) surface curvatures and (d) oil volumes: symbols for the experimental results and solid lines from the MK model for comparison..... 83

Figure 6-8: (a) Plot of ζ versus μ of oil based on the results of viscosity study and (b) plot of $\ln(\zeta/\mu)$ versus W_a obtained from wettability study, both showing anticipated relationship predicted by Blake's theory. 85

Figure 6-9: g function of extrapolated dynamic contact angles as a function of the TPCL speed at various surface (a) wettability, (b) oil viscosities, (c) surface curvatures and (d) oil volumes: symbols representing experimental results and lines the prediction by the HD model for comparison. The straight line represents the best fitting using the least square method on the data points over the velocity region where the data appeared visually linear. 87

Figure 7-1: Interfacial tensions between high viscosity oil N190000 and surfactant aqueous solutions at different surfactant concentrations 92

Figure 7-2: Monitored (a) frequency and (b) dissipation shifts of the QCM-D silica sensor at the third overtone caused by surfactant adsorption. 93

Figure 7-3: Temporal evolution of r_c/r_{c0} during oil displacement in (a) SDBS, (b) CTAB and (c) TX-100 solutions. 95

Figure 7-4: Temporal evolution of $(r_{c0} - r_c)/r_{c0}$ during oil displacement in (a) SDBS and (b) CTAB solutions. The straight lines indicate best fits to **Equation (7-2)** at the early stage. 98

Figure 7-5: Coefficients B and α in **Equation (7-2)** extracted from the linear fit at the early stage of the oil displacement. 99

Figure 7-6: Schematic representation of the Marangoni flow in the oil droplet caused by a spatial variation of surfactant adsorption along the oil-water interface. 100

Figure 7-7: The dynamic interfacial tension of hydrocarbon oil (heavy paraffin oil) against (a) SDBS and (b) TX-100 aqueous solutions at various concentrations measured by the theta optical tensiometer using the pendant drop method. 101

Figure 7-8: Cosine function of the experimental dynamic contact angle as a function of the TPC line velocity obtained from the oil displacement experiments with (a) SDBS and (b) TX-100 addition. The solid lines indicate the best fit of the data points which could be governed by the linear MK model. 103

Figure 7-9: The logarithm of the contact line friction coefficients normalized by oil viscosity versus the reversible work of adhesion. The black dash line represents the best fit of Blake's correlation to the data points of surfactant concentration below the CMC. 105

Figure A-1: The schematic of a drop profile (blue line) characterized by a series of nodal points in the numerical procedure. 112

List of Symbols

ΔG_μ	Energy barrier for molecular jumping arising from fluid viscosity
ΔG_0	Energy barrier for one molecular jumping at equilibrium
ΔG_S	Energy barrier for molecular jumping arising from solid-fluid interaction
μ	Viscosity
A	Oil-solid contact area
a, b	Principal semi-axis of a spheroid
c_l	Surfactant concentration in the subsurface
Ca	Dimensionless capillary number
c_b	Concentration of surfactant molecules in the bulk
C_B	Mass sensitivity
D	Dissipation factor
dc	Contact surface radius
D_d	Deformation parameter
D_L	Degree of oil liberation
D_S	Surfactant diffusivity in the solution
f	Resonant frequency
F_d	Driving force acting on TPCL
h	Planck constant
H	Length along a symmetric axis
h_A	Apex height
J_c	Mean curvature of interface
K	Net frequency of molecular jumping
K_0	Frequency of molecular jumping at equilibrium
k_B	Boltzmann constant
L	Macroscopic length
L_C	Characteristic length
L_S	Microscopic cut-off length
m	Mass

n	Overtone number
N_A	Avogadro's number
n_{\max}	Maximum order in numerical analysis
n_p	Total number of nodal points
$N_{\text{threshold}}$	Relative threshold grayscale intensity
p	Pressure
R_C	Radius of best fitting circle
R_d	Radius of drop as a sphere
R_e	Equivalent radius
r	Half arc length of droplet wetted area
R_m	Radius of curved solid substrate
S	Spreading coefficient
T	Absolute temperature
t	Time
T	Normal stress on the interface arising from interfacial tension
t_c	Dimensionless time
U	Velocity of TPCL
U_i	Initial TPCL velocity
\mathbf{v}	Velocity field
V_L	Volume of unit flow
V_o	Volume of oil droplet
W_a	Reversible work of adhesion
γ	Interfacial tension
Γ	Surface excess concentration
γ_C	Critical surface tension of surface
γ_{LG}	Liquid-gas interfacial tension
γ_{os}	Oil-solid interfacial tension
γ_{ow}	Oil-water interfacial tension
γ_{SG}	Solid-gas interfacial tension

γ_{SL}	Solid-liquid interfacial tension
ε	Deviation factor
ε_{\max}	Maximum deviation factor
θ_d	Dynamic contact angle
θ_0	Equilibrium contact angle
$\theta_{d,H}$	Macroscopic dynamic contact angle
$\theta_{d,M}$	Non-equilibrium dynamic contact angle
θ_f	Final contact angle
θ_m	Microscopic contact angle
θ_s	Static contact angle
λ	Mean distance between two nearest thermal activated sites
μ_e	Viscosity of exterior fluid
μ_i	Viscosity of interior fluid
ζ	Coefficient of contact line friction
σ_e	Hydrodynamic traction from exterior phase
σ_i	Hydrodynamic traction from interior phase
σ_M	Marangoni stress
φ	An angle defined to be equal to r_L/R_m
Π, A_n, B_n, C_n, D_n	Arbitrary constant

List of Abbreviations

AC	Alternating current
ADSA	Axisymmetric drop shape analysis
ADSA-D	Axisymmetric drop shape analysis-diameter
ADSA-EF	Axisymmetric drop shape analysis-electric field
ADSA-NA	Axisymmetric drop shape analysis-no apex
AFM	Atomic force microscopy
BIM	Boundary integral method
BLS	Boundary least squares
CCD	Charge-coupled device
CMC	Critical micelle concentration
CTAB	Hexadecyltrimethylammonium bromide
DBP	Di-n-butylphthalate
DCDMS	Dichlorodimethylsilane
EOR	Enhanced oil recovery
HD	Hydrodynamic
HLB	Hydrophilic lipophilic balance
MK	Molecular kinetic
OMCTS	Octamethylcyclotetrasiloxane
PET	Polyethylene terephthalate
PMMA	Polymethylmethacrylate
PTFE	Polytetrafluoroethylene
QCM-D	Quartz crystal microbalance with dissipation monitoring
SDBS	Sodium dodecylbenzenesulfonate
TIFA	Theoretical image fitting analysis
TPCL	Three-phase contact line
TX-100	Triton TM X-100

Chapter 1

Introduction and motivation

Wetting describes how one fluid interacts with a substrate surface in the presence of another immiscible fluid. Originally, water was the primary fluid concerned in this phenomenon, but recently, it has been expanded to more general fluids. A fluid can be regarded as the wetting phase if it exhibits a strong affinity toward the surface; on the contrary, it is called a nonwetting phase when the affinity is weak. Most common three-phase systems of wetting are seen as liquid-gas-solid or liquid-liquid-solid systems, and systems with three fluid phases could also be found in some situations.[1] [2]

In principle, wetting behavior could be classified into two categories: static and dynamic wetting. The static wetting focuses on the configurations of the wetting system with immobile three-phase contact line (TPCL) where the three phases meet; the dynamic wetting phenomena could occur as the TPCL moves with respect to the substrate surface. Both wetting phenomena have been extensively studied since they are closely relevant to our daily life and crucial to numerous industrial processes. Relevant examples include ink delivered by printer spreading on paper, coating functional films on the top of the surface, pesticide distribution on the plant leaves, removing dirt on the surface by detergent, extracting natural oil from porous media and water drainage from highways, to name a few.

In what follows, a brief history of the investigations on wetting phenomena is presented. Subsequently, an industrial application of water-based oil sands extraction process, which is strongly relevant to the wetting phenomenon, is discussed in detail. The motivation for gaining a better understanding of this specific application constitutes the overall objectives of this Ph.D. project.

1.1 Historical overview of wetting phenomena investigations

More than 200 years ago, British scientist Thomas Young[3] worked out a theoretical description on an ideal wetting system at a static equilibrium state, which is also known as Young's equation. Since then, extensive research has been conducted both theoretically and experimentally to further explore the fundamental principles of wetting. In the late 1860s, Athanase Dupre[4] introduced a concept to quantify the strength of the interaction between two different phases. Based on Young's equation, he also derived the famous Young-Dupre equation for the direct evaluation of that strength. In 1964, American chemist William Zisman[5] carefully examined the experimental data of the contact angles and proposed a retraction method to determine a critical parameter to characterize the solid surface.

With respect to the history of the static wetting investigation, the study on wetting dynamics starts relatively late. The pioneering work of wetting dynamics was found in Huh and Scriven's 1971 paper[6]. This paper uncovered a significant challenge on the investigation of wetting dynamics due to a theoretical singularity in the classical hydrodynamic description, and thereafter inspired extensive studies in this field. In the past several decades, endeavors have been made to figure out reasonable mechanisms that could alleviate the singularity issue and gain insight into the physics of the TPCL. For instance, rolling motion of spreading droplet[7] and slippage on the surface[8] were proposed in 1974 and 1984, respectively. In 1975, Hoffman[9] discovered that all the data from his dynamic wetting experiments could be correlated by a master curve on a single plot and indicated the potential existence of a universal description of the dynamic wetting behavior. Later, in 1979, an explicit mathematical expression given by Tanner[10] successfully quantified the dynamic behavior of wetting observed from the experiments. To date, more mathematical models for dynamic wetting quantifications have been developed. Among them, the molecular kinetic (MK) model originated from Blake and Haynes's theoretical description[11] in 1969 and the hydrodynamic (HD) model based on the hydrodynamic analysis of Cox[12] in 1986 are considered to be the most influential ones and have been widely used in recent theoretical investigations. More recently, thanks to the rapid development of computational technology, the molecular dynamics simulation has provided an alternative tool to explore the field of wetting dynamics.

Currently, wetting, especially wetting dynamics, is still an active field of research, despite the extensive study for many decades. Searching relevant publications of recent 10 years (from 2008

to 2018) archived in the Web of Science database with keyword “wetting dynamics”, 13111 results are returned. The most influential review in this field by Pierre-Gilles de Gennes[13], a Nobel Prize laureate in physics, has been cited more than 2000 times during the past 10 years. Several hot topics, such as wetting on rough surfaces[14] [15], volatile liquid wetting[16], dynamics of non-Newtonian fluid wetting[17] [18], nanofluid spreading[19] and superspreading phenomena of surfactant solutions[20] [21] have attracted more investigators into this field.

1.2 Wetting phenomena in water-based oil sands extraction

Canadian oil sands that are mainly located in northern Alberta are considered as one of the major recoverable natural oil resources over the world.[22] A high-efficient and low-cost technique of exploration along with the production of oil from oil sands is desperately needed to provide reliable energy supply for the future. Alberta oil sands are sedimentary deposits, or mixture, consisting of unconsolidated mineral solids, water and ultra-heavy oil known as bitumen.[23] The main component of the mineral grains in Alberta oil sands is quartz sands and the bitumen commonly deposits on the grain surface in the reservoir condition. Depending on the bitumen content in the ore, the oil sands ore could commonly be divided into three categories, including rich grade ore (12-14 wt.% bitumen), average grade ore (10-11 wt.% bitumen) and lean grade ore (6-9 wt.% bitumen). Compared to the conventional crude oil, the bitumen is characterized by an extremely high viscosity ($\sim 10^3$ Pa·s at room temperature) and thereby low mobility. As a consequence, the production of the bitumen from the oil sands turns out to be a challenging process.

The water-based oil sands extraction, which originates from the hot water separation process developed by Clark[24], has been demonstrated as an effective technique for the extraction of the bitumen from the oil sands. Currently, it is widely used in commercial operations of processing oil sands ore mined in shallow deposits.[25] A typical operation of the water-based oil sands extraction contains several elementary steps summarized as follows:

- The oil sands ore is mined and transported to an extraction plant.
- The bitumen is separated from the mined ore in hot water solution with additives.
- The liberated bitumen attaches to air bubbles and forms bitumen froth.
- The bitumen froth is collected on the top of separation vessels due to the buoyancy effect.

- The solids, water and unrecovered bitumen left in the extraction plant are rejected into tailing ponds for further treatments.
- The bitumen froth is treated by solvents in a froth treatment plant for removal of the water and solids in the froth.
- The bitumen obtained from the froth treatment plant is upgraded to synthetic crude oil.

A generalized schematic for the entire process is given in **Figure 1-1**.

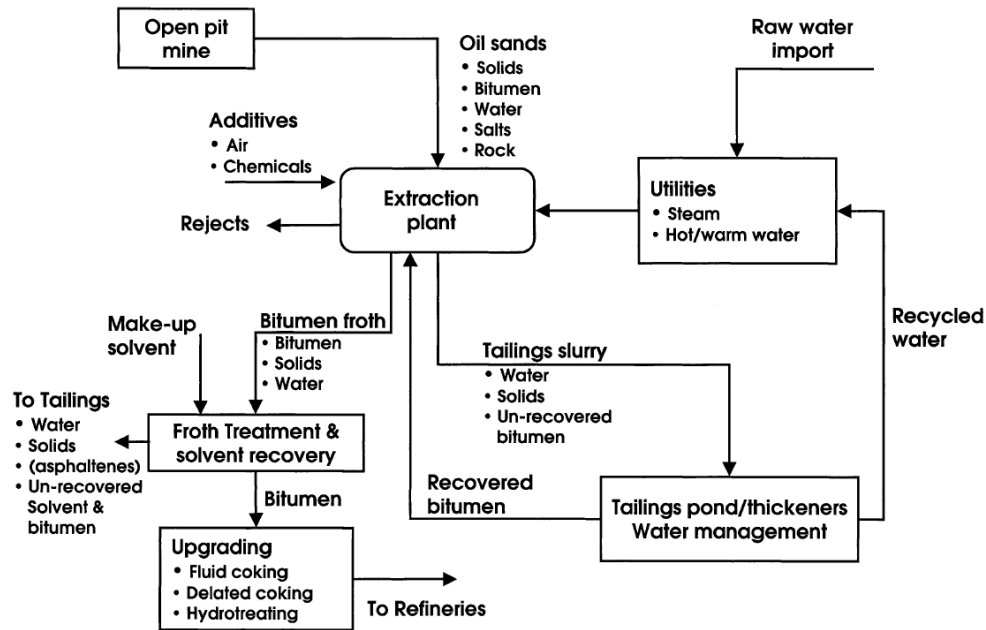


Figure 1-1: Schematic of a typical water-based oil sands extraction process.[25]

For the water-based oil sands extraction, one of the key steps is the disengagement of the high viscosity bitumen layer from its host sand grain surface in aqueous surroundings. This step is also called as bitumen liberation. As illustrated by **Figure 1-2**, during the bitumen liberation, a bitumen/water/solid TPCL is established at a pinning point caused by the rupture of the thin bitumen film due to the hydrodynamic flow of the surrounding aqueous phase. Subsequently, in most cases, the aqueous phase could displace the bitumen on the solid surface until reaching another state where the bitumen could be readily detached from the solid surface spontaneously or with the aid of hydrodynamic forces. It could be seen the bitumen liberation process is highly relevant to the wetting phenomenon, i.e., the wetting of the aqueous solution or the dewetting of the bitumen on the solid surface. Thus, the process is believed to be controlled by physicochemical properties, in particular interfacial properties of the bitumen-water-solid system.

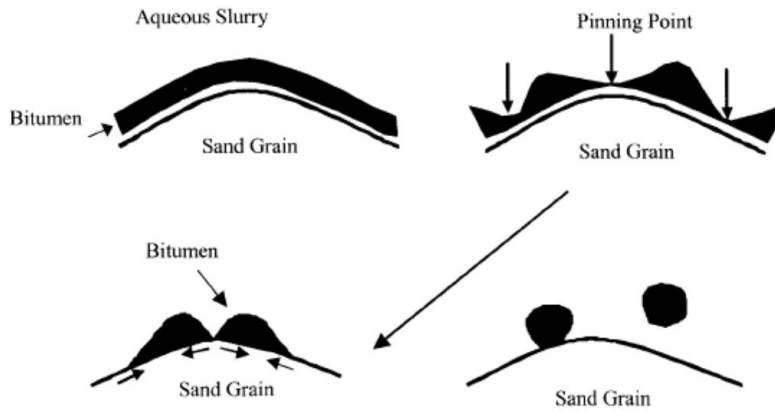


Figure 1-2: Conceptual steps of bitumen liberation during the water-based oil sands extraction.[26]

In light of the practical production experience of water-based oil sands extraction, it was found that alkaline chemicals addition could facilitate bitumen liberation. Although the exact mechanism of the benefit is still not fully understood, a popular hypothesis is that the natural surfactant in the bitumen is released into the aqueous phase at a high pH condition, which gives a reasonable explanation.[27] It is reported that major surface-active species contained in bitumen are naphthenic acids which are categorized as a group of cycloaliphatic carboxylic acids (RCOOH).[23] [27] The typical carbon number of the cycloaliphatic structure with saturated cyclopentane or cyclohexane rings (R) in naphthenic acids varies from 10 to 50.[28] In a simple immiscible hydrocarbon-water binary system as shown in **Figure 1-3**, the undissociated form of the naphthenic acid is favored to exist in the hydrocarbon phase. However, at increased pH environment, the chemical reaction equilibrium of the naphthenic acid described in **Figure 1-3** could shift towards the right and generate more naphthenic acids of ionized form dissolved in the aqueous phase. For the oil sands extraction, such process often refers to the natural surfactant release since the dissociated naphthenic acids are more interfacially active than the undissociated form.[28] Hence, the bitumen liberation behavior is likely to be modified under the influence of the released natural surfactant into the aqueous phase.

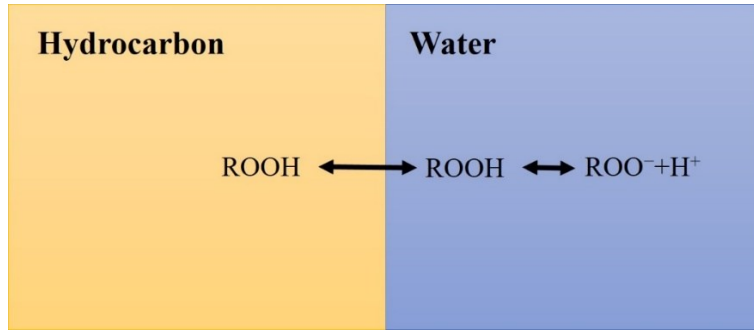


Figure 1-3: A simplified representation of the equilibrium of the naphthenic acid in an immiscible hydrocarbon-water system.

Generally speaking, an improvement of the ultimate bitumen liberation degree from the thermodynamic view is a strategy of achieving higher bitumen recovery during the water-based oil sands extraction process. On the other hand, faster bitumen liberation is beneficial for saving the processing time of production. Thus, a comprehensive study on both wetting statics and dynamics of an oil/water/solid system is necessary to further understand this critical bitumen liberation process and offer practical guidance for optimizations of the industrial production.

1.3 Objectives of this research

This Ph.D. project aims to explore the behavior of spontaneous liquid-liquid displacements. To distinguish other displacement systems investigated previously and establish a closer link to the bitumen liberation during the water-based oil sands extraction process, the project focuses on a microscale system involving an oil phase with extremely high viscosity and curved solid surfaces. To circumvent the disadvantage of using bitumen as the oil phase for the experimental investigation, which includes difficulties of identifying influential factors due to its complicated components and inconsistent experimental results caused by the unexpected reaction with air, pure high viscosity model oil which is stable in air is used in this study. The main objectives of this research are summarized as follows:

- Use an optical method to investigate the static and dynamic behavior of the microscale spontaneous oil-water displacement under the influence of several system parameters, such as solid wettabilities, oil viscosities, surface curvatures, oil volumes and surfactant types and concentrations.

- Develop an automatic method on the digital image analysis to process large volumes of image-based raw data and carry out comprehensive image analysis.
- Determine the interfacial tensions between the high viscosity oil and aqueous phase solutions which is difficult to measure from conventional techniques of tensiometry.
- Perform quantitative analysis of the data from the displacement experiments to understand the physics and physical chemistry related to the motion of the TPCL.
- Provide practical implications of the bitumen liberation in the industrial process and improve the general knowledge on the spontaneous wetting dynamics.

1.4 Outline of the Thesis

Chapter 2 introduces the fundamental knowledge in connection with the wetting phenomena. The difficulty of investigating the dynamics of wetting with the classic transport theory is mentioned. Several approaches, which are popular for the quantitative investigation of the wetting dynamic behavior, are thoroughly reviewed. Furthermore, the knowledge regarding surfactant-added wetting systems, including basic concepts of surfactant, adsorption behavior at interfaces, wettability alterations and surfactant-induced additional mechanisms on dynamic wetting behavior, are also covered in this chapter.

Chapter 3 describes the materials and experimental apparatus that are used for the examination of the high viscosity oil displacement behavior in this study. The experimental characterizations of the relevant properties of materials, such as viscosity, interfacial tension and adsorption of surfactant at a solid, are discussed as well.

Chapter 4 elaborates on the methodologies of the digital image analysis associated with three algorithms for the contact angle determination implemented in this study. A quantitative error analysis of the contact angle measurement is also performed to estimate the potential errors arising from some influential factors. The findings from that analysis give an implication of a suitable operational condition for the image-based contact angle determination.

Chapter 5 introduces an unconventional interfacial tension measurement technique that could be exclusively applicable to the system involving high viscosity liquid in this study. The numerical algorithms for the theoretical evaluation, experimental approach and methodology of the data

processing, which constitutes several indispensable parts for the application of this technique, are presented in detail.

Chapter 6 focuses on the investigation of the high viscosity model oil displaced by clean water without chemical additives. Various system parameters consisting of solid wettabilities, oil viscosities, surface curvatures and oil volumes are explored experimentally to understand their effects on the spontaneous oil displacement behavior. The dynamic shape of the microscale droplet and the relevant issues on the dynamic contact angle determination are also covered. Popular molecular kinetic and hydrodynamic approaches for the dynamic wetting investigation are also applied to analyze the corresponding experimental data and shed light on the fundamental mechanisms of the moving TPCL.

Chapter 7 presents a study of a more complicated displacement behavior in the presence of surfactant. Three types of surfactant aqueous solutions at different concentrations are used in the investigation. The data analysis is performed to obtain the contributing role of surfactants on the oil displacement and indicates some possible interpretations of the dynamic behavior in the presence of surfactants.

Chapter 2

Fundamentals

2.1 Static wetting

When a drop of water is deposited on a clean glass surface, it tends to completely spread out and ultimately form a thin water layer on the surface; however, if a Teflon surface replaces the clean glass surface, the spreading of the water drop could only reach a limited extent and be stuck on the surface. Based on these two final static configurations of water drop on the surface, the wetting behavior could be divided into two regimes including complete and partial wetting. For the complete wetting, a fluid could spread on a substrate surface to form a thin layer between the surface and another fluid. In the case of the partial wetting, a specific liquid drop shape could be formed on a surface associated with a finite equilibrium contact angle (θ_0) at the TPCL. The value of θ_0 provides a reliable evaluation of the wettability, which is a measure of the tendency of a fluid to spread on a solid surface surrounded by another immiscible fluid. As a simple example, good wettability is often indicated by a small contact angle of a specific fluid phase and vice versa. Thereafter, for convenience, the term “wettability” appearing in this dissertation refers in particular to the wettability with respect to an aqueous phase.

The configuration of the wetting system at the static state largely relies on the relevant interfacial properties. For a simple gas-liquid-solid system (see **Figure 2-1**), a spreading coefficient (S), which is a common criterion to distinguish the complete and partial wetting, is defined as,[29]

$$S = \gamma_{SG} - \gamma_{SL} - \gamma_{LG} \quad (2-1)$$

where γ_{SG} , γ_{SL} and γ_{LG} are interfacial tensions between solid-gas, solid-liquid and liquid-gas, respectively. Complete and partial wetting is likely to occur when the system is characterized by positive and negative S , respectively.

On an ideal solid substrate surface, the equilibrium contact angle θ_0 depicted in **Figure 2-1** could be well described by the famous Young’s equation:[3]

$$\cos \theta_0 = \frac{\gamma_{SG} - \gamma_{SL}}{\gamma_{LG}} \quad (2-2)$$

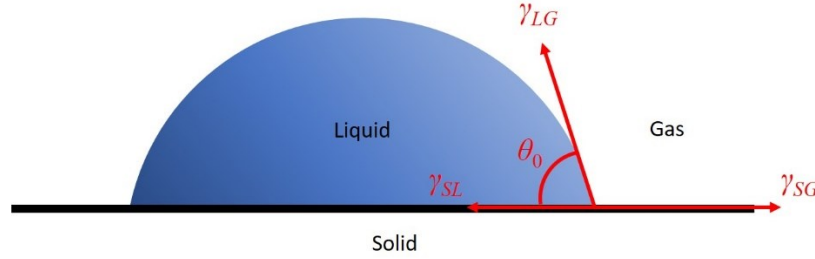


Figure 2-1: Schematic of a typical gas-liquid-solid three phase system and the interfacial tensions between the respective two phases.

Although **Equation (2-2)** originates from a rigorous thermodynamic derivation by minimizing the excess free energy of the overall system, the final mathematical expression gives a straightforward description of the mechanical balance at the TPCL in the horizontal direction. It is noted that θ_0 described in **Equation (2-2)** should be considered as a geometrical parameter observed on the macroscopic scale where the long-range intermolecular force is negligible.[30] When the radius of the solid-liquid contact area is extremely small (typically less than 100 nm), an extra term regarding the line tension which indicates the additional free energy to create the unit length of the TPCL should be added into **Equation (2-2)**.[31]

In actual application, **Equation (2-2)** could suffer a remarkable limitation since the real solid surface does not comply with the critical assumption of being atomically smooth, homogeneous and non-deformed.[32] Therefore, the experimentally observed static contact angle θ_s is likely to deviate from θ_0 . The upper and lower limits of θ_s are called advancing and receding static contact angles, respectively. The difference between the advancing and receding contact angles is termed static contact angle hysteresis which is another critical parameter to characterize wetting phenomenon.[33] In practice, the experimentally measured θ_s could be considered to approximately equal to θ_0 if the static contact angle hysteresis is not considerable.

The static condition of a wetting system is believed to have a close correlation to the interaction between the corresponding liquid and solid which commonly refers to adhesion. To characterize such interaction, a concept of reversible work of adhesion (W_a) which reflects how much energy is needed to separate fluid from a unit area of solid surface in wetting systems is introduced by

Dupre.[4] Integrating with the description of θ_0 in **Equation (2-2)**, a simple expression of W_a is given:

$$W_a = \gamma_{LG}(1 + \cos \theta_0) \quad (2-3)$$

Equation (2-3), which is called the Young-Dupre equation, provides a convenient way to evaluate W_a .

2.2 Dynamic wetting and singularity problem

Essentially, a dynamic wetting process at an isothermal condition is a typical hydrodynamic transport phenomenon. However, a significant difficulty emerges as a consequence of the conflict between the no-slip boundary condition assumed in the classic hydrodynamic theory and the motion of the TPCL. A rigorous classical hydrodynamic analysis has been performed by Huh and Scriven to model a steady creeping flow of a fluid at the corner near the moving TPCL.[6] Although a reasonable velocity field has been achieved from their analysis, the result suggests that the no-slip boundary condition could lead to the unbounded stress and pressure at the TPCL, which implies that the energy dissipation close to the TPCL diverges in the classical hydrodynamic description. This issue in dynamic wetting is often called the moving contact line singularity or paradox.

Because of the singularity, several attempts have been made to theoretically rationalize the TPCL motion at a microscopic scale where the continuum of hydrodynamics breaks down. Some mechanisms or hypotheses, namely the existence of a thin precursor film spreading ahead of the moving meniscus,[34] the violation of the no-slip boundary condition at the microscopic region near the TPCL[35] and the remarkable shear thinning viscosity of Newtonian fluid at the immediate TPCL,[36] have been artificially introduced to circumvent the singularity existing in the classic hydrodynamic analysis. However, these mechanisms have not been fully verified due to inadequate experimental proof.

From a practical perspective, two types of situations, including forced and spontaneous wetting, are frequently encountered in the dynamic wetting phenomena. The forced wetting refers to the case where the TPCL is in motion due to the external force applied (**Figure 2-2a**). In this case, a competition exists between the tendency of relaxing the system into equilibrium and the external

force driving the system away from the equilibrium state. For the spontaneous wetting, the TPCL could spontaneously evolve until the system reaches a new stable state, in the case that a liquid droplet is deposited on a surface or the surrounding environment of a deposited droplet is replaced (**Figure 2-2b**). Both forced and spontaneous wettings are the general forms of wetting dynamic phenomena. They could give complementary insights into the complicated physics of the TPCL motion.[37] From experimental investigations in scientific research, the forced wetting usually involves a constant velocity of the TPCL whereas the TPCL velocity is successively varied in the case of the spontaneous wetting.

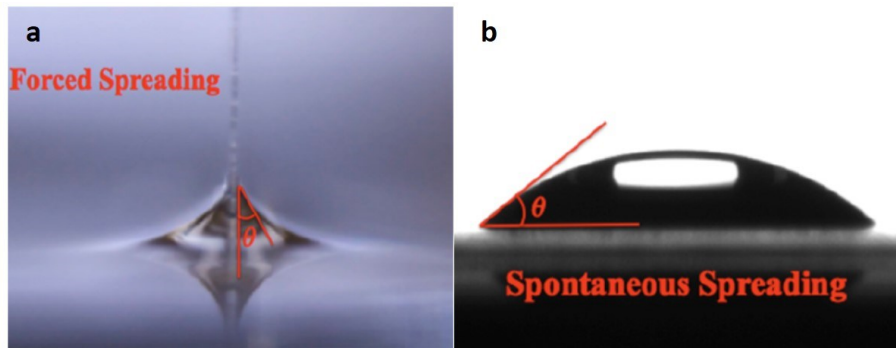


Figure 2-2: Schematics of (a) forced wetting and (b) spontaneous wetting[38]

2.3 Common approaches for wetting dynamic investigation

As the dynamic wetting occurs out of the thermodynamic equilibrium, it is an irreversible process involving certain energy dissipation mechanisms. Depending on different considerations of dominant energy dissipation mechanisms, two conventional approaches, including HD and MK, are frequently used in the dynamic wetting research.[39] The HD approach mainly takes into account the dissipative energy arising from the viscous flow in the bulk of fluids, whereas the MK highlights the friction dissipation between fluid and solid surface at the vicinity of the immediate TPCL. Essentially, these approaches are distinctive from each other since they rely on different frameworks. Nevertheless, both approaches focus on establishing a correlation between the observed dynamic contact angle and the velocity of the TPCL. In this section, some common approaches for the theoretical investigation of the wetting dynamics are thoroughly reviewed.

2.3.1 HD approach

The most frequently used HD approach for the wetting dynamics originated from Cox's hydrodynamic analysis.[12] In his analysis, the moving meniscus has been divided into three hypothetical regions with different length scales as sketched in **Figure 2-3**: the outer, intermediate and inner regions are supposed to be characterized by the length scales at the macroscopic, mesoscopic and microscopic levels, respectively. In the macroscopic outer region, the interface configuration is assumed to be accurately described by the analytical solution of a static condition. The static interface profile and the solid surface could form a contact angle which is called macroscopic contact angle, or apparent dynamic contact angle in the HD approach ($\theta_{d,H}$). As the interface is microscopically close to the TPCL, a microscopic cut-off length (L_S) with the order of a molecular size has been introduced to characterize the size of the inner region. In this region, totally different mechanisms other than hydrodynamics are supposed to determine the shape of the interface. Currently, the exact physics of this region has not been fully understood, as a direct experimental probing of the microscopic inner region has not been realized. However, solid-liquid interactions in the molecular level, such as van der Waals, electrostatic and hydrophobic forces, have been reasonably suggested to be crucial factors.[39] A concept of microscopic contact angle (θ_m) is applied to reflect the effect of these intermolecular forces on the meniscus shape at the microscopic scale. The existence of the intermediate region is proposed to connect the outer and inner regions. In the intermediate region, the prevalent hydrodynamic transport could result in a considerable energy dissipation from viscous flows.

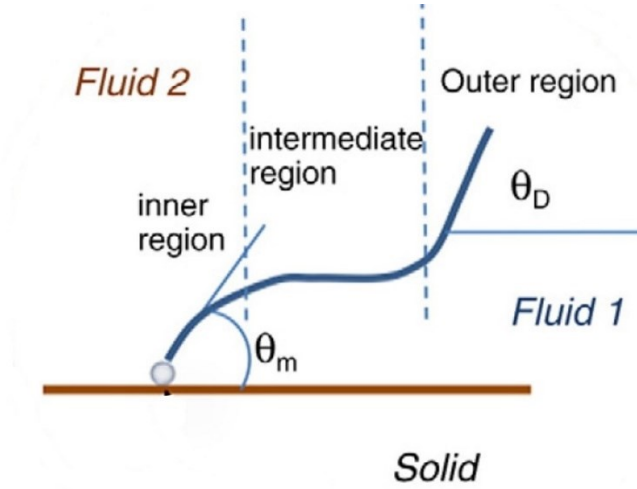


Figure 2-3: Schematic of three hypothetical regions of moving meniscus in Cox's hydrodynamic analysis.[32]

By matching the asymptotic expansions to the intermediate regime, the hydrodynamic flow equations have been solved by Cox. For his solution, in the simplest form, the relation between the assumed θ_m at the inner region and $\theta_{d,H}$ observed from the outer region is expressed as follows:

$$g\left(\theta_{d,H}, \frac{\mu_1}{\mu_2}\right) - g\left(\theta_m, \frac{\mu_1}{\mu_2}\right) = \pm Ca \ln\left(\frac{L}{L_S}\right) \quad (2-4)$$

In **Equation (2-4)**, Ca is the dimensionless capillary number which is defined as $Ca = \mu U / \gamma$, where μ could be the viscosity of advancing or receding fluid depending upon specific situations, U is the velocity of the TPCL and γ is the interfacial tension between the advancing and receding fluids. L is a macroscopic length of the wetting system. The plus and minus signs before the capillary number represent advancing and receding cases of the primary fluid concerned, respectively. When the plus sign is applied, the viscosity ratio μ_1/μ_2 is defined as the viscous ratio between the receding and advancing fluids, and μ in Ca equals to the viscosity of the advancing fluid; on the contrary, the negative sign indicates that μ_1/μ_2 is the ratio between the advancing and receding fluid viscosities and μ in Ca is the viscosity of the receding fluid.[32] Moreover, the integral function $g(\theta, \mu_1/\mu_2)$ in **Equation (2-4)** is defined as

$$g\left(\theta, \frac{\mu_1}{\mu_2}\right) = \int_0^{\pi-\theta} \frac{d\epsilon}{f\left(\epsilon, \frac{\mu_1}{\mu_2}\right)} \quad (2-5)$$

where the function $f(\beta, \mu_1/\mu_2)$ is written as

$$f\left(\epsilon, \frac{\mu_1}{\mu_2}\right) = \frac{2 \sin \epsilon \left[\left(\frac{\mu_1}{\mu_2}\right)^2 (\epsilon^2 - \sin^2 \epsilon) + 2 \frac{\mu_1}{\mu_2} \{\epsilon(\pi - \epsilon) + \sin^2 \epsilon\} + \{(\pi - \epsilon)^2 - \sin^2 \epsilon\} \right]}{\left(\frac{\mu_1}{\mu_2}\right)^2 (\epsilon^2 - \sin^2 \epsilon) \{\epsilon(\pi - \epsilon) + \sin \epsilon \cos \epsilon\} + \{(\pi - \epsilon)^2 - \sin^2 \epsilon\} (\epsilon - \sin \epsilon \cos \epsilon)} \quad (2-6)$$

Equation (2-4)~(2-6) are called the HD model. Due to the experimental difficulty of determining θ_m and L_S , θ_m and $\ln(L/L_S)$ in this model could be regarded as adjustable parameters. In the common case of a liquid spreading on a gaseous surrounding, the dominant viscosity of the advancing phase ($\mu_1/\mu_2 \sim 0$) could lead to the simplification of the integral function $g(\theta, \mu_1/\mu_2)$ in the model,

$$g(\theta, 0) = \int_0^\theta \frac{\epsilon - \sin \epsilon \cos \epsilon}{2 \sin \epsilon} d\epsilon \quad (2-7)$$

As suggested by Voinov[40], a further simplification of **Equation (2-7)** could be carried out in the case that θ falls into the range between 30° and 135° , which commonly happens in the partial wetting. In such a case, the approximation of $g(\theta, 0)$ could be given by $g(\theta) \approx \theta^3/9$. As such, **Equation (2-7)** could have a simple form as

$$\theta_{a,H}^3 - \theta_m^3 = \pm 9Ca \ln\left(\frac{L}{L_S}\right) \quad (2-8)$$

As the complicated integral function in the original model is eliminated in **Equation (2-8)**, the latter is a frequently used form of the HD model in applications.

Other than the Cox's conventional HD approach, another sophisticated approach, known as the microhydrodynamic approach, has been proposed by Shikmurzaev.[41] In his approach, the interfacial tension near the TPCL at the dynamic state is considered to deviate from the equilibrium value due to the fact that the formation-disappearance of the interface occurs there. As a consequence, an interfacial tension gradient could exist. On the assumption that Young's equation is still valid on the dynamic condition, a mathematical relation between the dynamic contact angle and the velocity of the TPCL has been established by performing hydrodynamic analysis. The major advantage of the microhydrodynamic approach is that it takes into account the influence of some non-local factors beyond the velocity of the TPCL (e.g. the flow field near the TPCL) on the wetting dynamics.[42] Unfortunately, in this approach, too many unmeasurable parameters which could only be extracted from an experimental data fitting process restrict its widespread application.[43]

2.3.2 MK approach

The original MK approach was developed by Blake and Haynes in 1969.[11] According to the description of their approach, the macroscopic behavior of the TPCL motion is a consequence of overall statistical motions of microscopic elements (namely, individual molecule, a segment of macromolecules or molecular cluster) at the immediate vicinity of the TPCL as illustrated in **Figure 2-4**. Moreover, the microscopic elementary motion is assumed to be thermally activated. At equilibrium, the ceased TPCL motion implies that the statistical frequencies of the elementary displacement in forward and backward directions which are defined as the direction along and against the TPCL motion respectively are identical. By analogy with the activated rate theory of Eyring,[44] the frequency (K_0) to either direction at equilibrium is expressed as,

$$K_0 = \frac{k_B T}{h} \exp\left(\frac{-\Delta G_0}{N_A k_B T}\right) \quad (2-9)$$

where k_B and h are the Boltzmann and Planck constant respectively, N_A is Avogadro's number, T is absolute temperature, and ΔG_0 indicates the energy barrier of thermal activation for one-mole elementary units at equilibrium.

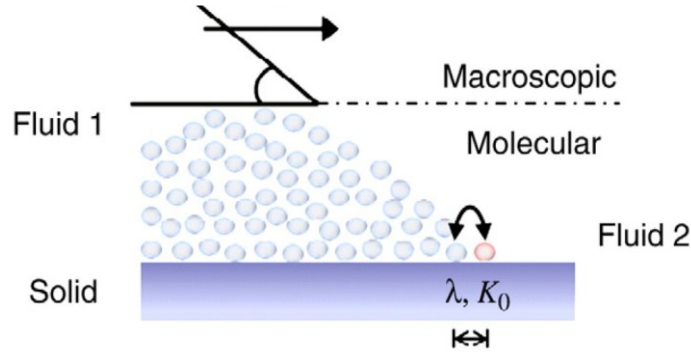


Figure 2-4: Schematic of the microscopic elementary motion described in the MK approach.[32]

At the dynamic situation where the contact angle deviates from the static one (θ_s), the energy barrier of thermal activation could be altered due to a driving force (F_d) acting on the TPCL which is given by,

$$F_d = \gamma(\cos \theta_{d,M} - \cos \theta_s) \quad (2-10)$$

where $\theta_{d,M}$ is the non-static dynamic contact angle or apparent dynamic contact angle in the MK approach. By assuming the mean distance between two nearest thermal activated sites is λ , the

number of such sites at the unit area is roughly equal to $1/\lambda^2$. Thus, the energy barrier of the forward motion is decreased and the reverse one is increased with the same amount of $F_d\lambda^2/2$. The thermally activated frequency of the forward direction (K_+) and backward direction (K_-) are given by,

$$K_+ = \frac{k_B T}{h} \exp\left(\frac{-\Delta G_0/N_A + F_d\lambda^2/2}{k_B T}\right) \quad (2-11)$$

$$K_- = \frac{k_B T}{h} \exp\left(\frac{-\Delta G_0/N_A - F_d\lambda^2/2}{k_B T}\right) \quad (2-12)$$

The net frequency (K) at the dynamic state is described in terms of the frequency difference between the forward and backward motion,

$$K = K_+ - K_- = 2K_0 \sinh\left[\frac{\gamma(\cos\theta_{d,M} - \cos\theta_S)\lambda^2}{2k_B T}\right] \quad (2-13)$$

where K_0 is the frequency of the microscopic motion in any direction at equilibrium. Subsequently, the macroscopic velocity of the overall TPCL motion is reasonably evaluated by the product of K and λ ,

$$U = 2K_0\lambda \sinh\left[\frac{\gamma(\cos\theta_{d,M} - \cos\theta_S)\lambda^2}{2k_B T}\right] \quad (2-14)$$

Equation (2-14) is the full mathematical description of the MK model. It is seen that this model contains two microscopic parameters, K_0 and λ . When the argument of the hyperbolic sine function in **Equation (2-14)** is sufficiently smaller than unity, the model could be reduced to a linear form, which is called linear MK model,

$$U = \frac{\gamma(\cos\theta_{d,M} - \cos\theta_S)K_0\lambda^3}{k_B T} = \frac{\gamma}{\xi}(\cos\theta_{d,M} - \cos\theta_S) \quad (2-15)$$

where ξ is defined as the coefficient of contact line friction which is given by $\xi = \frac{k_B T}{K_0\lambda^3}$. In this linear form, two microscopic parameters in **Equation (2-14)** are integrated into one parameter. It is noted that ξ has the same unit as the dynamic viscosity. Thus, the energy dissipation at the TPCL zone could be indicated by this combined parameter quantitatively.

One of the remarkable advantages of the original MK approach over the HD approach is that the fluid-solid interaction is considered. However, it has the limitation that the effect of fluid viscosity on the dynamics of the TPCL moving is not considered. To fill this gap, this approach was further modified by Blake et al.[45] In the amendment, an improvement was achieved by adding an extra contribution to the energy barrier of molecular activation arising from liquid viscosity instead of only considering the influence from the interaction between solid and liquid as assumed in the original model. As a result, the total energy barrier of the thermal activation could be written as the sum of the contributions from liquid-solid interaction and fluid viscosity,

$$\Delta G_0 = \Delta G_S + \Delta G_{\mu 1} + \Delta G_{\mu 2} \quad (2-16)$$

where ΔG_S indicates the contribution of the interaction between a solid surface and both fluids, and $\Delta G_{\mu i}$ represents the contribution from the viscous interaction with surrounding fluid molecules in the fluid i . Base on Eyring's theory of fluid viscosity[46], the dynamic viscosity (μ) is directly related to ΔG_{μ} as following,

$$\mu = \frac{h}{V_L} \exp\left(\frac{-\Delta G_{\mu}}{N_A k_B T}\right) \quad (2-17)$$

where V_L is the volume of the unit flow and typically close to λ^3 . In the case that the considerable viscous contribution only comes from the fluid with dominant viscosity μ , combining **Equation (2-13)** **(2-16)** and **(2-17)** yields,

$$K_0 = \frac{k_B T}{\mu V_L} \exp\left(\frac{-\Delta G_S}{N_A k_B T}\right) \quad (2-18)$$

In practical terms, the evaluation of ΔG_S seems to be difficult. Thus, Blake and De Coninck[45] suggested a reasonable approximation that the contribution of the solid-liquid interaction on the unit area ($\Delta G_S/\lambda^2 N_A$) is equivalent to the reversible work of adhesion which could be evaluated by the Young-Dupre equation (**Equation (2-3)**). Taking this into account, the contact line friction could be expressed as

$$\xi \approx \frac{\mu V_L}{\lambda^3} \exp\left(\frac{W_a \lambda^2}{k_B T}\right) \quad (2-19)$$

Provided that λ and V_L/λ^3 do not vary too much case by case in a specific system, **Equation (2-19)** provides a theoretical prediction that the contact line friction increases linearly with fluid viscosity

and exponentially with adhesion energy. Although such dependence is indeed a coarse approximation, the validity of such theoretical correlation has been substantiated in studies of a number of surfactant-free systems, such as the spontaneous spreading of the glycerol-water mixture on glass[47], the electrowetting and retraction of the ionic liquids at the hydrophobic surface[48], and the forced wetting of the nylon filament.[49] Recently, Ramiasa et al.[50] and Goossens et al.[51] have performed in-depth investigations to disclose the intrinsic correlation of the dynamic behavior of liquid-air and liquid-liquid systems, as well as suggested a practical approach for the prediction of ζ in a liquid-liquid system from the corresponding ζ in liquid-air systems.

2.3.3 Combination of HD and MK approaches

The application of the HD or MK approaches concentrating on single energy dissipation mechanism could miss some critical physics governing the TPCL motion. Thus, intuitively, these approaches could somehow be integrated to achieve a more sophisticated approach that could simultaneously take into account both crucial energy mechanisms described in the HD and MK approaches. In the following, two different approaches are introduced to realize such a combination. Using these approaches, the real physics of the TPCL motion is expected to be further illustrated.

Normally, both $\theta_{d,H}$ in the HD model and $\theta_{d,M}$ in the MK model are achieved from the experimentally observed dynamic contact angle and treated to be identical in practice. Therefore, both are written as the dynamic contact angle (θ_d) in most of the expressions. However, in Petro's argument, it is assumed that $\theta_{d,M}$ is actually the microscopic contact angle (θ_m) in the HD model.[52] As such, a combined model of dynamic contact angle-TPCL velocity dependence could be formulated by substituting $\theta_{d,M}$ in **Equation (2-14)** into θ_m in **Equation (2-8)**,

$$\theta_d^3 = \arccos^3 \left[\cos \theta_s - \frac{2k_B T}{\gamma \lambda^2} \ln \left[\frac{U}{2\lambda K_0} + \sqrt{\left(\frac{U}{2\lambda K_0} \right)^2 + 1} \right] \right] + 9 \frac{\mu U}{\gamma} \ln \left(\frac{L}{L_S} \right) \quad (2-20)$$

Taking into account that the work done by the unbalanced interfacial tension on the moving TPCL is totally compensated by the energy dissipation channels from viscous flow in the wedge near the TPCL as well as the friction at the TPCL, de Ruijter et al. suggested an alternative combined approach and derived a formulation specifically for a spreading droplet,[53]

$$U = \frac{\gamma(\cos \theta_s - \cos \theta_d)}{\xi + 6\mu\Phi(\theta_d)\ln\left(\frac{L}{L_s}\right)} \quad (2-21)$$

where $\Phi(\theta_d)$ is a factor related to the geometry of the droplet. In the case that the shape of a spreading droplet could be approximated as a spherical cap, $\Phi(\theta_d)$ could be expressed as,

$$\Phi(\theta_d) = \frac{\sin^3 \theta_d}{2 - 3 \cos \theta_d + \cos^3 \theta_d} \quad (2-22)$$

2.3.4 Experimental validation

It is noted that all the approaches discussed above eventually interpret the dynamic behavior in the form of the relation between U and the dynamic meniscus shape characterized by θ_d . Thus, the common demonstration of any given model is the comparison with the easily collected experimental data of θ_d and U over a certain range. Moreover, some ancillary measurements are also required to determine other necessary measurable parameters, such as fluid viscosity and interfacial tension. In this section, several relevant experimental data found in the literature are selected to illustrate some success of these models in the interpretation of the experimental observation.

In the paper of the HD model derivation,[12] Cox validated his model by a comparison of Hoffman's experimental data regarding the moving meniscus shape of silicone oil in the glass capillary[9]. Blake and Haynes adopted the experimentally observed shape of the water-benzene interface in the capillary tube to validate the MK model in the original publication where they proposed this model.[11] In the initial work of developing the combined approaches, Petro et al.[52] and de Ruijter et al.[53] confirmed the validity of their respective combined models by the experimental dynamic wetting data of glycerol-water mixture and di-n-butylphthalate (DBP) on the low energy polyethylene terephthalate (PET), respectively.

In addition to the preliminary validation of these models outlined in the corresponding original works, extensive experimental studies of wetting dynamics have been conducted to further explore the applicability of these models. Haynes and Ralston[54] examined the dynamic wetting and dewetting of water as well as glycerol on the smooth PET surface and subsequently pointed out that the MK model is more suitable for their data description than the HD model. The experimental study of the advancing and receding behavior of the hexadecane and octamethylcyclotetrasiloxane

(OMCTS) on the fluorinated surface was reported by Schneemilch and coworkers.[55] Their work has concluded that the better description of the HD and MK models on the dynamic behavior depends on the direction of the movement in the case of hexadecane, but such dependence is trivial for OMCTS; and furthermore, the best prediction of their experimental data was given by the Petro's combined model. The experimental dynamic spreading data of polymers along with their mixtures was found to have a satisfactory agreement with de Ruijter's combined model in the case of complete wetting whereas molecular-kinetic model worked well for the partial wetting case.[56] Fetzer et al. were able to demonstrate experimentally that the HD and MK model could satisfactorily describe the dodecane-water displacement behavior at the initial fast-speed stage and final stage with low speed, respectively.[57]

Due to a large number of reports on the interpretation of the dynamic wetting behavior with these models, only a few typical examples are covered in this section. Nevertheless, all the cases stated above collectively indicate that the applicability of each model to the dynamic wetting description could vary case by case.

2.3.5 Limitations of these approaches

Even though these generally accepted approaches have successfully been used to interpret numerous experimental observations of wetting dynamics, it should be recognized that some critical limitations may appear during their applications.

First, in terms of model expression, all approaches involve several crucial parameters related to microscopic properties that cannot be currently measured directly from the experiments. Therefore, practical experimental data fitting process is commonly performed for their evaluations. Yet, physically unreasonable information may arise from such a purely mathematical process sometimes.[43] Moreover, applying the combined approaches is more likely to increase the possibility of overparameterization as it is suggested to be phenomenological.[39] Due to the free choice of these parameters, the demonstrated agreement of the experimental data to the theoretical models does not mean that these approaches could essentially provide a reliable description of a real dynamic behavior all the time. Comprehensive and detailed analysis of these extracted free parameters could potentially alleviate that unreliability, but such analysis could be complicated.

Second, as the typical way for dynamic behavior quantifications in these approaches focus on establishing the dependence of U on θ_d , the proper and accurate acquisition of θ_d from experiments

looks clearly important. Nevertheless, the conventional techniques of the image-based measurement on θ_d suffer from an accuracy limit since it is usually inadequate to probe the length scale in submicron level. Currently, adopting alternative experimental techniques of delicate microscopic probing are still difficult to precisely determine the moving meniscus microscopically close to the TPCL. As a result, the experimentally measured dynamic contact angle is unlikely to be well-defined, and even worse, it may be short of physical implications for the wetting phenomenon description and investigation.[58] [59] For instance, from the perspective of the HD approach, it is generally believed that the actual dynamic contact angle at the immediate TPCL is rather different from the one assessed by the conventional techniques at a specific distance limited by the experimental capacity.

Furthermore, since the HD and MK approaches merely involve one independent energy dissipation mechanism of the TPCL motion for each, both approaches could reasonably capture the wetting behavior at a certain spectrum where the respective mechanism dominates. In fact, the appropriate criterion on the spectrum to distinguish the applicability of different approaches is rather difficult to be clarified. It is possible that the combined approaches could potentially overcome that difficulty by the simultaneous consideration of two dissipation mechanisms. Unfortunately, they have not been demonstrated as the universal solution yet.[52]

2.4 Surfactant

2.4.1 Basic concepts of surfactant

Surfactants which are also known as surface-active agents are natural or synthetic chemicals. The typical structure of surfactant molecules is comprised of an ionic or highly polar hydrophilic group and a nonpolar hydrocarbon chain which are called “head” and “tail” of surfactant molecules, respectively.[60] Moreover, the head and tail are covalently bonded, so neither could be easily separated from each other. Such a special structure is responsible for the interesting amphiphilic property of surfactants. For a surfactant dissolved in a solvent, one portion of the surfactant molecule, which is incompatible with the solvent, could cause the increase of the overall free energy. To lower the free energy of the whole system, surfactant molecules preferably adsorb or concentrate on the interface with a certain orientation. As a result, the corresponding interfacial properties are modified in the case of surfactant adsorption. The addition of surfactant into a

wetting system could more or less affect the wetting behavior. Due to this feature of surfactants, they have been widely used in a lot of fields to tune or control various wetting processes.

Despite the similar amphiphilic structure, surfactant molecules display a huge variety on detailed molecular structure. To distinguish them conveniently, several methods of surfactant grouping have been suggested. The most common method is based on the ionic properties of the hydrophilic head groups.[60] As shown in **Figure 2-5**, surfactants could be divided into four categories, including anionic surfactants with a negatively charged head group, cationic surfactants with the hydrophilic group carrying a positive charge, no charged nonionic surfactants and amphoteric surfactants (zwitterionic surfactants) which carry both positive and negative charges on a single surfactant molecule. Typically, zwitterionic surfactants could transfer into anionic or cationic ones when the surrounding environment, such as pH, is changed.[61] The recent appearance of highly activated Gemini surfactants (dimeric surfactants), a single molecule of which consists of two hydrophilic head groups and two hydrophobic groups,[62] [63] could potentially add one more category of surfactant types based on this classification method.

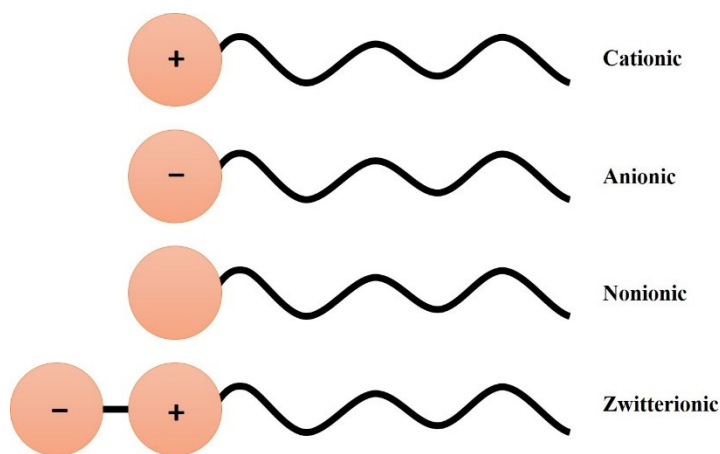


Figure 2-5: Schematics of the major four categories of surfactants based on the ionic group of hydrophilic head.

Another normal classification method of surfactants relies on their solubilities in solvents, such as oil or water. The concept of the hydrophilic-lipophilic balance (HLB), which is introduced to measure affinities of surfactants to water or oil, is considered as a criterion of this method.[64] The scale of HLB is typically distributed from 0 to 20.[65] A simple method has been suggested to estimate the HLB value of a certain surfactant by accumulating the effect of each chemical group in the surfactant molecule on the overall property.[64] [66] Higher HLB indicates that the

surfactant has more tendency of being dissolved into water. By taking the HLB value of 10 as a reference, the surfactant could be roughly classified as water-soluble and oil-soluble. A more comprehensive classification of surfactants based on HLB could be found somewhere, which could provide an intensive instruction of surfactant applications.[67] [68]

For a certain surfactant solution of low concentration, in addition to most adsorbed surfactant molecules at the interface, a tiny amount of the molecules remaining in the bulk could be homogeneously dispersed in the solvent as an isolated form. As the concentration is increased, the finite interface area could gradually saturate with surfactant molecules and hence significantly restrict further surfactant adsorption. At a critical point, a certain number of molecules could spontaneously aggregate in bulk instead of going to the interface, and in most cases form an aggregate structure of a spherical geometry that is known as surfactant micelles. The typical configuration of surfactant micelle in aqueous media is given in **Figure 2-6a**: the hydrophilic head groups are located on the surface while hydrophobic chains congregate in the core. On the other hand, the positions of the hydrophilic and hydrophobic portions could be reversed in the solvent of non-polar oil as shown in **Figure 2-6b**. The formation of micelles could effectively avoid the incompatible portion of surfactants from contacting with the solvent and therefore lower the overall free energy. The concentration in which the aggregation begins to take place refers to the critical micelle concentration (CMC). Above the CMC, both individual surfactant molecules and surfactant micelles are believed to exist in the solution simultaneously. The size of a micelle could depend on many factors, such as the chemical structure of surfactant and solvent, surfactant concentration, temperature to name just a few, but the typical diameter of micelles is around several nanometers.[69] According to the theory of Israelachvili et al.[70], some larger sized structures of surfactant aggregates beyond the spherical micelle, such as cylindrical micelles and bilayer structures are likely to form at even higher surfactant concentration.

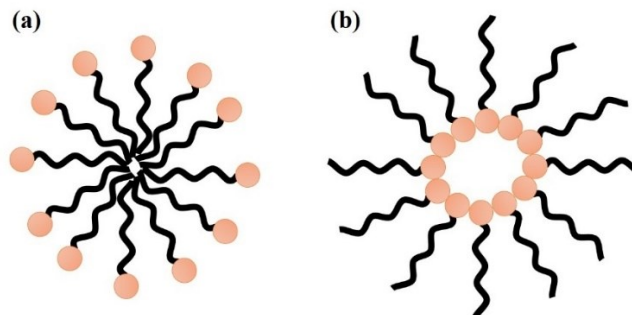


Figure 2-6: Schematics of structures of surfactant micelles in (a) aqueous and (b) oil media.

2.4.2 Surfactant adsorption at the interface

As stated previously, in the presence of surfactant, interfacial properties (e.g., interfacial tension of fluid-fluid interface or surface energy of fluid-solid interface) are most likely affected by the preferential surfactant adsorption at the interface. From the molecular point of view, interfacial energy originates from the asymmetric molecular attractions acting on the molecules at the interface. Thus, the alternation of the interfacial energy occurs when the surfactant molecule substitutes the original one at the interface during the adsorption process. The extent of the alteration relies on the nature and amount of the adsorbed molecules on the interface. The surface excess concentration (Γ) defined as the number of surfactant molecules at the unit interfacial area is proven to be a useful characterization of surfactant adsorption. Based on the thermodynamic theory, Gibbs has derived an expression to quantitatively correlate the change of the interfacial energy (γ) caused by surfactant adsorption to the surfactant concentration in the bulk (c_b) and Γ , which is given as [67]

$$\Gamma = -\frac{1}{RT} \frac{d\gamma}{d\ln c_b} \quad (2-23)$$

In practice, **Equation (2-23)** is rarely adopted to interpret experimental data directly. However, on the one hand, the change of γ could give a hint to Γ in the system where γ could be easily measured with this equation; on the other hand, the access to the change of interfacial energy is allowed by **Equation (2-23)** when Γ could be measured directly.[67] It should be noted that **Equation (2-23)** is no longer valid at the concentration above the CMC where γ is nearly constant.[71]

At the fluid-fluid interface, adsorbed surfactant molecules preferentially orientate with the head exposed to the more polar phase and the tail located in the less polar one. Normally, such molecular

orientation at the interface could result in the reduction of the interfacial tension. The interfacial tension keeps decreasing with the increase of surfactant concentration in the bulk until the CMC in which all the adsorption sites on the interface are fully occupied by the adsorbed surfactant molecules.

It is believed that the surfactant adsorption at the fluid-solid interface is driven by the interactions between surfactant molecules and the solid surface.[72] Thus, the adsorption on such interface is unlikely to take place if the interaction is rather weak. Apart from the adsorption caused by chemical reactions, the interaction could arise from several kinds of intermolecular forces, such as electrostatic interactions, hydrophobic bonding, hydrogen bonding and dispersion forces.

In addition to the thermodynamic consideration thus far, it is noted that the surfactant adsorption at the interface is a kinetic process, and hence the corresponding interfacial tension is supposed to be time-dependent under isothermal conditions. The typical surfactant adsorption kinetics could be described as a two-step process: the diffusive transport of surfactant molecules from the bulk solution as well as the local adsorption that occurs at the interface.[73] To gain further knowledge of the surfactant adsorption kinetics, in 1946, Ward and Tordai[74] derived a simple diffusion-controlled adsorption kinetics model. Even though dozens of models have been developed to deal with surfactant adsorption kinetics afterward, it appears that their influential model is still considered as the basis of most contemporary models of surfactant adsorption kinetics because most adsorption processes are diffusion-controlled.[73] Based on their model, a quantitative description with regard to the time dependence of Γ for an initially surfactant-free interface is given by,

$$\Gamma(t) = 2c_b \sqrt{\frac{D_s t}{\pi}} - \sqrt{\frac{D_s}{\pi}} \int_0^t \frac{c_1(\tau)}{\sqrt{t-\tau}} d\tau \quad (2-24)$$

where c_b and c_l are the surfactant concentration in the bulk and the subsurface immediately outside the interface respectively; t is time and D_s is the surfactant diffusivity in the solution. Currently, obtaining an analytical solution of **Equation (2-24)** seems impossible. Nevertheless, with the integrated consideration of this equation along with **Equation (2-23)**, which suggests the direct dependence of the interfacial tension change on Γ , it could be implied that the relatively fast relaxation of the dynamic interfacial tension caused by surfactant adsorption is expected at increased surfactant concentration. The second terms in **Equation (2-24)** is the negative

contribution from the desorption process to the overall net adsorption amount.[75] Considering the early stage where the desorption is negligible, this term can be safely neglected, resulting in

$$\Gamma(t) = 2c_b \sqrt{\frac{D_s t}{\pi}} \quad (2-25)$$

Equation (2-25) predicts that Γ could linearly increase with $t^{0.5}$ at the initial stage, which has been substantiated by some experiments of surfactant adsorption. [73] [76]

2.5 Wettability alteration in the presence of surfactant

The surfactant-induced interfacial energy change of one or more interfaces in a three-phase wetting system is responsible for the modified wetting behavior. The term wettability alteration of a certain solid surface is frequently adopted to describe the changed static wetting state caused by surfactant. In general, the variation of the static contact angle could give an appropriate interpretation of the wettability alteration and hence the sessile drop contact angle measurement is preferably used to offer a quantitative characterization. Driven by the interest to obtain industrial products with optimized formulation for wettability modification, many experiment-based studies have been carried out to interpret the wettability variation of a variety of solid surfaces under the influence of surfactants. For these studies, it appears that the water/air/solid and water/oil/solid wetting systems have attracted more attention due to widespread applications related to them.

2.5.1 Water/air/solid system

For the water/air/solid wetting system, the majority of works have focused on the phenomenon of spreading surfactant aqueous solutions on different types of solid substrates, which is an essential process for coatings, cosmetic applications and pesticide distributions. For these works, the enhanced or hindered spreading of an aqueous solution with surfactant addition is preferentially substantiated by observed smaller or larger static contact angles of the aqueous phase, respectively.

The surface of glass or quartz, a kind of purer glass in terms of the silicon dioxide content, is a common high energy surface. Normally, pure water could completely spread over glass or quartz surface in air. Early study regarding some traditional ionic and nonionic surfactant solutions spreading on the hydrophilic glass surface revealed that cationic surfactant solutions have distinct wetting behavior from other anionic and nonionic surfactant solutions: in the presence of cationic

surfactant, the spreading of aqueous solution is considerably hindered due to the decreased wettability of glass surface by the aqueous phase.[77] Later, it was found that the negative impact of cationic surfactant on spreading of aqueous solution over quartz surface could be alleviated at the increasing surfactant concentration because of bilayer structure formation of adsorbed surfactant on the surface.[78] The solutions of Zwitterionic surfactant with a big polar group which is likely to introduce steric effect have been verified to have a small impact on the wettability of quartz surface over a wide range of surfactant concentrations.[79] Such a feature of these Zwitterionic surfactant solutions is quite different from conventional nonionic or ionic surfactant solution.[79] Moreover, the synergetic effect of mixed surfactant systems on the wettability of glass surface by their aqueous solution has been reported to arise from the specific interactions of different surfactant molecules.[80]

Except for the high energy hydrophilic solid surface mentioned in the previous paragraph, low energy hydrophobic solid surfaces, such as paraffin, polytetrafluoroethylene (PTFE) and polymethylmethacrylate (PMMA) have been extensively studied as well. Since water does not preferably spread on such surfaces, surfactants are introduced into the water to enhance the ability of the aqueous phase on wetting the surface in most cases. It has been shown that surfactant mixtures generally display a better performance on the wettability improvement of the low-energy surface than a single surfactant.[81] [82] [83] Mixtures of surfactants and additives may also improve the wettability of the low-energy surface in some situations.[84] Furthermore, extraordinary trisiloxane surfactants which are referred to as superspreaders have been widely reported in that their aqueous solutions could completely wet low energy surface.[85] Nevertheless, the corresponding mechanism regarding the superspreading phenomenon is still in hot dispute. [20] [86]

2.5.2 Water/oil/solid system

The wettability alternation of water/oil/solid system in the presence of surfactant is strongly related to the application of enhanced oil recovery (EOR) in the oil and gas industry as well as the implementation of a suitable detergent for the removal of oily dirt from the surface by aqueous solution. In the oil and gas industry, the water flooding technique, which consists of injecting water or water-based solutions to help complement producing energy thereby expelling the residual oil out of rock pores, is frequently adopted to stimulate oil production. When this technique is applied,

more hydrophilic rock surface is favorable since more efficient spontaneous imbibition of water caused by capillary force could displace more trapped oil in the subsurface reservoir to the producing well.[87] [88] Therefore, the surfactant-induced wettability alternation could be a better candidate to reach this goal by lowering the oil-water interfacial tension and adjusting the surface energy of the rock surface. The latter mechanism is believed to be more prominent.[89] In fact, most relevant studies have concentrated on the capability of surfactants to lower the advancing static contact angle of the aqueous phase.

Even though most of the rock surface in the reservoir is intrinsically hydrophilic, in reality, the aging effect arising from the adsorption of components from the crude oil could lead to the hydrophobic rock surface.[89] The introduction of surfactant could cause the shift of the aged hydrophobic rock surface towards the hydrophilic state by two mechanisms: establishing a hydrophilic layer by the surfactant adsorption on the top of hydrophobic layer on the rock surface; or exposing the originally hydrophilic rock surface via the interaction between surfactants and adsorbed substance to remove that layer.[90]

The surfactant selection for the field application of EOR often depends on the rock type. For two common reservoir types, it has been found that more efficient wettability alternation could be achieved by cationic addition in the carbonate reservoir, whilst the anionic surfactant is more suitable for sandstone reservoir.[87] [91] However, some researchers suggested that nonionic surfactants could have higher ability of wettability alteration for EOR than ionic surfactants.[92] A recent study reveals that using the Gemini surfactant could achieve better performance of wettability alternation since its high density of charge could lead to a more efficient mechanism of oil layer removal.[93]

2.6 Influence of surfactant on wetting dynamics

The altered interfacial properties due to surfactant addition could adjust the capillary force acting on the TPCL and thereby modify the TPCL motion. From the theoretical perspective, the presence of surfactants could lead to a more complicated dynamic wetting behavior. Some surfactant-induced mechanisms are likely to dominate at certain stages of the dynamic process and considerably affect the corresponding dynamic behavior. In this section, some common mechanisms are reviewed.

The first mechanism concerns the fact that the surfactant adsorption at initially clean interfaces is a kinetic process, and hence the corresponding interfacial properties, which are commonly regarded as constants in the absence of surfactants, are time-dependent under isothermal conditions. As the instantaneous capillary force for the TPCL motion depends on the interfacial properties near the TPCL, a significant temporal relaxation of the interfacial energy caused by the surfactant adsorption kinetics could have an impact on the dynamic wetting behavior.

Second, apart from the temporal variation mentioned above, adsorbed surfactants at interfaces may not be spatially uniform in dynamic conditions. As a result, interfacial tension gradients are established, which could induce traction forces along the interface and hence drive fluid flow. This phenomenon is also known as the Marangoni flow and the induced additional tangential stress (σ_M) acting on the interface is given by:[20] [94]

$$\sigma_M = \nabla\gamma \quad (2-26)$$

where $\nabla\gamma$ denotes the interfacial tension gradient. A positive interfacial tension gradient indicates that the Marangoni flow is in the direction from low to high surface tension area. To be specific, if the interfacial tension of a sessile liquid droplet is greater at the area near the TPCL than the apex, the Marangoni flow could push the droplet outward and enhance the spreading rate of the droplet on the surface.

The additional mechanisms could arise from the existence of surfactant micelles in the solution above the CMC. For a surfactant micellar solution, if the migration of surfactant molecules to the interface during the adsorption could lead to a depletion of surfactant monomers in the bulk, surfactant micelles in the solution could break down into surfactant monomers to compensate. The typical relaxation time of the disintegrating process of the micelles has been reported to range from milliseconds to minutes.[95] [96] [97] As a result, the relevant kinetics of the surfactant adsorption associated with the dynamic wetting could potentially be affected.

In the investigation of wetting dynamics in the presence of surfactant, a quantification of the temporal evolution of instantaneous parameters relevant to wetting status was frequently adopted, instead of the dependence of the velocity of the TPCL on the dynamic contact angle described in the MK and HD models. Typically, the growth of the wetting area on the flat surface was described by a power law correlation for the case of droplet spreading: [86] [98] [99] [100] [101]

$$r_c \sim t^\alpha \quad (2-27)$$

where r_c is the radius of the liquid-solid contact area at the respective time (t) and α is called the wetting exponent which could be obtained through experimental data fitting. The spreading dynamics at different stages was found to be well described by **Equation (2-27)** and the underlying mechanisms governing the dynamics could be indicated by the extracted α . [98] [102] [103] The common relationship between α and the corresponding mechanism found in the literature is briefly summarized in **Table 2-1**. Normally, for the complete spreading of a surfactant-free droplet of low viscosity fluid, $\alpha \sim 0.5$ is extracted from the early stage, which corresponds to the regime dominated by inertia; [104] subsequently, a viscous regime of $\alpha \sim 0.1$ could be found at the late stage, which is consistent with the description of the well-known Tanner's law. [10] On the other hand, a dependence of α on surface wettability at the early regime was reported by Bird et al. [105] in the case of partial spreading. They found that α could decrease with increasing equilibrium contact angle. Recently, another viscous regime at the even earlier stage has been confirmed from the study of the spreading of high viscous fluid. [106] [107] The early viscous regime could be characterized by $\alpha \sim 1$ and the duration of this regime was related to the fluid viscosity. [107] Surfactant additions into spreading droplets were suggested to affect α as well due to additional mechanisms [103].

Table 2-1: Summary of the relationship between α and the corresponding mechanisms

Spreading exponent (α)	Corresponding mechanisms
0.1	Capillary-driven (opposed by viscous dissipation) [102] [108]
0.14	Capillary-driven (opposed by the contact line friction) [102] [108]
0.25	Marangoni force-driven [94] [101]
0.125	Gravity-driven [109]
0.5	Inertial force-driven [110] [104]
1	Dominated viscous force at the early stage [106] [107]

Chapter 3

Experimental methods

3.1 Materials

To investigate the influence of the high viscosity of the bitumen on the oil displacement process during the bitumen liberation, three high viscosity polybutene oils N190000, N450000 and N2700000 purchased from Cannon Instrument Co. were used in this study. All these liquids were Newtonian fluids and their relative density with respect to water was around 0.9. The general molecular structure of the oils is given in **Figure 3-1** and these oils are characterized by various viscosities due to different molecular weights. The glass micropipette from Drummond Scientific was used to fabricate the microscale curved solid surface to model the sand grain surface of the oil sands ore.

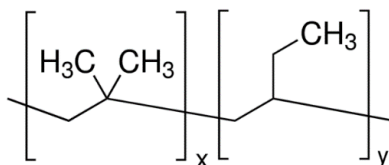


Figure 3-1: General molecular structures of high viscosity polybutene oil.

Three surfactant agents, namely anionic sodium dodecylbenzenesulfonate (SDBS, Sigma Aldrich), cationic hexadecyltrimethylammonium bromide (CTAB, Sigma Aldrich) and nonionic TritonTM X-100 (TX-100, Fisher Scientific), were used in this study. These water-soluble surfactants are expected to have negligible solubility in the oil phase as their hydrophile-lipophile balance (HLB) values are larger than 10.[64] All the agents were used as received without further purification. The corresponding molecular structures are given in **Figure 3-2**.

Fisher Scientific) for 1, 30 or 120 seconds and washed subsequently by pure toluene repeatedly. The silanization hydrophobized the glass surface due to the reaction of dichlorodimethylsilane with silanol groups on the glass surface.[112] Depending on the immersion time, the glass surface could be made to various degrees of surface hydrophobicities. To obtain a more hydrophilic glass surface, glass tips were treated by sodium hydroxide solution (pH = 12) for 2 hours, which hydrolyzed the glass surface and led to the formation of hydrophilic silanol groups on the surface, and subsequently rinsed by deionized water thoroughly. All the glass tips with various wettability modifications were dried in air for 24 hours prior to their use.

3.1.2 Preparation of surfactant aqueous solutions and the CMC determination

A series of surfactant aqueous solutions with the desired concentrations have been prepared with water produced by a Milli-Q filtration system. The surface tensions of these surfactant solutions at 20°C were measured by the du Nouy ring method (Tensiometer-K12, Kruss, Germany). With the plot of measured surface tension against logarithmic concentration as indicated by **Figure 3-4**, the CMCs of SDBS, CTAB and TX-100 were determined to be 2.1, 0.96 and 0.22 mmol/L, respectively. The surfactant aqueous solutions in glass jars at 5 concentration levels, which are given as multiples of the CMC (0.2, 0.5, 1, 3 and 10) were prepared by shaking and using ultrasound at 50 °C water bath.

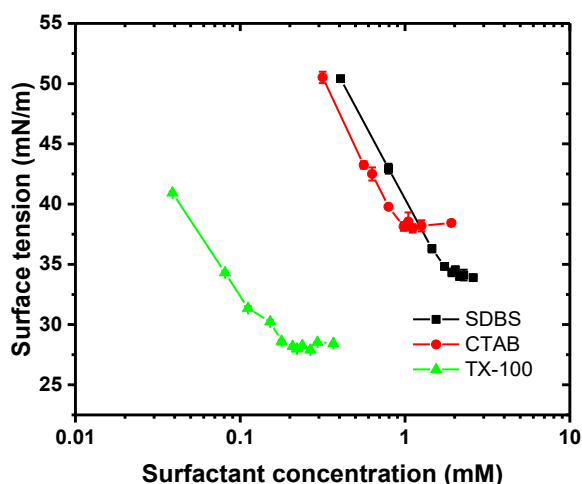


Figure 3-4: The plot of measured surface tension vs. logarithmic concentration of surfactants

3.2 Viscosity measurement of the oil sample

The AR-G2 rotational rheometer (TA instrument, USA) was used to determine the viscosity of the high viscosity oil samples. The principle of this measurement is based on the detection of the torque caused by the viscous flow of the sample in a cylinder gap at a certain rotational speed of geometry as illustrated by **Figure 3-5**. The measured torque and implemented rotational speed could be translated into the shear stress and shear rate with the known geometrical information. As a result, the viscosity of the sample could be readily calculated.

Since the high viscosity of the oil samples could more easily lead to the considerable torque during the measurement, the small parallel plate geometry with 20 mm diameter was selected. The shear rate was increased logarithmically from 0.01 s^{-1} to 1 s^{-1} for the data collection when the temperature was controlled at 20°C by circulating water pumped from the water bath and the electrically heated base simultaneously. It is noted that even higher shear rate should be avoided in this measurement as more significant dissipation arising from viscous flow could cause a considerable temperature increase of the sample. The results of the viscosity measurement are shown in **Figure 3-6**. Because of the independence of the oil viscosity on the shear rate, the rheological property of these oil samples is similar to that of bitumen, which shows Newtonian behavior. The viscosities of N190000, N450000 and N2700000 at 20°C were determined to be 810 ± 10 , 2140 ± 20 and $7890 \pm 100 \text{ Pa}\cdot\text{s}$, respectively, which are close to the typical viscosity of pure bitumen.

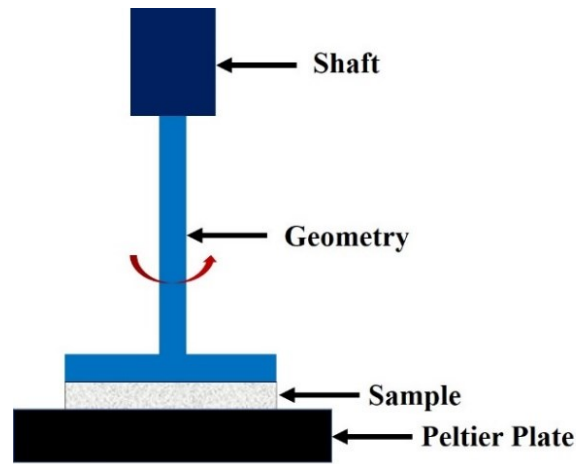


Figure 3-5: Schematic of viscosity measurement with a rotational rheometer.

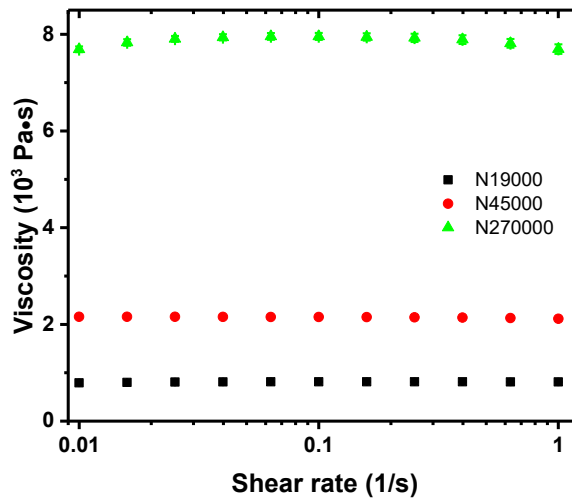


Figure 3-6: Measured viscosities of the high viscosity oil samples at the various shear rate

3.3 Measurement of interfacial tension

Due to the extremely high viscosity of the oil phase, the drop shape relaxation method, which is feasible to high viscosity liquid, was adopted to determine interfacial tensions between the oil and aqueous solutions in this study. The detailed description of this method will be given in **Chapter 5**. In short, the geometrical information on the spontaneous relaxation of an elongated liquid droplet into its final spherical shape in another immiscible liquid was obtained experimentally.

Subsequently, the interfacial tension between these liquids could be evaluated by fitting the experimental geometry of the droplet to the theoretical curve achieved by the hydrodynamic analysis. It should be mentioned that, in the presence of surfactants, the nonuniform surfactant distribution caused by the surfactant convection and diffusion on the interface was assumed to be negligible due to the small droplet size and the slow relaxation of the high viscosity fluid here.[113] Thus, the interfacial tension was nearly constant during the relaxation and the measured value from such method was believed to be close to the equilibrium value. Pure water as well as prepared SDBS and TX-100 aqueous solutions were directly used in this test, whereas CTAB solutions were adjusted by 10N HCl solution to acidic condition (pH=2) since the surface of the glass pipette was preferentially wet by oil in the natural CTAB solution.

3.4 Measurement of surfactant adsorption at the solid surface

The surfactant adsorption at the solid-water interface was quantitatively investigated using a quartz crystal microbalance with dissipation (QCM-D) technique. In principle, the piezoelectric quartz sensor of QCM-D could oscillate at a fundamental resonant frequency under an alternating current (AC) voltage applied between its electrodes. The frequency could be altered once adsorption or loading occurring on the surface of the sensor causes mass changes.[114] In a QCM-D experiment, two parameters, resonant frequency (f) and dissipation factor (D), could be simultaneously monitored. Therefore, the measured shift of f allows the evaluation of the adsorbed mass with some well-known empirical relationships. For a simple case, if the adsorbed substance is rigid and does not slip on the surface which normally indicated by a small trace of D , the shift of f at the overtone order of n (Δf_n) is proportional to the adsorbed mass (Δm) in the light of the Sauerbrey model:[115]

$$\Delta m = -C \frac{\Delta f_n}{n} \quad (3-1)$$

where C is the mass sensitivity constant, and n is the overtone number. It is noted that the adsorption kinetics could be understood through the temporal evolution of the monitored data.

In our study, a QSense Analyzer (Biolin Scientific, Sweden) was used to monitor f and D signals of the piezoelectric sensor. Silica sensors (QSX 303, QSense) were adopted to mimic the glass surface since silica is a major component of glass. The surfactant solutions of 0.5CMC and 3CMC,

which represent the concentration below and above CMC respectively, were selected for this analysis.

The experiments were carried out at a temperature of 20 °C. The fluid was feed by a peristaltic pump with a flow rate of 0.15 mL/min. At the beginning of the experiments, stable baselines of signals were established through the feed of deionized water flow. Subsequently, surfactant solutions were pumped into the system to observe the variation of f and D arising from the surfactant adsorption. The instrument could record 11 harmonics of f and D during the experiment, however, only the one at the third overtone was used for our analysis. After each measurement, the piezoelectric silica sensor, tubing and flow module mounted on the instrument were cleaned thoroughly by following the instructions provided by the manufacturer.

3.5 Spontaneous microscale oil displacement tests

The micropipette system, which has been used to investigate emulsion properties,[116] was modified here to study the displacement of an oil droplet on a stationary microscale curved solid surface in an aqueous phase at room temperatures (20°C). As shown in **Figure 3-7**, the micropipette experimental system is an inverted optical microscope (Zeiss Axiovert 200) equipped with micromanipulators, which could smoothly adjust the position of the micropipette mounted on them with a three-dimensional movement at microscale range. A charge-coupled device (CCD) camera is attached on the microscope to record observations in the form of digital images.

Two glass pipets were mounted on the two opposite micromanipulators as shown in **Figure 3-8**: one is the aforesaid pipet with spherical cap end fabricated as the substrate for the liquid-liquid displacement tests; and the other is the pipet with small amount of oil sample at the tip. The spherical cap surface was coated spontaneously by the oil when it was made to contact the oil sample on the opposite glass tip in air. Retracting the spherical cap pipet slightly several seconds later led to the formation of a submillimeter size oil droplet (approximately $5 \times 10^{-4} \text{ mm}^3$ if not specified) on the solid spherical cap surface. The freshly formed oil droplet spread slowly on the surface because of its high viscosity. To ensure the oil to be fully spread and relaxed on the solid sphere surface, a 30-minute waiting period was allowed prior to the drop receding experiment in solutions.

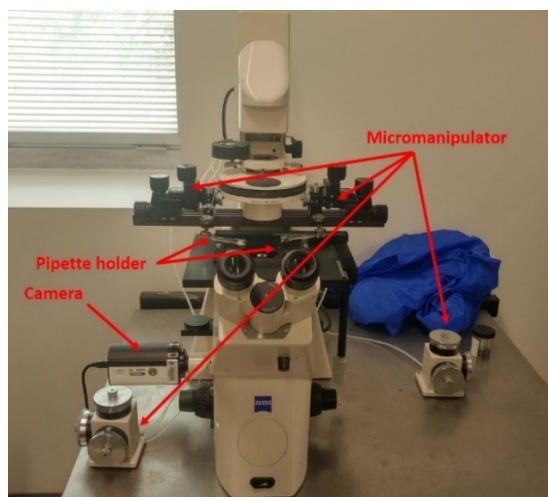


Figure 3-7: Photograph of micropipette system.



Figure 3-8: Photograph illustrating the sample delivery to the spherical cap surface of the glass tip.

Experiments were initiated by gently placing this partially oil-covered glass cap into a quiescent pool of aqueous solution while starting the time of the experiment. Driven by capillary force, the oil receded spontaneously on the solid surface in the aqueous phase to reach a new configuration as shown in **Figure 3-9**. Due to the strong flow resistance from the high viscosity oil used in our experiments, the oil relaxation may proceed much slower than other common spontaneous wetting processes. Because of the adequate solution in the pool, it was not necessary to take the overall depletion effect of surfactant concentration into account though a significant effect may take place locally. The maximum time of an individual experiment never exceeded 30 min within which the

mass loss of the solution in the reservoir due to the evaporation of the water from the pool was less than 2%.

The instantaneous configuration of oil on the solid surface was directly observed in situ through the optical microsystem with the objective lens of 10 times magnification. The whole process was observed under the optical microscope and captured by the CCD camera as sequential digital images. The captured digital images were stored in 8-bit grayscale 801×801 pixels array. The typical frame rate for the recording varied from 2 to 60 frames/min, enough to achieve a reasonable number of images in an individual displacement process. Each experiment was repeated at least three times until a satisfactory reproducibility was observed.

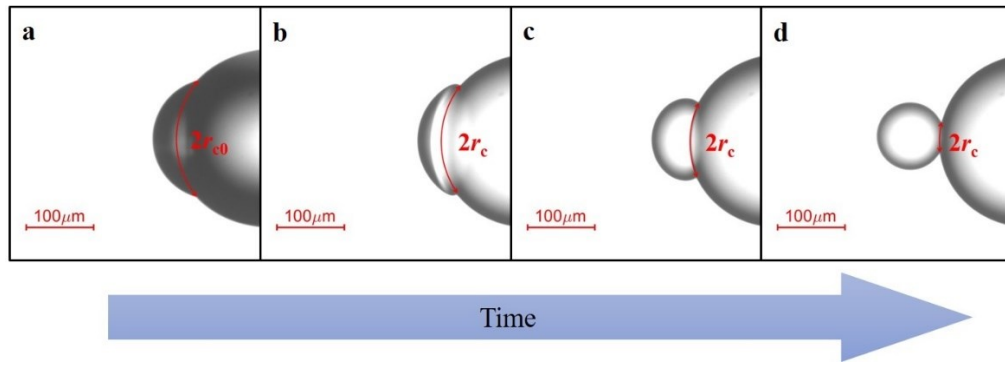


Figure 3-9: Snapshots of oil droplet receding on a solid surface in aqueous solution. The solid red lines indicate the arc length ($2r_c$) of the droplet wetted area on the curved surface between the TPC lines observed from the side view image at an experimental time (t). The subscript 0 for r_c in (a) denotes the initial time ($t = 0\text{s}$).

Chapter 4

Digital image analysis

4.1 Introduction

Using advanced digital computational image processing technology, several characterizations for the oil displacement process, such as the oil-solid contact area and the velocity of the TPCL, could be extracted from the captured side view images. Moreover, the dynamic contact angle, which is critical for the description of the oil displacement process, could be obtained from the image analysis of instantaneous droplet configurations as well.

In fact, the digital image analysis has been commonly used to directly measure the contact angle from a captured sessile droplet shape on a two-dimensional image because of its advantages of convenient operation and wide applicability on various situations.[117] The most straightforward method of measuring contact angle from an image is aligning a tangential line to the drop profile at the location of the TPCL. However, poor accuracy and relying on the experience of the operator could be the major limitation of this method.[118] In the past several decades, numerous computational methods (or algorithms) have been developed for more accurate image-based contact angle determinations. In the following paragraphs, several common algorithms for image-based contact angle measurements are briefly reviewed.

The half contact angle method is one of the simplest algorithms to readily determine the contact angle. [119] When the sessile drop on the flat surface is assumed to be a segment of a sphere under negligible gravitational effect, based on the pure geometric relation as indicated in **Figure 4-1**, half contact angle could be evaluated through the following simple mathematical formula with the measured contact surface radius (d_C) and apex height (h_A),

$$\frac{\theta}{2} = \tan^{-1} \left(\frac{h_A}{d_C} \right) \quad (4-1)$$

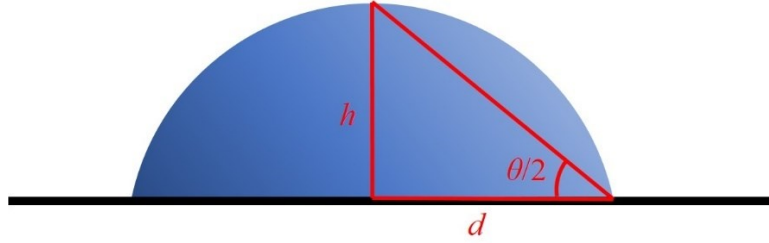


Figure 4-1: Schematic of contact angle determination by $\theta/2$ method

The state-of-the-art axisymmetric drop shape analysis (ADSA) is a versatile technique for the theoretical description of the drop shape. Despite various numerical implementations of ADSA, the overall strategy is consistent to determine an optimized theoretical shape of a quasi-static axisymmetric liquid drop by matching the drop profiles extracted from the image.[120] The theoretical shape profile in ADSA is commonly achieved through numerical integration of the Laplace equations with the inputs of physical properties which consist of interfacial tension, density, gravity and the surface curvature at the apex of the drop. Typically, surface tension is an adjustable parameter for the numerical scheme of the profile matching. The best fit allows a quick determination of contact angles as well as other properties, such as drop volume and surface area. This constitutes the classic ADSA method originally proposed by Rotenberg et al.[121]. Motivated by widening the application of the ADSA technique, more advanced methods derived from the original ADSA have been developed. For instance, the axisymmetric drop shape analysis-diameter (ADSA-D) method has been introduced to handle small contact angles [122]; the axisymmetric drop shape analysis-no apex (ADSA-NA) method has been used to determine the contact angle in the case of missing critical information at the apex region of the drop[123]; and the axisymmetric drop shape analysis-electric field (ADSA-EF) method has been performed to take into account the effect of electric field [124]. The main advantage of these methods based on the ADSA over the $\theta/2$ method is their high accuracy on contact angle measurement; however, considerable errors may appear when they are implemented to deal with asymmetric drop. The other limitation of these methods is that some physical properties are needed to be properly determined for the theoretical analysis.[125]

To overcome the drawbacks of the methods based on ADSA, some direct fitting algorithms, such as circle fitting[126], ellipse fitting[127] and polynomial fitting[118] [128] are frequently used to determine the contact angle of both axisymmetric and asymmetric drops without the need of

knowing any physical property of the system. For these algorithms, a whole extracted drop profile or part of it is directly fitted by a simple geometrical model. Afterward, the contact angle can be readily determined by calculating the slope of the best fitting curve at the TPCL. The accuracy of the contact angle measurement might be compromised by adopting these direct fitting algorithms. However, increasing the magnification or resolution are two practical ways to compensate for such a loss of accuracy.

It is noted that most algorithms mentioned above highly rely on extracted object profiles from sharp images. Recently, a new method which is called theoretical image fitting analysis (TIFA) has been developed to carry out an image-based contact angle determination without operating edge detection algorithm.[129] This new method could be exclusively applied to the case of blurred images commonly caused by the lack of contrast, out of focus or bad illumination.

In this study, the digital image processing for data acquisition could be performed in a more efficient way due to the high volume of images. Thus, the automatic digital image analysis is carried out here. In this chapter, the methodology of the digital image analysis for this study is discussed. With the help of modern computational technology, a custom-programmed Matlab® code was developed to realize the anticipated automatic image analysis. Error analysis was performed to understand some common influential factors on detected edge profiles associated with measured contact angles obtained from direct fitting algorithms.

4.2 Methodologies of digital image analysis

As shown in **Figure 3-9**, the digital snapshots captured by the camera in this study are grayscale images. The recorded image sequences were analyzed with a custom-programmed Matlab® code. Thanks to the high contrast of oil-water and glass-water interface, the contours of different phases could be extracted from grayscale images (**Figure 4-2a**). An embedded function was employed to automatically transfer edge locations to a set of consecutive edge pixel coordinates. The coordinates were then converted to physical units through the factor of $0.4644\mu\text{m}/\text{pixel}$ obtained by the length calibration. The TPCL (two single points on the 2-D image) was identified by searching for two maxima in the second derivative variation of the edge coordinate function (**Figure 4-2b**). By knowing the location of the TPCL, the oil and glass profiles were separated. A circle was fitted to the profile of the curved glass substrate to identify the oil-glass interface

(Figure 4-2c); and subsequently, the volume of the oil droplet (V_o) could be calculated due to the axisymmetric nature. The instantaneous oil-solid contact area was then evaluated from the arc length between the two contact points on the circle of the substrate. Meanwhile, the velocity of the TPCL was determined by analyzing the first derivative of the TPCL position with respect to the experimental time. Unfortunately, the limits of image resolution could cause some uncertainties of TPCL location, which may lead to more significant uncertainties in TPCL displacement velocity. To reduce such uncertainties, the experimental data were adjusted by a smoothing function using a moving average filter which was embedded in Matlab[®].

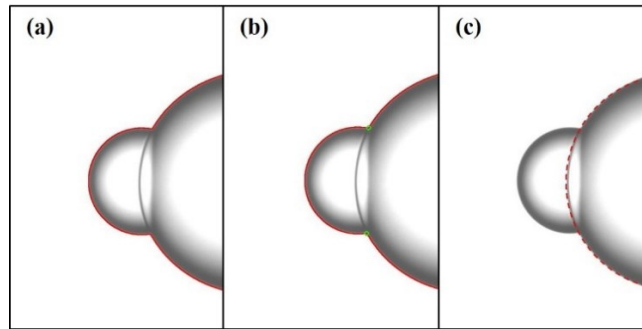


Figure 4-2: Visual demonstration of some critical steps during the digital image analysis.

In this study, the instantaneous dynamic contact angle (θ_d) is defined as the contact angle measured from the aqueous phase. Thus, the dynamic contact angle measured from the oil phase at that moment is represented by $(\pi - \theta_d)$. It is noted that the methods based on the ADSA may be unreliable when the TPCL is in a considerable motion since the object for the ADSA is supposed to be in a static or at least quasi-static state. Here, in light of the balance between the calculation cost and the accuracy of measurement needed in this study, three types of direct fitting methods, by adopting the simplest model of circular geometry, were employed to determine θ_d from the extracted contour. In what follows, the description of these methods is given.

As shown in **Figure 4-3a** and **Figure 4-4a**, a circle (green dash line) was fitted to the entire extracted contour of the oil-water interface on the image and the dynamic contact angle was obtained by calculating the intersection angle formed by this circle and the circle standing for substrate baseline (red solid line). This is called the circle fitting algorithm. For the local circle fitting algorithm, some local contour pixels from the TPCL point toward the droplet apex were fitted by a segment of a circle to determine the contact angle (**Figure 4-3b** and **Figure 4-4b**). A section of the circle was fitted to the droplet contour at the apex and extrapolated to the solid

surface for contact angle determination in the apex circle fitting algorithm (**Figure 4-3c** and **Figure 4-4c**). It is noted that the implementation of these three algorithms could provide consistent contact angles when the receding oil droplet is close to final static as shown in **Figure 4-3**. Nevertheless, significant discrepancy of the determined contact angles could be observed in the case of the rapid motion of the TPCL (**Figure 4-4**). More implications on these methods are discussed later in **Chapter 6**.

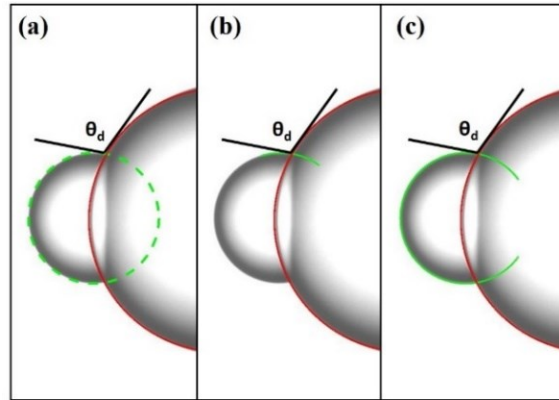


Figure 4-3: Visual demonstration of the contact measurement for the case of low TPCL velocity by adopting (a) the circle fitting, (b) local circle fitting and (c) apex circle fitting algorithms.

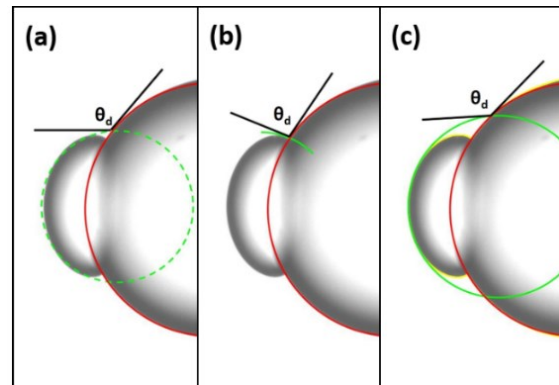


Figure 4-4: Visual demonstration of the contact measurement for the case of high TPCL velocity by adopting (a) circle fitting, (b) local circle fitting and (c) apex circle fitting algorithms.

Finally, a programmed loop was created to process each sequential image automatically, allowing the determination of the instantaneous oil-solid contact area and dynamic contact angles during the oil receding process.

4.3 Error analysis of contact angle measurement

In this section, several easily adjustable factors that may affect the outcome of the detected edge from digital image processing are thoroughly investigated to understand potential errors on the image-based contact angle measurement. In the following discussion, the same static configuration of the oil droplet as shown by **Figure 4-5** is consistently implemented to generate object profiles under various operational conditions for the error/sensitivity analysis of the contact angle measurement. This systematic error analysis is expected to offer guidance of recognizing suitable operational conditions for the image-based contact angle measurements in this study.

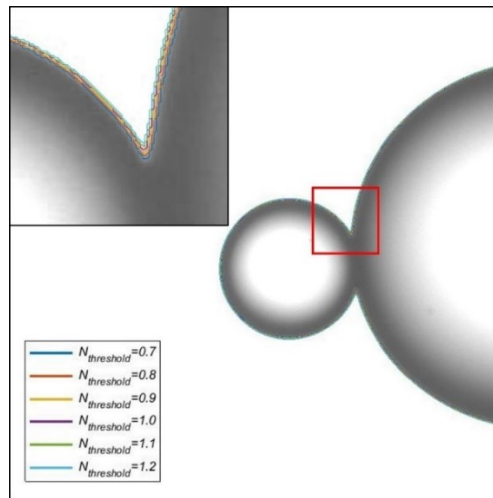


Figure 4-5: The detected edge profiles by adopting various $N_{threshold}$. The zoomed region of the meniscus near the TPCL enclosed in the red square is shown in the inset.

The digital image is represented by a two-dimensional array of pixels that are the basic elements of the image. For the 8-bit grayscale digital image used in this study, the intensity of an arbitrary pixel is stored as an integer between 0 and 255, which represent shades of gray from absolute black to white.[130] Normally, due to the strong contrast at the object boundary appearing on the image, the intensity for pixels across the object edge could change drastically. Therefore, the edge location on the image could be identified by a critical intensity that is called grayscale thresholding. In this study, the threshold grayscale intensity was evaluated by using the popular Otsu's method to minimize the intraclass variance of the black and white pixels.[131] To elucidate the dependence of measured contact angles on threshold grayscale intensities, here, six relative threshold grayscale intensities ($N_{threshold}$) with respect to the reference value obtained from the Otsu's method ($N_{threshold}$)

were selected for the error analysis. As indicated by **Figure 4-5**, all the detected edge profiles from adopting various $N_{threshold}$ are almost overlapped on the overall image. This is attributed to the sharp boundary of the captured image in this study. From the enlarged detail in the inset of **Figure 4-5**, it is seen that the detected edge profile could shift into water phase a little bit with the increase of $N_{threshold}$. The measurement results in **Figure 4-6** show that such shift of the detected edge could contribute to slightly larger measured contact angle. Therefore, the effect of the threshold grayscale intensity selection on the contact angle measurement is not distinct in this study.

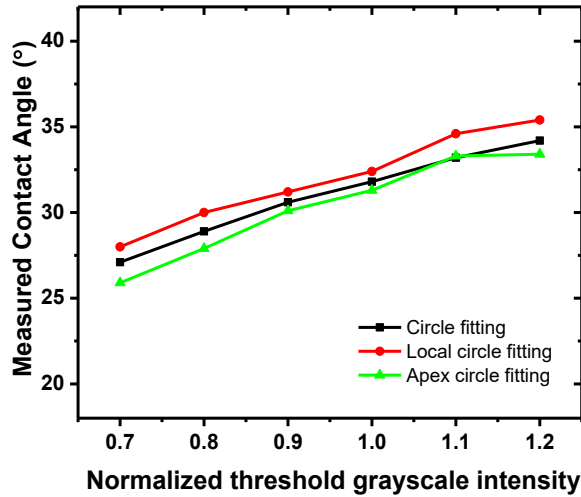


Figure 4-6: The measured contact angles by adopting various threshold grayscale intensities for the edge detection

The brightness of captured digital images is significantly dependent on some operational factors, such as exposure time and illumination intensity. As shown in **Figure 4-7**, at an identical condition of illumination intensity, a series of captured images of the displaced oil droplet (same as the state shown in **Figure 4-5**) show noticeable changes when different exposure times were applied. Clearly, longer exposure time could result in a brighter image. To gain knowledge of the sensitivity of the measured contact angle to the brightness of the image, the contact angles determined from these images were compared. **Figure 4-8** indicates that the slow variation of the measured contact angles is observed at short-exposure time; on the other hand, the measured contact angles exhibit more considerable sensitivity at increased exposure time. Moreover, the even longer exposure time of 210 ms led to the failure of the image-based contact angle measurement due to the nearly

disappeared contrast (**Figure 4-7h**). It could be implied that long exposure time should be avoided for image acquisition, as unreliable image analysis could arise from rather bright images with less contrast.

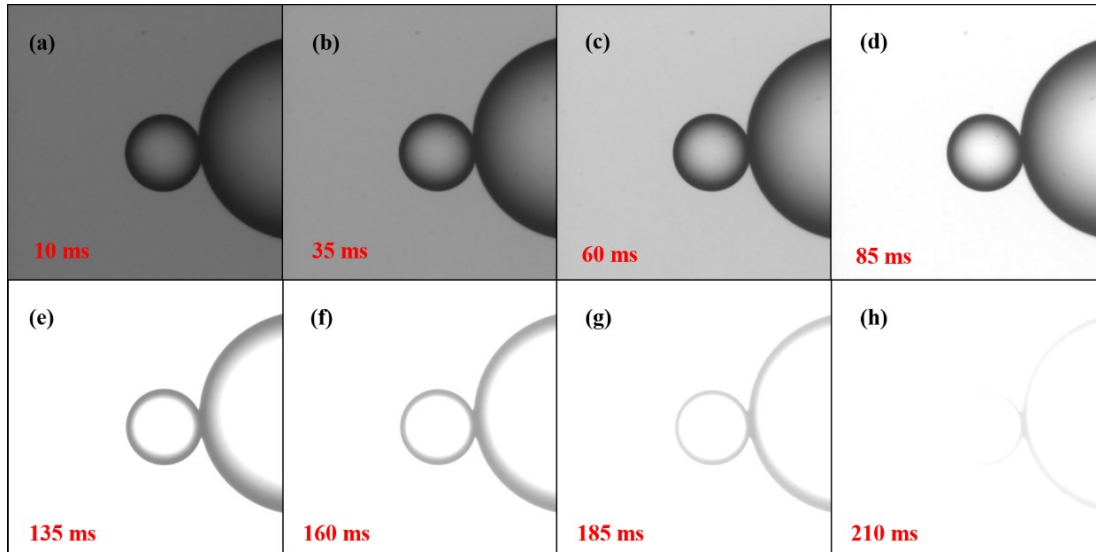


Figure 4-7: Images of the displaced oil droplet at the same state captured using exposure times of (a) 10 ms; (b) 35 ms; (c) 60 ms; (d) 85 ms; (e) 135 ms; (f) 160 ms; (g) 185 ms and (h) 210ms.

The exposure time for the image in **Figure 4-5** is 110 ms.

The focus adjustment is another common factor related to the quality of captured images. Here, attaining on-focus image is realized by adjusting the location of the objective lens relative to the object with the focus knob on the microscope. Setting the location at the on-focus condition to 0 mm as a reference, the objective lens was shifted away from that location to capture some out-of-focus images (**Figure 4-9**). It is seen that the out-of-focus shot led to blurred images and thereby introduced a large uncertainty of edge detection. The measured contact angles from these images as well as the on-focus one (**Figure 4-5**) are constructed in **Figure 4-10**. The measured contact angle was significantly changed on the out-of-focus image compared with the on-focus one. Moreover, an obvious quantitative error of the measurement appeared at the case far away from the on-focus condition (**Figure 4-9b&d**). Thus, it appears that guaranteeing the on-focus shot is essentially important for the contact angle measurement.

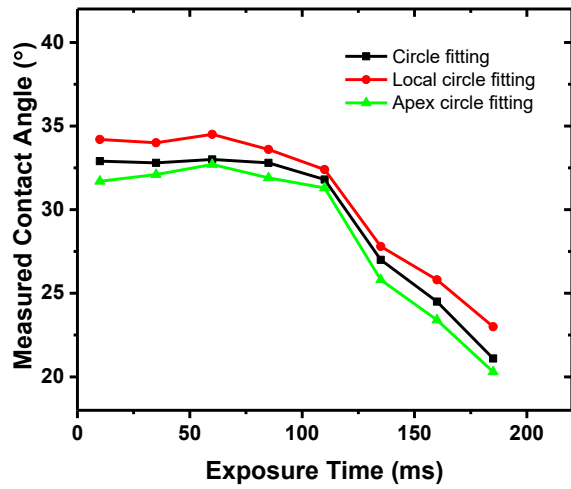


Figure 4-8: The contact angles measured from the captured digital images at different exposure time.

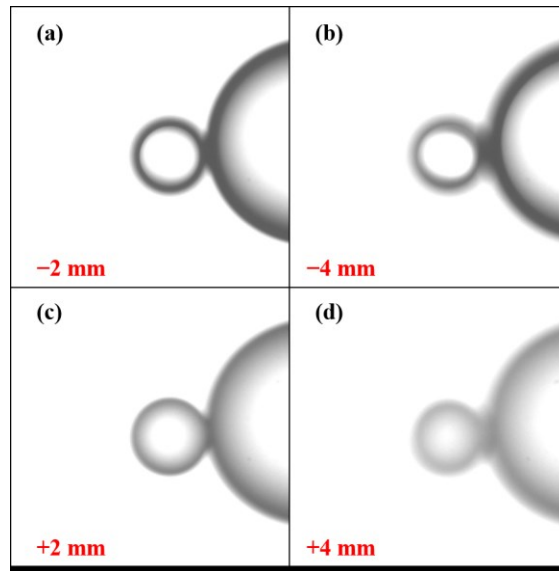


Figure 4-9: Images of the displaced oil droplet at the same state captured under out-of-focus conditions, where the location of the objective lens was shifted from the on-focus one in (a) -2 mm; (b) -4 mm; (c) $+2$ mm and (d) $+4$ mm. The on-focus image is shown in **Figure 4-5**.

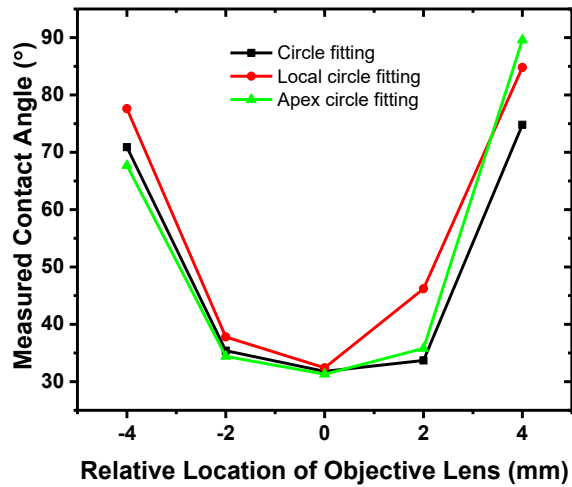


Figure 4-10: The contact angles measured from the digital images captured at different location of the objective lens as shown in **Figure 4-9**.

A comparison of the measured contact angles from different methods in **Figure 4-6**, **Figure 4-8** and **Figure 4-10** revealed that these methods exhibit similar sensitivity to those influential factors investigated in the study of error analysis. As a consequence, these methods generally could provide similar reliability for the purpose of the static contact angle measurement in this study.

4.4 Summary

With the digital image analysis, several parameters for the oil displacement characterization, including the oil-solid contact area, the velocity of the TPCL and the contact angle, were extracted. Three algorithms of circle fitting, local circle fitting and apex circle fitting were performed in this study to directly evaluate contact angles from extracted contours on images without considering physical properties. In the case of the slow TPCL motion, the determined contact angles from these algorithms showed consistency, while significant difference appeared when the TPCL moved fast. Because of the sharp boundary of oil-water and solid-water interfaces on the captured image, the measured contact angle was not sensitive to the threshold grayscale intensity for the edge detection. Another error analysis on several images of oil droplet at the same static configuration suggested that relatively shorter exposure time and on-focus shot during the digital image acquisition were

two crucial conditions to guarantee the reliable result of the image-based contact angle determination in this study.

Chapter 5

Drop shape relaxation analysis

5.1 Introduction

As the behavior of the oil displacement is highly correlated to the interfacial energy, knowing the relevant interfacial tension is an important prerequisite of gaining physical insight into the system. In practice, the interfacial tension at a fluid-fluid interface could be directly determined from a variety of experimental approaches. However, because of the extremely high viscosity of the oil in this study, it is difficult to measure the interfacial tension between the oil and the aqueous phase with conventional methods of tensiometry. For instance, the extremely long time needed for the oil drop to reach equilibrium caused by the slow viscous flow of the oil phase may limit the application of the pendant drop and spinning drop techniques; on the other hand, for force-based methods, such as du Nouy ring and Wilhelmy plate, a considerable viscous force arising from the high viscosity fluid flow should be considered to modify the force balance adopted for the interfacial tension calculation, however the evaluation of the viscous force is difficult.[132]

To overcome the difficulty of the interfacial tension measurement on high viscosity system with conventional methods, alternative methods based on dynamic behavior analysis have been developed to evaluate the interfacial tension, especially for the polymer-polymer interface. In principle, these methods take advantage of the kinetics of interfacial motion governed by interfacial tension as well as some other factors to obtain the interfacial tension. Depending on the extent of the deformation, generally, a viscous drop could display two distinct behaviors, breakup (**Figure 5-1**) or retraction (**Figure 5-2**). The theoretical analysis of any dynamic behavior is utilized for the interfacial tension determination from the corresponding experiments.[133] In this study, a method based on the analysis of drop retraction/relaxation dynamic behavior, which is named “drop shape relaxation method”, is applied to determine the interfacial tension between high viscosity oil and aqueous phase. With a negligible body force, a deformed drop suspended in another immiscible fluid could reshape into a spherical shape with time. The drop shape recovery

process is driven by the interfacial tension between the fluids and retarded by the fluid viscosity. As a result, with the known fluid viscosity, the interfacial tension is evaluated by analyzing the dynamic behavior of the drop observed in the corresponding experiment.

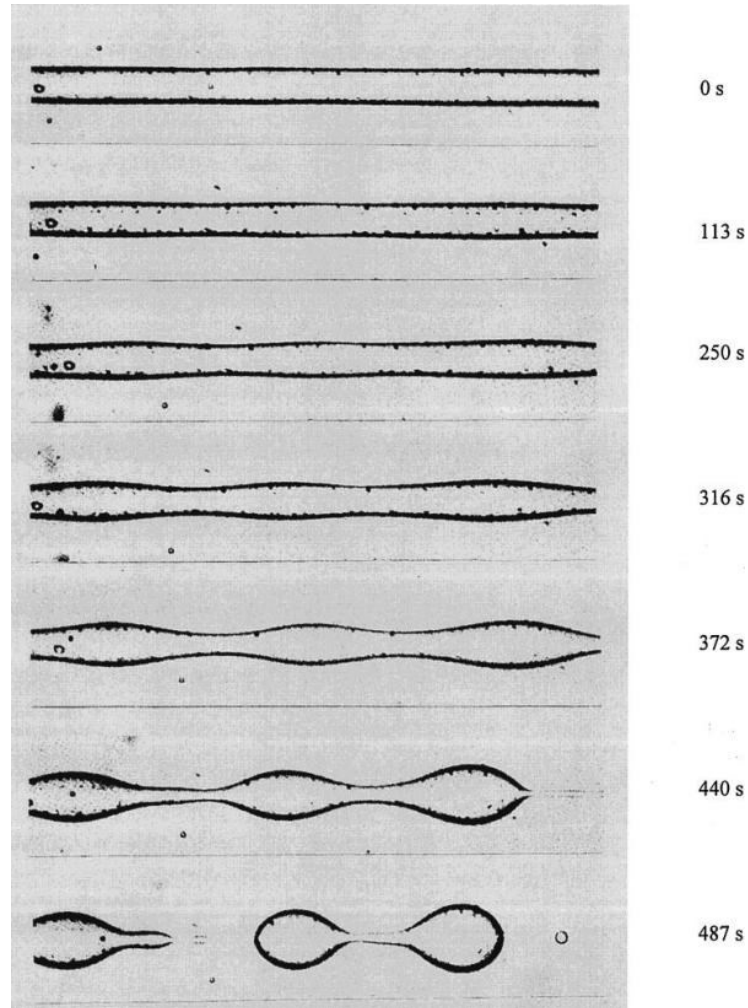


Figure 5-1: The process of a highly deformed drop breakup. [133]

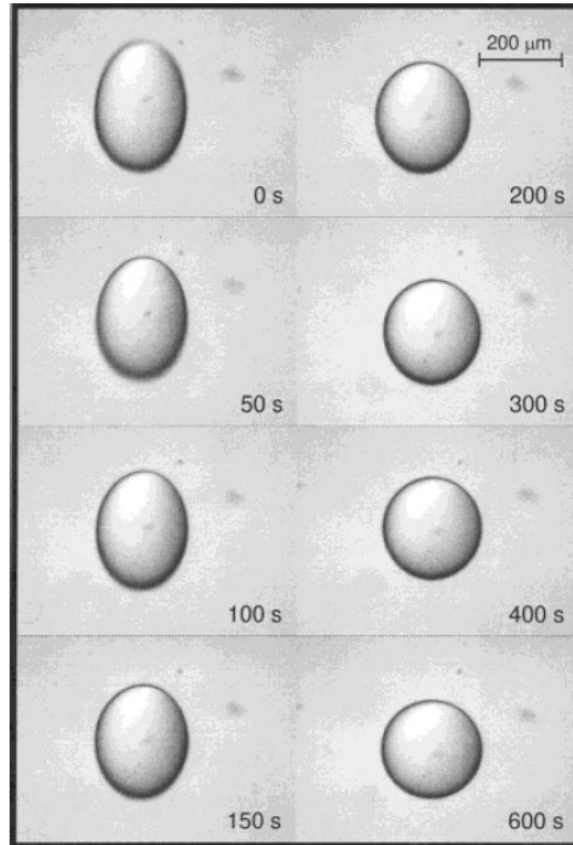


Figure 5-2: The process of a gently deformed drop retraction.[134]

In this chapter, several theoretical analyses of drop relaxation are briefly revisited, and a boundary least square method is introduced to analyze an axis-symmetrically deformed drop shape relaxation in a quiescent aqueous phase within the limit of Stokes flow. A custom-programmed Matlab® code was developed to implement this analysis for the numerical solution of the drop shape evolution. For the experiments, a distorted micrometer-sized oil droplet was generated by applying suction on the opposite sides of the droplet through two glass micropipettes; and subsequently, the oil droplet retraction was triggered by the sudden removal of the suction. This simple method avoided the use of an advanced device to obtain such kind of droplet deformation by generating complex flow. In the end, the experimental data was matched with the theoretical analysis to determine the interfacial tension, which was also performed by a custom-programmed Matlab® code.

5.2 Axisymmetric drop shape relaxation analysis

5.2.1 Review

The theoretical analysis of a deformed axisymmetric drop shape relaxation process has been performed by some researchers. Their works have provided useful mathematical models for the quantitative description of the relaxation process associated with the interfacial tension evaluation.

Carriere and Cohen[135] [136] brought forward an empirical model to predict the relaxation process of a drop with a spherocylinder shape initially (a cylinder capped by two semispherical on both ends),

$$f_{cc} \left(\frac{R_e}{R_d} \right) - f_{cc} \left(\frac{R_{e0}}{R_d} \right) = \frac{2.7t\gamma}{(\mu_e + 1.7\mu_i)R_d} \quad (5-1)$$

where μ_i and μ_e are viscosities of interior and exterior fluids respectively, t is time, γ is the interfacial tension between the two fluids, R_d is the radius of the drop as a sphere at equilibrium state, R_e is defined as the equivalent radius and R_{e0} is R_e at the initial time ($t=0$ s). The following equation of volume preservation could be utilized for the evaluation of R_e ,

$$\frac{4}{3}\pi R_d^3 = 2 \left[\pi R_e^2 \left(\frac{H}{2} - R_e \right) + \frac{2}{3}\pi R_e^3 \right] \quad (5-2)$$

where H is the overall length of the drop. The function $f_{cc}(x)$ in **Equation (5-1)** is expressed as,

$$f_{cc}(x) = 1.5 \ln \frac{\sqrt{1+x+x^2}}{1-x} + \frac{3^{1.5}}{2} \tan^{-1} \left(\sqrt{3} \frac{x}{x+2} \right) - \frac{x}{2} - \frac{4}{x^2} \quad (5-3)$$

Using Rallison's theoretical approach for objects at small deformation[137], Luciani et al.[134] and Guido et al.[138] developed another model to characterize the relaxation process of a slightly deformed spheroid drop,

$$D_d/D_{d0} = \exp \left[- \frac{40 \frac{\mu_i}{\mu_e} \left(\frac{\mu_i}{\mu_e} + 1 \right)}{\left(2 \frac{\mu_i}{\mu_e} + 3 \right) \left(19 \frac{\mu_i}{\mu_e} + 16 \right) \mu_i R_d} t\gamma \right] \quad (5-4)$$

where D_d is the deformation parameter which is defined as,

$$D_d = \frac{a-b}{a+b} \quad (a > b) \quad (5-5)$$

where a and b are two principal semi-axes of the spheroid with different lengths on the projected view.

Although the models mentioned above are simple and convenient to use, both suffer from critical disadvantages which could potentially limit their application: the first empirical model is unreliable when there is a viscosity considerable difference between two fluids [139] and the latter is only suitable for slightly deformed drop[133]. Therefore, a more sophisticated analysis is needed to deal with the more general situation for general applications.

Essentially, instantaneous fluid velocity fields associated with the evolution of the oil drop shape are governed by the famous Navier-Stokes equations. As a result, theoretically, the evolution of the drop shape could be evaluated by solving these equations with appropriate boundary conditions. Unfortunately, in most cases, it is difficult to obtain the analytical solution of the full Navier-Stokes equations due to its intrinsic complexity. In practice, numerical methods are normally adopted to solve these equations. The powerful finite element analysis, which is believed to be a general method to deal with numerical fluid mechanics problem, typically consumes a large amount of computational time, and hence, is not economical for this study. Boundary integral method (BIM) has been shown to be accurate and efficient in the study of free boundary problems (e.g., the transient motion of interface at low Reynolds number).[140] By using this method, Stone et al.[141] and Tjahjadi et al.[142] have successfully obtained the theoretical drop shape during the drop relaxation process. Unfortunately, such a method is inadequate to deal with the case of two immiscible fluids with extremely high or low viscosity ratios, which is the case in this study.[143] [144] Here, an alternative, so-called boundary least squares (BLS) method, which is applicable to the case of arbitrary viscosity ratio was implemented to obtain numerical solutions of the transport equations governing the drop shape evolution and predict the relaxation of an axis-symmetrically deformed drop.[145] [146] The description of this method is presented in detail in the next section.

5.2.2 Theoretical calculation with boundary least squares method

On an assumption of the negligible inertial and body forces, the dynamics of the drop shape reaction is governed by the following creeping motion equations simplified form the full Navier-Stokes equations

$$\mu_i \Delta \mathbf{v}_i = \nabla p_i, \quad \nabla \cdot \mathbf{v}_i = 0 \quad (5-6)$$

$$\mu_e \Delta \mathbf{v}_e = \nabla p_e, \quad \nabla \cdot \mathbf{v}_e = 0 \quad (5-7)$$

where \mathbf{v} and p are the velocity and pressure fields, and subscript i and e denote interior and exterior phases, respectively.

At the interface of two immiscible liquids, the continuity of velocities and the balance of mechanical stress must be satisfied. Therefore, two boundary conditions are imposed at the interface,

$$\mathbf{v}_i = \mathbf{v}_e \quad (\text{at interface}) \quad (5-8)$$

$$\boldsymbol{\sigma}_i - \boldsymbol{\sigma}_e + \mathbf{T} = 0 \quad (\text{at interface}) \quad (5-9)$$

where $\boldsymbol{\sigma}_i$ and $\boldsymbol{\sigma}_e$ are the hydrodynamic tractions from interior and exterior phase respectively, and \mathbf{T} is the normal stress on the interface arising from interfacial tension.

In the case of axisymmetric velocity and pressure fields, the analytical solutions of **Equation (5-6)** and **Equation (5-7)** at spherical coordinates (R, β, Φ) have been found by Happel et al.[147],

$$v_{R,i} = - \sum_{n=2}^{\infty} (A_n R^{n-2} + C_n R^n) P_{n-1}(\cos \beta) \quad (5-10)$$

$$v_{\beta,i} = \sum_{n=2}^{\infty} [n A_n R^{n-2} + (n+2) C_n R^n] \frac{G_n(\cos \beta)}{\sin \beta} \quad (5-11)$$

$$p_i = \Pi - 2\mu_i \sum_{n=2}^{\infty} \frac{2n+1}{n-1} C_n R^{n-1} P_{n-1}(\cos \beta) \quad (5-12)$$

$$v_{R,e} = - \sum_{n=2}^{\infty} (B_n R^{-n-1} + D_n R^{-n+1}) P_{n-1}(\cos \beta) \quad (5-13)$$

$$v_{\beta,e} = - \sum_{n=2}^{\infty} [(n-1) B_n R^{-n-1} + (n-3) D_n R^{-n+1}] \frac{G_n(\cos \beta)}{\sin \beta} \quad (5-14)$$

$$p_e = -2\mu_e \sum_{n=2}^{\infty} \frac{2n-3}{n} D_n R^{-n} P_{n-1}(\cos \beta) \quad (5-15)$$

where $P_n(x)$ and $G_n(x)$ are the Legendre and Gegenbauer polynomials respectively, A_n, B_n, C_n, D_n and Π are arbitrary constants which could be determined from boundary conditions. It is noted that the solutions are given by infinite sums as the integer n goes to infinity. However, in practice, a finite maximum n (n_{\max}) must be imposed to truncate the exact solutions and hence obtain approximated ones. In the solutions, the subscripts R and β represent two resolved components of a vector in the spherical coordinate system. Due to the axial symmetry, the third component of the azimuthal angle Φ is eliminated.

In principle, the BLS method was used to identify the optimal arbitrary constants truncated at n_{\max} . In the analysis, the arbitrary constants were represented by a vector $a_i = \{\Pi, A_n, B_n, C_n, D_n\}$ and the parameter M_{BLS} was defined as half of the value obtained by integrating the sum of squares of the two boundary conditions (**Equation (5-8)** and **Equation (5-9)**) over the interfacial region,

$$M_{\text{BLS}} = \frac{1}{2} \int_{\text{interface}} [(\mathbf{v}_i - \mathbf{v}_e)^2 + (\boldsymbol{\sigma}_i - \boldsymbol{\sigma}_e + \mathbf{T})^2] dS \quad (5-16)$$

Theoretically, M_{BLS} must be equal to 0 at the condition of infinite arbitrary constants. Here, the vector a_i with finite parameters can be approximately evaluated by minimizing M with respect to a_i . Thus, a_i could be determined by finding the zero first derivative of M_{BLS} with respect to a_i ,

$$\frac{\partial M}{\partial a_i} = \int_{\text{interface}} \left[(\mathbf{v}_i - \mathbf{v}_e) \cdot \frac{\partial (\mathbf{v}_i - \mathbf{v}_e)}{\partial a_i} + (\boldsymbol{\sigma}_i - \boldsymbol{\sigma}_e + \mathbf{T}) \cdot \frac{\partial (\boldsymbol{\sigma}_i - \boldsymbol{\sigma}_e + \mathbf{T})}{\partial a_i} \right] dS = 0 \quad (5-17)$$

With the determined a_i , the velocity and pressure fields at this moment were readily attained with the Happel's solutions. Finally, the temporal evolution of the drop shape could be reasonably estimated, once the velocity of the interface at any moment was identified.

In this study, this theoretical analysis was carried out numerically using a personal computer. More detailed numerical implementations regarding this calculation are given in **Appendix A**.

5.2.3 Calculation results and validation

First, the BLS method was used to obtain a theoretical relaxation process of an axisymmetric spheroid drop shape. For this calculation, the initial axial ratio (a_0/b_0) of the spheroid was set to 1.8 and the viscosity of the drop fluid was assumed to be much larger than that of the continuous fluid. For the calculation, the following parameter setting was used: n_{\max} is 60; Δt_c is 0.05; the

maximum t_c at the end of the calculation is 6 and the total number of the nodal points to describe the drop profile at one side of the axis (n_p) is 181. The result showed that the total computing time on the personal computer equipped with Intel Core i5-2500K dual-core processor (2×3.3 GHz) was only around 5 seconds. It is indicated that the BLS method is a highly efficient method for the drop shape relaxation analysis.

In **Figure 5-3**, the evolution of the drop shape from the computation discussed in **Section 5.2.2** is presented at several dimensionless computational times (t_c). It can be seen that the calculated drop shape gradually evolved into a perfect sphere, which is in agreement with the real experimental behavior and thus provided preliminary validation of this theoretical analysis.

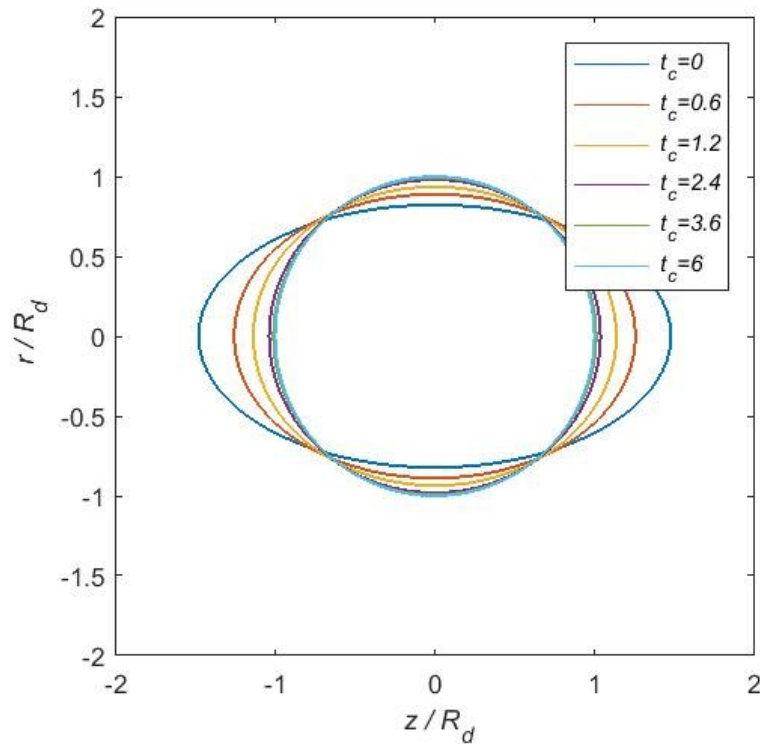


Figure 5-3: The theoretical drop profile at several dimensionless times during the relaxation from an initial spheroid shape using the BLS method.

Two additional self-consistency checks for the result of this analysis were performed: as indicated by **Figure 5-4a**, the slightly changed drop volume tracked at each incremental time step confirmed the mass conservation during calculation; meanwhile, in **Figure 5-4b**, the insignificant shifts of

the theoretical curves from the calculation by adjusting Δt_c to larger 0.1 or smaller 0.01 suggested that $\Delta t_c=0.05$ is adequate for the Euler-type integration.

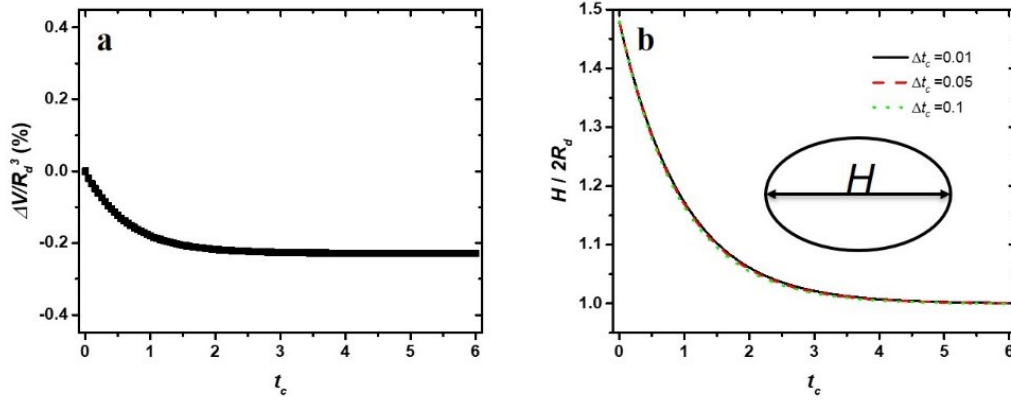


Figure 5-4: The results of two self-consistent checks for the BLS method: (a) the dimensionless drop volume in the calculation changes as function of t_c and (b) the plots of the dimensionless length of the drop on symmetric axis (H) versus t_c obtained in the calculations with adopting different Δt_c for the Euler-type integration.

In **Figure 5-5**, when a_0/b_0 was set to be 1.2, the satisfactory agreement between the analysis result of the BLS method and the theoretical line predicted by **Equation (5-4)** at various viscosity ratios could be found. This further demonstrated that the BLS method was reliable and convincing.

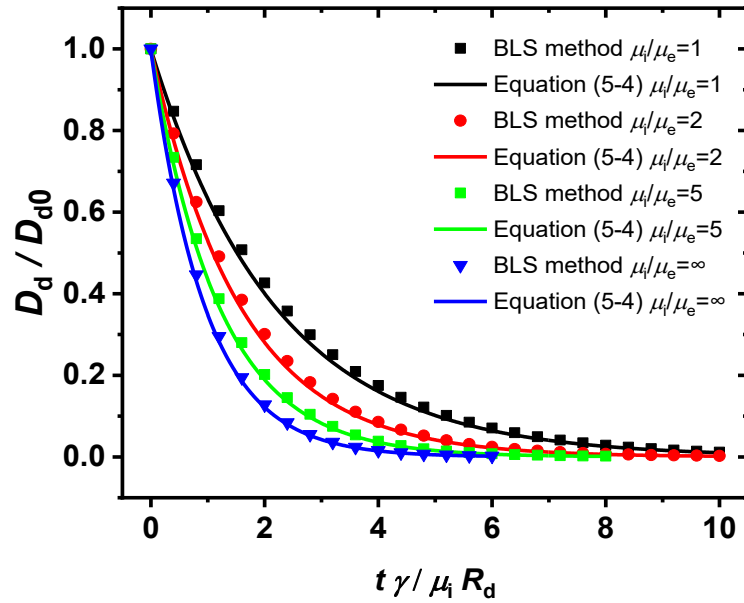


Figure 5-5: Comparison between the temporal evolution of D_d/D_{d0} calculated from the BLS method and that predicted from **Equation (5-4)** at various viscosity ratios.

For the arbitrary axisymmetric drop shapes, as shown in **Figure 5-6**, computation errors did not appear from the analysis of the BLS method. It was seen that reasonable results were obtained from the calculations, as the arbitrary drop shapes could finally evolve into a perfect sphere. Thus, it appears that the BLS method can handle the case of an arbitrary axisymmetric drop shape relaxation properly.

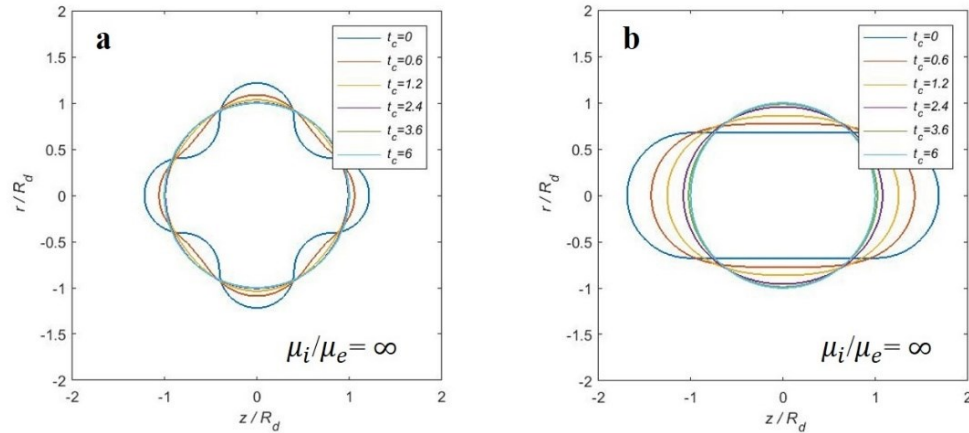


Figure 5-6: The theoretical drop profile at several dimensionless times during the relaxation from an initial shape of (a) “flower” and (b) spherocylinder using the BLS method.

5.3 Interfacial tension measurement

5.3.1 Micrometer-sized drop shape relaxation experiments

The micropipette system discussed in **Section 3.5** for microscale oil displacement experiments was adopted to conduct the micrometer-sized oil drop shape relaxation experiments. Similar to the procedure of the microscale curved glass substrate fabrication, a glass tip with a tapered end was obtained by stretching a micropipette (100 microliters) with hot wire pipet puller. The tapered end was truncated by a homemade forging apparatus to produce a glass tip with an open end of approximately 10 μ m diameter. Two such micropipettes were mounted on the micromanipulator with the micrometer-sized open ends opposite to each other. Meanwhile, the other untreated sides of the micropipettes were connected to syringes respectively through flexible plastic tubes. By operating the syringe, negative or positive pressure at the micrometer-sized open end could be created to provide suction or release of an oil droplet, respectively. Prior to the experiment, the micrometer-sized open ends were placed into an aqueous solution with suspended micro-sized oil droplets. Subsequently, one oil droplet was selected and sucked from opposite sides by micropipettes and elongated axially as shown in **Figure 5-7a**. The relaxation experiment was initiated by releasing one side of oil from the pipette (**Figure 5-7b**) and then the axially deformed oil droplet relaxed into a sphere in the solution with time (**Figure 5-7b~d**). The evolution process was captured by a CCD camera. It is mentioned that the size of the oil droplet in this experiment

was at the order of $10\mu\text{m}$, and hence the typical Bond number (ratio of body force to capillary force) and Weber number (ratio of inertial force to capillary force) in this process could be around 10^{-4} and 10^{-9} , respectively. The negligible body and inertial forces reflected by these dimensionless numbers were in accord with the assumption in the BLS method mentioned above. Therefore, the theoretical prediction of such relaxation process was attained by performing the BLS method.

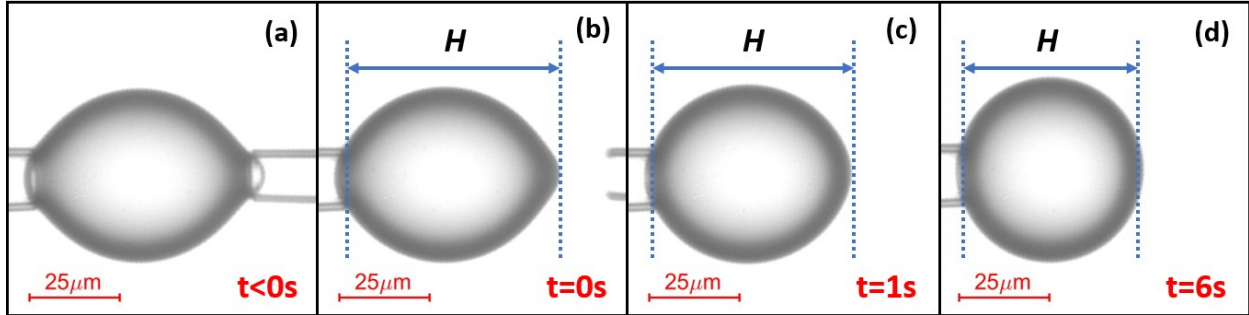


Figure 5-7: Snapshots illustrating the micrometer-sized oil drop shape relaxation in the micropipette system.

5.3.2 Digitized initial drop shape extraction

Prior to performing the BLS method, the digitized initial experimental drop profile should be extracted from the captured image at a certain time set as the initial time of the experiments through the digital image analysis. Similar to the methodology of the contact angle measurement mentioned in **Section 4.2**, the contours of the oil drop and the glass pipette were extracted through grayscale thresholding (**Figure 5-8a**) and stored in the form of consecutive edge pixel coordinates. As indicated by **Figure 5-8b**, the extracted contour of the oil and the pipette were separated by two points located by searching for two maxima in the second derivative variation of the edge coordinate function. Subsequently, the profile of the drop was divided into two axisymmetric parts indicated by red and green lines, respectively, in **Figure 5-8c**. However, in this case, these two parts could never be absolutely axisymmetric. In practice, either of them was selected as the extracted drop shape. As discussed in **Appendix A**, the extracted initial drop shape was characterized by the cylindrical coordinates in the form of closely spaced nodal points (r_i, z_i) along the meridian curve for the numerical BLS method. **Figure 5-8d** shows the extracted drop shape obtained from this procedure in the cylindrical coordinate system. It is mentioned that the coordinates could be easily converted to physical units through the factor of $0.4644\mu\text{m}/\text{pixel}$.

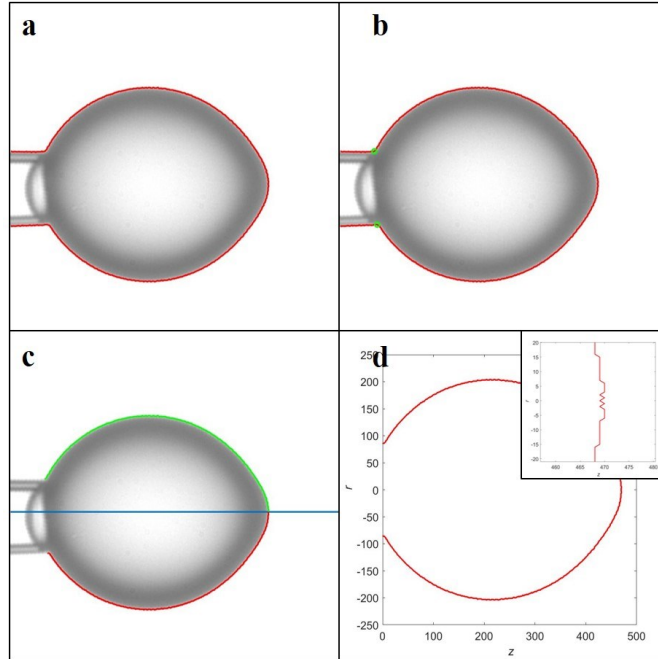


Figure 5-8: Visual demonstration of some major steps to extract the experimental drop shape from the digital image for the BLS method. The zoomed region of the directly extracted drop profile at the apex is shown in the inset of (d).

The unavoidable noise along the nodal points could appear on the directly extracted drop profile as shown in the inset of **Figure 5-8d**. For the calculation, such noise could yield the discontinuity of the calculated numerical curvature of the interface (J_c) along the nodal points and thereby fail the BLS method. To address this issue and validate the BLS method by achieving the continuous numerical curvature of the interface, a data smoothing algorithm was applied for the slight redistribution of the nodal points on the coordinates. As shown in **Figure 5-9**, for the plot of the original data, the significant variation of the numerical curvature along the nodal points could be observed. It could be seen that the conventional smoothing algorithm could only weaken but not fully eliminate such variation.

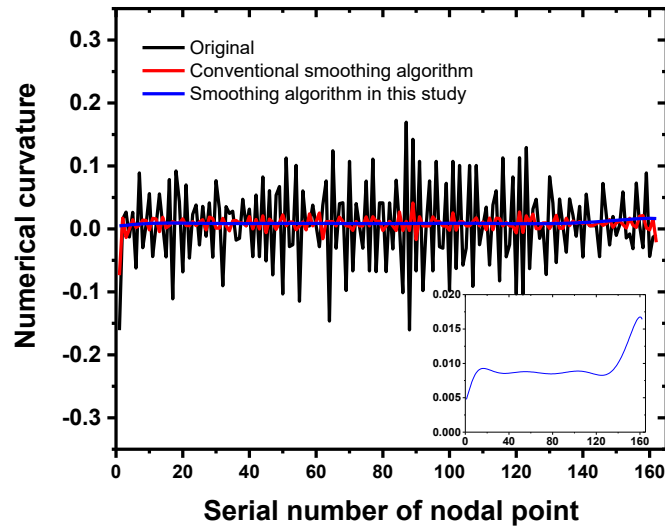


Figure 5-9: The calculated numerical curvature along the nodal points. The detailed description of the evaluation of J_c refers to **Appendix A**.

To avoid the failure of the BLS method dealing with the extracted drop shape from the experiment, more sophisticated smoothing algorithm was implemented as follows: the nodal points with the cylindrical coordinates (r_i, z_i) were first translated into spherical coordinates (R_i, β_i) ; an eighth-order polynomial (such model may not be optimal, but it works quite well here) was used to fit the function $R_i=f_{R_i}(\beta_i)$ associated with the constraint of $df_{R_i}(\pi)/d\beta=0$ in the form of the Lagrange multiplier due to the axisymmetric nature of the drop shape; new spherical coordinates $(R_{i,s}, \beta_{i,s})$ for the nodal points could be evaluated using the obtained best fitting polynomial and then translated back into new cylindrical coordinates $(r_{i,s}, z_{i,s})$. It could be seen that the smoothed drop profile from this algorithm was highly similar to the untreated one in general (**Figure 5-10a**) but rather smooth in detail (**Figure 5-10b**). Also, as shown by **Figure 5-9**, the anticipated continuous numerical curvature was obtained after such processing.

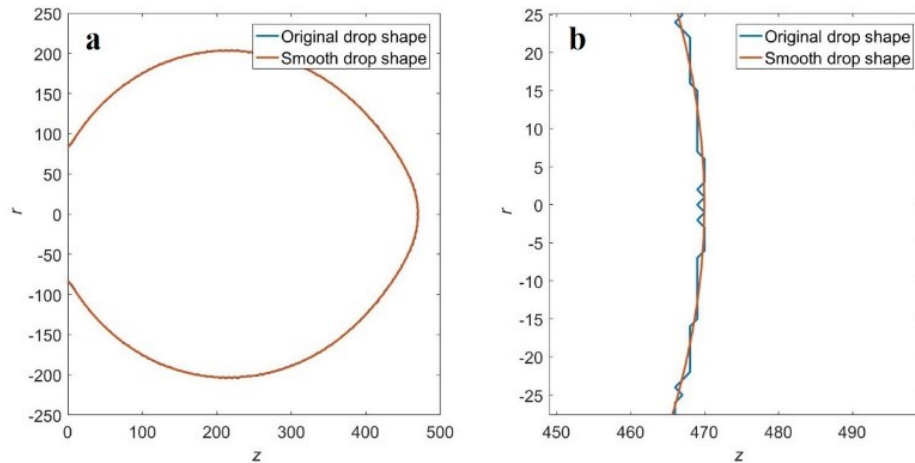


Figure 5-10: Comparison of the extracted drop profile without and with smoothing process from (a) an overall view and (b) an enlarged view at the apex.

5.3.3 Interfacial tension evaluations

The BLS method was performed to theoretically analyze the temporal evolution of the smoothed initial drop shape extracted from the experiment as shown in **Figure 5-11**. As indicated by **Figure 5-7**, the lengths of the oil droplet along the symmetric axis (H) were measured at different experimental times. By adjusting γ/μ , the measured experimental data was plotted in a dimensionless form to match the theoretical curve obtained from the BLS method as shown in **Figure 5-12**. With the determined optimal value of γ/μ from the experimental data fitting as well as the known μ , γ could be readily evaluated.

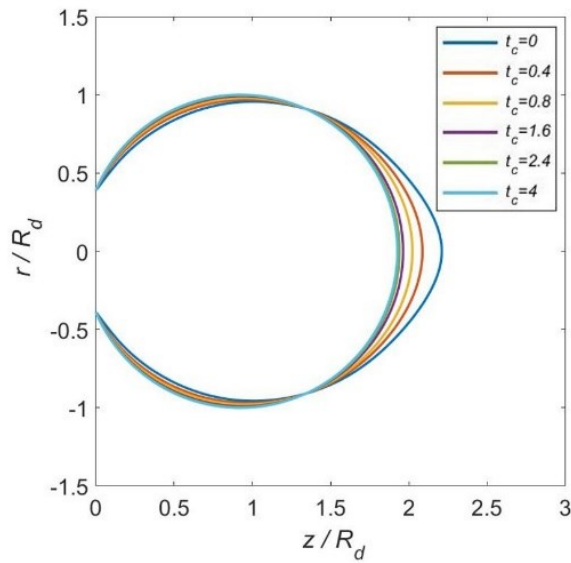


Figure 5-11: The theoretical drop profile at several dimensionless times during relaxation from the extracted initial shape from the experiment with performing the BLS method.

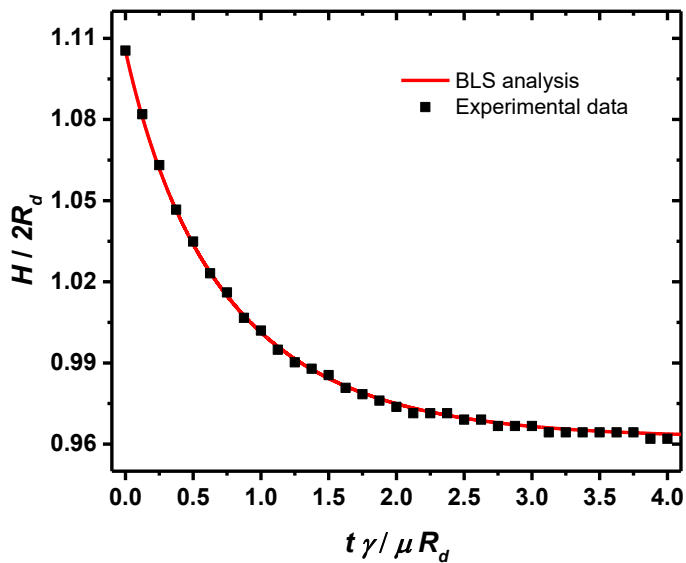


Figure 5-12: Determination of the interfacial tension by matching experimental data with the theoretical curve obtained by the BLS method.

The interfacial tensions against pure water of the high viscosity oils used in this study were measured by this drop shape relaxation method at 20°C and the results are given in **Table 5-1**. It could be seen that these model oil samples with the distinct difference of viscosity exhibit similar

interfacial properties against water. The measured interfacial tensions in the presence of surfactants will be presented in **Section 7.2.1**.

Table 5-1: The measured interfacial tension between the high viscosity oils and water

Model oil	N190000	N450000	N2700000
Oil-water interfacial tension (mN/m)	37±2	36±3	34±3

5.4 Summary

To determine the interfacial tension between the high viscosity oil and the aqueous phase, the drop shape relaxation method was used in this study. In principle, this method consists of the theoretical analysis as well as the experimental data collection and matching. For the theoretical part, the creeping motion equations governing the dynamic process of an axisymmetrically deformed drop restoring into an equilibrium spherical shape have been solved by the BLS method numerically. The BLS method has been demonstrated to be a highly efficient technique to analyze the relaxation process of arbitrary axisymmetric drop shape. In the experimental aspect, a micrometer-sized sample oil droplet was elongated to create an axisymmetric deformation with the micropipette system. The initial oil drop profile was extracted from the image captured after initiating the relaxation experiments and then smoothed with a special algorithm for the BLS method. By matching the experimental data of the temporal evolution of drop shape with the theoretical value from the BLS method, interfacial tensions were determined. The measured interfacial tensions between oil and water suggest that three high viscosity model oil samples have similar interfacial tensions against water despite distinct viscosities.

Chapter 6

Oil displacement in pure water

6.1 Introduction and motivation

The displacement of a fluid from a solid surface in an immiscible fluid has been the subject of considerable research over the past several decades. In the past, experimental studies of the displacement process have been focused mainly on how the wetted area of one fluid on the solid surface in air-equilibrated with the liquid vapor evolved with time. Such dynamic behavior is frequently described by the velocity of the TPCL displacement.

Numerous investigations were conducted to understand the displacement dynamics, in particular for the spreading of nonvolatile liquid droplets on smooth solid surfaces. [40] [148] [149] [150] The spreading process has been considered to be driven by the capillary force. The surface tension and viscosity of the liquid were shown to be the key factors in determining the displacement dynamics of the TPCL. For the displacement of immiscible liquids on solid surfaces, the viscosity ratio of the two liquids was verified to play an important role in the liquid-liquid displacement.[57] The intrinsic correlation of the TPCL displacement in liquid-air and liquid-liquid systems has been obtained.[50] [51] More recently, the displacement of liquids on solid substrates of considerable surface roughness was studied to understand the influence of surface nanostructure on wetting dynamics. [14] [151] [152]

The dynamic contact angle formed between the fluid-fluid and fluid-solid interfaces at the moving TPCL commonly serves as an important descriptor for the system. The dependence of dynamic contact angle on the TPCL displacement velocity is frequently investigated for model establishment.[37] [153] The dynamic contact angle determines the instantaneous geometry of the droplets on the solid surface. From a thermodynamic point of view, it is generally accepted that a static liquid droplet on a smooth and homogeneous surface with insignificant gravitational effect could form a spherical cap to minimize its surface energy. Similarly, the dominant capillary force could keep the droplet shape as a spherical cap at any moment even when the TPCL moves on

solid surfaces. Consequently, the dynamic droplet shape has been treated traditionally as a spherical cap during spontaneous displacement of droplet in the wetting/dewetting process. In fact, such consideration of the dynamic drop shape, also known as “quasi-static spherical cap approximation”, has been widely used in studying dynamics of a sessile drop spreading or receding on a solid surface, [56] [108] [154] [155] [156] as it greatly simplifies analysis of dynamic contact angles. However, such treatment could result in a poor or even erroneous estimation in some cases due to considerable body force[157] or inertia.[104]

Most recent studies on displacement dynamics of TPCLs on solid surfaces are restricted to the spontaneous wetting of liquids with low or intermediate liquid viscosity. In such cases, the viscous force is a major rate-limiting mechanism but plays a limited role on the macroscopic shape of moving meniscus as compared with the dominant capillary force. However, wetting systems may involve extremely high viscosity liquids in some applications, such as polymer melts or heavy crude oil. A significant viscous force may arise from the flow of high viscosity liquids and exhibit unexpected wetting behavior. It is therefore necessary to develop deep understanding on microscale liquid-liquid displacement under considerable viscous force and expand comprehensive knowledge of spontaneous wetting phenomenon to high viscosity fluid systems.

The objective of this chapter is to determine microscale displacement dynamics of high viscosity oil droplet on highly curved smooth solid surface by an aqueous medium. This investigation was initially performed to explore the bitumen liberation dynamics during water-based oil sands extraction process[25] [111] [158] and then expected to improve the general knowledge regarding high viscosity liquid spontaneous wetting dynamics. The effects of system parameters such as solid wettability, oil viscosity, surface curvature and oil volume on microscale displacement dynamics were investigated. The popular “quasi-static spherical cap approximation” was challenged for describing dynamic droplet shape of high viscosity oil in an aqueous medium and a new methodology for image-based dynamic contact angle determination was developed. Finally, widely used MK and HD models were applied to quantitatively analyzing the experimental observations.

6.2 Results and discussion

6.2.1 Degree of liberation.

In this section, the influence of some system parameters such as surface wettability, oil viscosity, substrate surface curvature and oil droplet volume on the oil displacement process was investigated by comparing the temporal evolution of D_L . To more efficiently determine how much oil was displaced by water on the surface, the degree of oil liberation (D_L) defined below (**Equation (6-1)**) was used to present the experimental results:

$$D_L(t) = \frac{A_0 - A(t)}{A_0} \times 100\% \quad (6-1)$$

where A_0 and $A(t)$ are the initial and the instantaneous oil-solid contact areas, respectively. In this study, the static advancing contact angle θ_s refers to the final contact angle measured from the aqueous phase. The instantaneous dynamic contact angle θ_d was also determined through the aqueous phase by the digital image processing. The dynamic contact angle measured through the oil phase was therefore given by $(\pi - \theta_d)$.

In this section, the influence of some system parameters such as surface wettability, oil viscosity, substrate surface curvature and oil droplet volume on the oil displacement process was investigated by comparing the temporal evolution of D_L . Glass tips of distinct surface wettability as described previously were first used to investigate the influence of surface wettability on oil receding process. The receding oil (N450000) exhibited different final static contact angles on these glass substrates in water (**Table 6-1**). The semi-logarithmic plot of D_L as a function of experimental time is shown in **Figure 6-1a**. Clearly, both final D_L and dynamics of oil liberation are sensitive to the wettability of the solid surface. Slower oil displacement rate and lower ultimate D_L were observed on more hydrophobic surface, which implies that increasing hydrophobicity of the solid surface is a crucial factor to hinder oil receding in both static and dynamic perspectives.

Figure 6-1b shows the results of oil receding experiments using three high viscosity oils (N190000, N450000 and N2700000). These model oil samples have distinct difference in viscosity but similar interfacial properties. In this case, the oil viscosity is the only prominent factor that alters the oil receding behavior. The faster receding of oil contact area observed with less viscous oil demonstrates that the viscosity of oil is an important limiting mechanism for the oil receding

dynamics. However, the impact of viscosity on the final static state of the oils on the solid is negligible as revealed by nearly identical ultimate D_L as anticipated.

The effect of macroscopic surface geometry on D_L was investigated by conducting the experiments using the oil (N450000) on the spherical solid surfaces of different surface radii while keeping the other properties the same. The results in **Figure 6-1c** show a negligible effect of the substrate curvature on microscale oil receding. Interestingly, a slightly slower rate of oil liberation has been observed on the more curved surface. One possible interpretation for the slower receding rate was the longer moving distance of the whole oil droplet to reach the final state, which could be recognized by the shift in the center of gravity position of the droplet. Solving the governing hydrodynamic equations with a TPCL singularity alleviating model could shed the light on the underlying mechanism. To investigate the effect of oil drop size, different amounts of model oil samples (N450000) were deposited onto the identical solid surface. The results in **Figure 6-1d** show that reducing the oil volume could accelerate the oil receding process but has a negligible impact on the ultimate D_L .

Table 6-1: Static contact angle of N450000 on various solid surfaces with wettability modification in water

Used chemicals	Sodium hydroxide solution (pH = 12)	Without treating	1 wt.% DCDMS in toluene solution		
Treating time (s)	7200	-	1	30	120
Static contact angle (°)	28±2	39±3	58±2	91±1	104±4

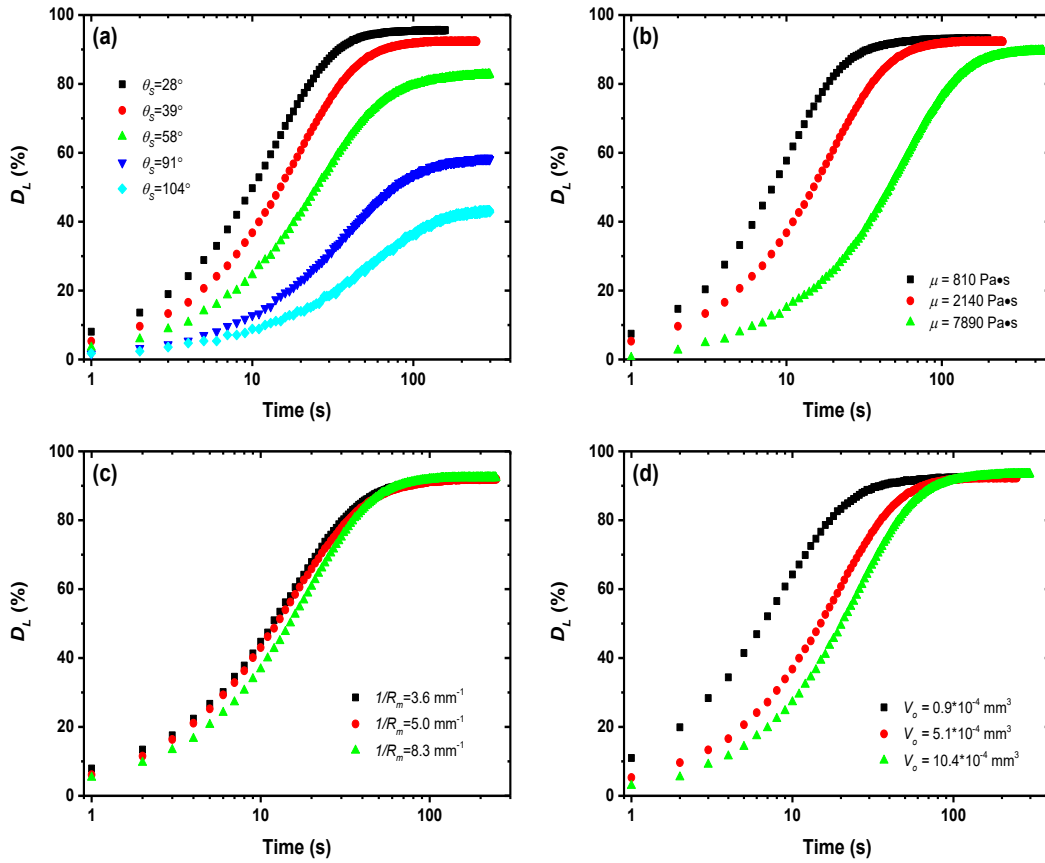


Figure 6-1: Semi-logarithmic plots of D_L versus time under variable experimental conditions: (a) surface wettability, (b) oil viscosities, (c) surface curvatures and (d) oil volumes. The error bars are not presented for clarity.

6.2.2 Non-spherical cap shape of the droplets

The shape of oil droplets associated with the dynamic contact angle was found to evolve with time during the entire oil receding process. In this section, the dynamic contact angle measurement from the recorded optical images is discussed. In this study, the body force can be safely ignored due to the microscale size of the droplets, which is supported by small Bond number (ratio of body force to capillary force) of 10^{-5} for the current system. The speed of placing the oil droplet on the spherical cap from air into the aqueous phase was ~ 0.01 m/s in the experiments, corresponding to a Weber number (ratio of inertial force to capillary force) at the initial stage in the order of 10^{-3} . In such systems, the inertial effect is negligible. As a result, “quasi-static spherical cap approximation” is often considered to be valid for the description of the receding droplet shape.

With this approximation, the dynamic contact angle can be determined via several easily measurable parameters. Assuming a constant V_o during the recession process, the direct geometric relationship between the contact angle (θ_d) and the half arc length (r) of the instantaneous droplet wetted area between the TPCLs on the side view image could be established. If the curvature of the solid surface is $1/R_m$, the relationship is given by[159]

$$\frac{\sin^3 \varphi}{\sin^3(\theta - \varphi)} [2 + 3 \cos(\theta - \varphi) - \cos^3(\theta - \varphi)] - [2 - 3 \cos \varphi + \cos^3 \varphi] = \frac{3V_o}{\pi R_m^3} \quad (6-2)$$

where the angle φ is defined to be r/R_m .

On the other hand, the convenient circle-fitting contact angle measurement approach as discussed in **Section 4.2** may be employed to determine the dynamic contact angle directly from captured images by assuming the spherical cap shape of the oil droplet. The image sequences of one displacement experiment were analyzed by the aforesaid dynamic contact angle measurement approaches of the “quasi-static spherical cap approximation”. As indicated by the square and circle symbols in **Figure 6-3**, considerably different contact angle values from two different approaches were obtained at early receding stage. This finding indicates that the “spherical cap approximation” may provide inaccurate measurement of dynamic contact angles. In fact, as shown in **Figure 6-2**, significant deviation of receding droplet shape from the spherical cap shape was observed in these experiments.

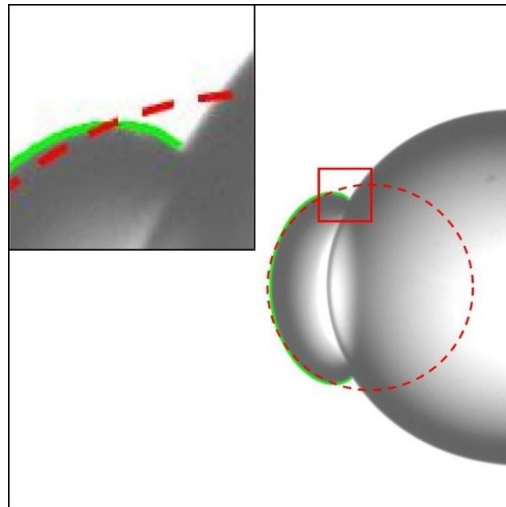


Figure 6-2: Demonstration of the deviation of the dynamic drop shape from a spherical cap on the snapshot of the oil displacement experiment. The zoomed region of the meniscus shape near the TPCL enclosed in the red square is shown in the inset.

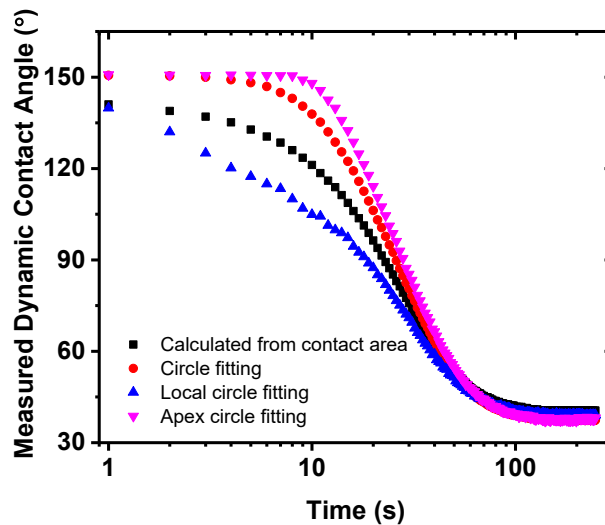


Figure 6-3: Comparison of dynamic contact angles determined using four different approaches for the same oil receding process.

When the TPCL is moving, the viscous stress could arise from the viscous flow near the TPCL. Cox[12] provided a theoretical hydrodynamic analysis by dividing the moving meniscus into three hypothetical regions where different dominant balances of forces control the shape of the fluid-fluid interface. Far away from the TPCL where viscous flow is insignificant, the surface of the droplet is well defined by the capillary force and its shape could be accurately described by the

analytical solution of a static condition (e.g., a spherical cap shape by neglecting gravity). This part of the droplet constitutes the outer region. Closer to the TPCL, the shape of the droplet is distorted by growing viscous forces from local flow field and bent towards the direction of the TPCL motion. In this viscous bending region which is also known as intermediate region, the meniscus shape governed by the balance of viscous and capillary forces may deviate significantly from the static Laplacian profile. As shown in **Figure 6-2**, the distortion of the oil droplet shape was found to be more pronounced near the moving TPCL and the location of the observed TPCL on the image to be inside the best fitted circle. Thus, the non-spherical cap shape in this study is likely to arise from the viscous effect near the TPCL, providing a direct proof that the viscous bending region hypothesized in the Cox's theory does exist. As the interface is microscopically close to the TPCL where the classical hydrodynamic theory breaks down, totally different governing mechanism is supposed to control this inner region. Currently, the specific physics of this region is not well understood, as a result of lacking direct experimental probing of the microscopic inner region. However, solid-liquid interactions (such as van der Waals, electrostatic and hydrophobic forces) have been suggested to be a crucial factor.

Based on Cox's theoretical analysis, a model has been developed to appropriately capture the dynamic meniscus shape of immersing a glass tube into a liquid bath.[160] The details of this model could be found elsewhere.[160] [161] From the description of this model, the deviation of the dynamic interface shape from the static shape due to the viscous force is more significant for the interface close to the TPCL. Such deviation is considered to depend on Ca defined in **Section 2.3.1**. The deviation at a given distance to the TPCL could become more significant with increasing Ca . Due to the complex temporal and spatial variation of the Ca during the spontaneous droplet receding, accurate quantification of the receding droplet shape with this model is proven to be difficult. However, it is still plausible that more significant viscous effect on the interface could be observed at higher Ca during the dynamic receding process.

In most scenarios of the spontaneous spreading/receding of sessile droplets, the initial maximum Ca value at the TPCL is typically around $10^{-4} \sim 10^{-2}$. [43] [51] [47] [162] Even larger Ca value could be found in some cases but only for the forced wetting.[59] In this spontaneous droplet receding system, the typical maximum magnitude of Ca could be as large as 0.1. A non-negligible viscous contribution to the interface at the minimal length scale limited by the capability of the experimental set-up resolution ($\sim 1 \mu\text{m}$), may emerge. On the other hand, it is likely that the smaller

microscale size oil droplet used in this study could result in larger relative surface area on the droplet under the influence of the considerable viscous force. Thus, the prominent viscous force indicated by large Ca value may distort the shape of static-like interface significantly near the TPCL, leading to significant deviation of the droplet shape from the spherical cap shape.

To quantitatively investigate the extent of dynamic shape deviating from a spherical cap, the image analysis on the shape of the droplets was performed and a deviation factor (ε) as a measure of the deviation was defined as follows,

$$\varepsilon = \frac{\sum_{i=1}^n [\sqrt{(x_i - x_c)^2 + (y_i - y_c)^2} - R_c]}{n_{pixel} L_c} \times 100\% \quad (6-3)$$

where (x_i, y_i) and (x_c, y_c) denote the coordinates of all the edge pixels on the oil-water interface and the center of the corresponding best fitting circle, respectively. R_c is the radius of the best fitting circle. n_{pixel} in **Equation (6-3)** represents the total number of edge pixels and the characteristic length L_c could be considered as the radius of oil droplet when it forms a spherical shape.

The temporal evolution of ε is given in **Figure 6-4**. In general, the original spherical cap shape of oil droplet in air could deform immediately at the initial receding stage upon in contact with an immiscible liquid. The deviation factor increases rather rapidly to a maximum value (ε_{max}) and then diminishes progressively to the minimum equilibrium value. It should be noted that ε can never be zero due to the pixel noise originating from the edge detection and the finite resolution of imaging analysis. In this study, the oil droplet could be regarded as a perfect spherical cap shape when ε is around 0.2%.

On the surfaces of different wettabilities, the significant variation of ε_{max} in each case was detected (**Figure 6-4a**). Since adjusting the surface wettability could achieve considerably variable Ca by varying U without changing μ and γ , such experimental observation further verifies that the extent of the droplet deformation is strongly correlated to Ca . On each corresponding surface, the receding oil droplet configuration at ε_{max} is given by the snapshot in **Figure 6-5**. As shown in **Figure 6-5a**, the deviation of the droplets from the spherical cap shape on the most hydrophilic surface could be easily recognized. As the hydrophobicity of the solid substrate is increased, ε_{max} becomes smaller and the droplet deformation at ε_{max} is less significant. As shown in **Figure 6-5e**,

non-spherical cap shape of receding oil over the most hydrophobic surface is almost absent on the captured image.

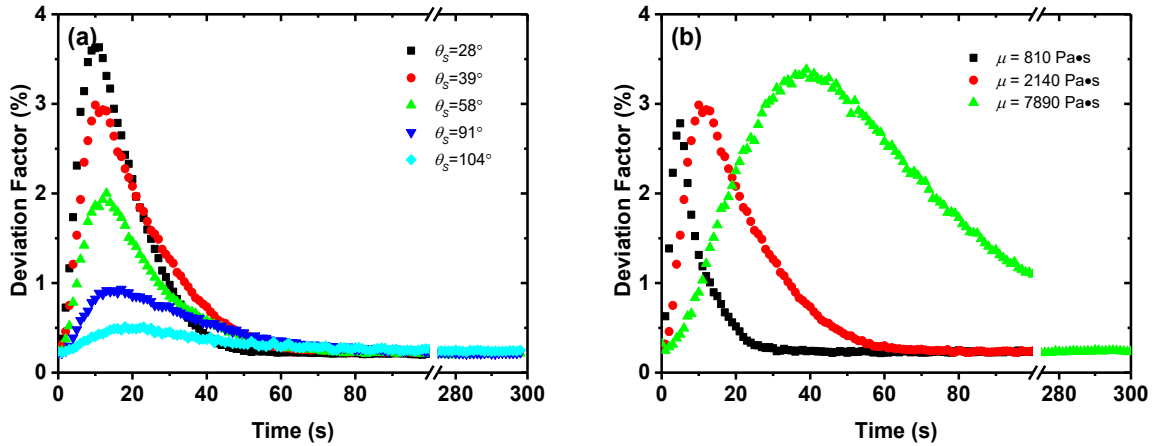


Figure 6-4: Deviation factor as a function of displacement time with various (a) surface wettability and (b) oil viscosities.

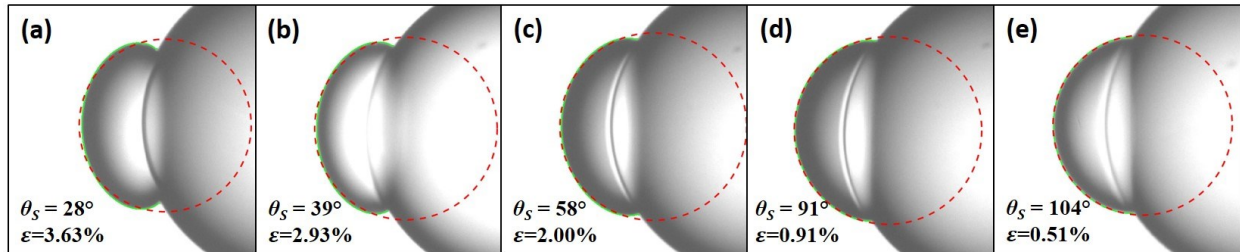


Figure 6-5: Snapshots of receding oil droplet configurations at the time with maximum deviation factor on a set of surface with variable wettability, showing progressive less deviation of the oil droplets on increasingly high hydrophobicity of solid surfaces: (a) $\theta_s=28^\circ$; (b) $\theta_s=39^\circ$; (c) $\theta_s=58^\circ$; (d) $\theta_s=91^\circ$ and (e) $\theta_s=104^\circ$.

In contrast to the alteration of the surface wettability, **Figure 6-4b** reveals insignificant influence of the oil viscosity on ϵ_{\max} , decreasing ϵ_{\max} only slightly with lowering the viscosity of the oil in the studied range. Reducing μ is known to increase U and alter Ca , which is believed to be a key factor that causes the deviation of the droplet from the spherical cap shape. Moreover, the recession of the low viscosity oil droplet occurs more rapidly to allow a narrow window of investigating temporal droplet shape. It should be noted that all the oils used in this study fell into the high viscosity range. Based on the tendency of μ variation obtained here, it may be predicted that ϵ_{\max}

could become smaller and significant deviation could occur only at an early stage in a narrow temporal window when viscosity is further decreased. This consideration could provide an explanation why the non-spherical cap droplet shape caused by viscous flow has not been observed in most studies involving low viscosity fluids.

6.2.3 Dynamic contact angle

Intuitively, it is straightforward to extract the local meniscus shape for the contact angle determination. In this study, a local circle fitting method mentioned in **Section 4.2** was used. The number ratio of contour pixels selected for fitting with respect to the overall contour pixels of the oil-water interface was defined as the edge pixel ratio. Interestingly, for significantly deformed droplets (**Figure 6-6a**), a pronounced discrepancy of local fitting circles has been found when different edge pixel ratios which could be regarded as various observation scales were selected for fitting. Meanwhile, the results in **Table 6-2** revealed that fewer edge pixels employed for such local fitting method could yield smaller dynamic contact angle values, which means that the curvature of the interface profile near the TPCL becomes increasingly larger as the observation gradually approach the TPCL. This observation further demonstrates that the viscous force could be the main factor of the droplet deformation in this study, as the viscosity-induced bending of the interface near the TPCL could result in the scale dependence of the local dynamic contact angle. As the droplet deformation became negligible at the scale of the observation, the discrepancy of best fitted circles with different edge pixel ratios diminished (**Figure 6-6b**) and consistent local contact angles were obtained (**Table 6-2**).

Table 6-2: Contact angles obtained using the local circle fitting methods with various pixel ratios for fitting

Pixel ratios for fitting	5%	10%	15%	20%
(a) $\varepsilon=2.93\%$	102°	110°	116°	121°
(b) $\varepsilon=0.24\%$	39°	38°	37°	37°

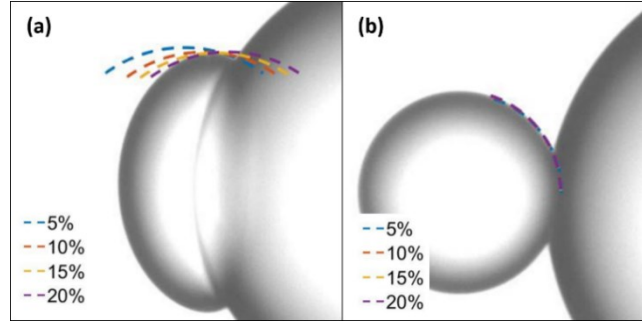


Figure 6-6: Best local fit of circles with various pixel ratios in fitting of local oil droplets for the ε values of the droplets to be (a) 2.93% and (b) 0.24%.

The extensive drop shape analysis of the local meniscus has led to a generally-accepted view that the dynamic contact angle may not be a well-defined concept and the actual dynamic contact angle at the immediate vicinity of the TPCL is different from the experimentally measured macroscopic contact angle values. [30] [58] [160] Practically, the accessibility of the experimental observation, such as finite resolution of experimental set-up, allows us to extract the experimental dynamic contact angle at a specific length scale. In most cases, due to small Ca , the experimental observation can only reach the quasi-static interface which is negligibly affected by viscous force. For this reason, the complexity caused by viscous bending of the droplets near the TPCL could be easily avoided during the practical operation.

As the interface near the TPCL becomes more curved beyond the circular description, more sophisticated ellipse[163] and polynomial[118] [128] fitting methods were performed in some investigations to obtain more accurate meniscus shape for contact angle measurement. However, to my knowledge, these measurements are essentially phenomenological, and the fundamental physics of the more curved surface is still beyond the consideration of these methods. In this study, the simple circular geometry for contact angle measurement was still adopted. To achieve more local information with finite image resolution, only 5% edge pixels were selected in the following discussion. Smaller edge pixel ratio was not implemented, since the noise on the captured image could cause pronounced uncertainty of the results from circle fitting. The contact angle determined in such way is called “local dynamic contact angle” in this study.

To eliminate the impact of the viscous bending on the dynamic contact angle determination, the alternative apex circle fitting discussed in **Section 4.2** was also conducted and the quasi-static apex part of the droplet far away from the TPCL was used in this method. From the apex to the TPCL,

the circle achieved by the apex fitting could fit a wide range of the droplet contour until it deviates. Thus, it is indicated that this method may, to a large extent, get rid of the scale sensitivity of the measured dynamic contact angle caused by the viscous bending. The measured contact angle by this method is called “extrapolated dynamic contact angle”.

Comparing the results of dynamic contact angle obtained by all the methods mentioned above for the same image sequences (**Figure 6-3**), considerable difference at the initial oil receding stage suggests that these methods could not be treated identically. However, the consistent contact angle values at the later stage with slow TPCL movement illustrate that the discrepancy of these methods diminishes when the droplet deformation is not serious. This investigation hints that these methods are supposed to be interchangeable for the common dynamic wetting systems with a low Ca value. A close look at more significant scatter in the data obtained by local circle fitting method reveals such method has a relatively low resistance to the uncertainty of edge pixels on the image.

6.2.4 Quantitative description with theoretical models

In this section, the MK and HD models that were established to quantify wetting dynamics were examined to evaluate their applicability to predicting the experimental dynamics of TPCL displacements in this study. The respective adjustable parameters related to microscopic properties obtained by the least-square fitting will be discussed.

With using the contact angle of the oil phase ($\pi - \theta_d$), the MK model (**Equation (2-14)**) and the HD model (**Equation (2-4)**) were rewritten into **Equation (6-4)** and **Equation (6-5)** here respectively:

$$U = 2K_0\lambda \sinh\left(\frac{\gamma[\cos(\pi - \theta_{d,M}) - \cos(\pi - \theta_S)]\lambda^2}{2k_B T}\right) \quad (6-4)$$

$$g\left(\pi - \theta_{d,H}, \frac{\mu_1}{\mu_2}\right) - g\left(\pi - \theta_m, \frac{\mu_1}{\mu_2}\right) = \pm C a \ln\left(\frac{L}{L_S}\right) \quad (6-5)$$

The experimentally obtained dynamic contact angles could be considered to be the non-static contact angle in the MK model and macroscopic contact angle in the HD model. With these considerations, extracting their values from the experiments is an essential step to perform a quantitative investigation with these models. In most cases, the non-static contact angle and the macroscopic contact angle could be safely treated as identical concepts for model implementations. However, for these systems, different experimentally obtained dynamic contact angles for each

model need to be used due to significant interfacial viscous bending near the TPCL. For the MK model, the local shape of the meniscus at the TPCL could more accurately predict the unbalanced Young's force which alters the thermal activated behavior of molecules at the TPCL zone. Therefore, more local dynamic contact angle extracted from the local circle fitting method needs to be used as the non-static contact angle in this model. The macroscopic contact angle in the HD model on the other hand should be extrapolated from the static interface with a negligible viscous effect. In this case, the dynamic contact angle extrapolated using the apex circle fitting method is used as the macroscopic contact angle in the HD model.

Cosine functions of local dynamic contact angles are plotted against TPCL speed in **Figure 6-7**. The MK model is applied to fitting these experimental data with the theoretical curve. The theoretical curve from the MK model agrees fairly well with the experimental data of oil receding over low velocity range. However, as the TPCL speed increases, the MK model consistently underestimates the cosine function of local dynamic contact angles. In other words, the collected experimental dynamic contact angle values at high TPCL velocity are likely to yield stronger unbalanced Young's force as compared with the model prediction. Previous research[164] pointed out that the transition of dominant energy dissipation mechanism from the immediate vicinity of the TPCL to the viscous flow in the core region of the droplet at increasing TPCL velocity could cause such deviation of the MK model, since the dissipation from the hydrodynamic viscous flow is not considered in the MK model. Here it is skeptical that the scale sensitivity of local dynamic contact angle discussed earlier could be an alternative explanation. At high displacement velocity of viscous liquid, a considerable viscous bending may cause unreliable measurement of local contact angle values through the present procedure. As mentioned earlier, reducing observation scale in such case could yield smaller local contact angle values. The correction of such experimental uncertainties could decrease the experimental value of cosine function in **Figure 6-7** to obtain a better prediction over the high velocity region. Such speculation lacks adequate evidence to confirm and further investigation with higher resolution experimental facilities is needed.

A close look at the dynamic regime which is governed by the MK model reveals that the correlation between dynamic contact angle and TPCL velocity is strongly affected by surface wettability and liquid viscosity, while it remains almost unchanged at various surface curvatures and droplet sizes as anticipated. The adjustable parameters extracted from the best fit of the MK model to the

experimental results at low velocity regime are given in **Table 6-3**. In general, λ and K_0 tend to be randomly distributed and have no particular dependence on variable parameters in this study, whereas the contact line friction (ζ) shows increasing ζ value with increasing surface hydrophobicity or oil viscosity. Again, the surface curvature and oil volume have insignificant impact on the contact line friction.

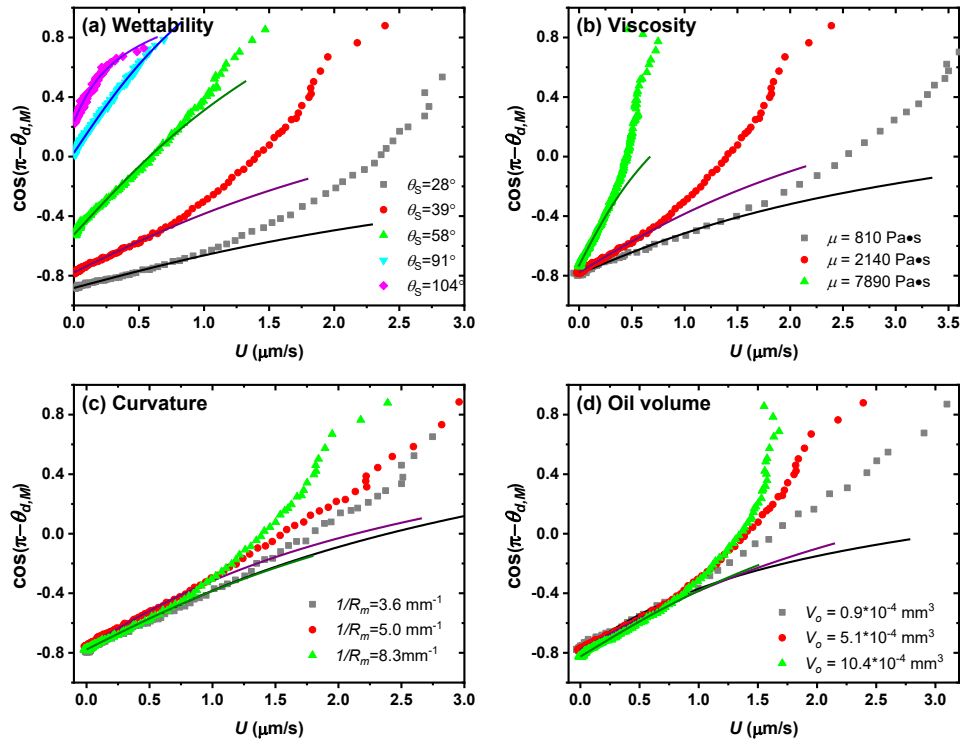


Figure 6-7: Cosine functions of local dynamic contact angles as a function of the TPCL speed at various surface (a) wettability, (b) oil viscosities, (c) surface curvatures and (d) oil volumes: symbols for the experimental results and solid lines from the MK model for comparison.

In this high viscosity dynamic systems, the values of λ always fall within the typical length scale of molecular size, whereas the values of K_0 are quite small only in a few hundred hertz as compared with the order of megahertz reported in previous studies. Such abnormal K_0 values could be explained by the modified MK theory proposed by Blake.[45] The small K_0 observed in this study is a result of extremely high viscosity of oil as shown in **Equation (2-18)**. **Equation (2-19)** predicts a linear increase of the contact line friction parameter with liquid viscosity but an exponential increase with the adhesion energy. Provided that λ and V_L/λ^3 do not change substantially as the

case in this study, the linear correlation between the contact line friction and liquid viscosity is substantiated by the data from the viscosity study in **Figure 6-8a**. It appears that the plot of $\ln(\xi/\mu)$ against W_a obtained from wettability study yields a straight line in **Figure 6-8b**, which suggests that ξ will increase exponentially with W_a . It should be acknowledged that the linear fit in **Figure 6-8b** is less convincing due to some scatter, which is attributed to the nature of **Equation (2-19)** to be a rough estimation. Consideration of the pinning energy arising from the contact angle hysteresis[164] [165] might be needed to improve the fit. Unfortunately measuring the receding contact angle of water in the current experimental setup is not possible and there is a clear need to design a new experimental setup that allows the addition of the oil droplet into the solid surface in the aqueous environment for the receding displacement of three phase contact angle at the microscale experiments. Furthermore, the values of λ and V_L extracted from the best fitted straight line in **Figure 6-8b** are 0.41nm and 0.35nm³, respectively. The V_L value obtained here is close to the volume of some small molecules, [47] [50] [166]which implies that only a molecular segment of the macromolecular oil is likely to be displaced on the adsorption sites in one individual thermally activated motion.

Table 6-3: Adjustable parameters extracted from MK and HD models

	λ (nm)	K_0 (kHz)	ξ (kPa*s)	$\ln(L/L_s)$ (small U)	θ_m (°) (small U)	$\ln(L/L_s)$ (intermediate U)	θ_m (°) (intermediate U)
Wettability: 28°	1.1±0.2	0.4±0.4	10±2	33±3	27±2	17±1	34±1
Wettability: 39°	0.64±0.02	0.9±0.2	17±2	34±6	38±3	16±1	47±4
Wettability: 58°	0.52±0.03	0.9±0.1	34±1	33±1	58±2	13±1	68±2
Wettability: 91°	0.6±0.1	0.4±0.2	48±3	20±2	91±1	10±2	97±1
Wettability: 104°	0.9±0.2	0.1±0.1	62±9	18±1	102±4	-	-
Viscosity: 810 Pa*s	0.8±0.1	1.0±0.4	7±3	63±8	36±2	19.8±0.4	50±1
Viscosity: 2140 Pa*s	0.64±0.02	0.9±0.2	17±2	34±6	38±3	16±1	47±3
Viscosity: 7890 Pa*s	0.63±0.03	0.3±0.1	47±1	22±2	41±3	12±1	51±5
Curvature: 3.6 mm⁻¹	0.7±0.1	1.0±0.2	16±1	36±5	36±3	16±1	45±2
Curvature: 5.0 mm⁻¹	0.6±0.1	1.0±0.3	18±1	35±3	39±2	14.0±0.4	50±4
Curvature: 8.3 mm⁻¹	0.64±0.02	0.9±0.2	17±2	34±6	38±3	16±1	47±3
Volume: 0.9×10⁻⁴ mm³	0.7±0.1	0.7±0.3	18±2	34±3	36±2	14±2	47±1
Volume: 5.1×10⁻⁴ mm³	0.64±0.02	0.9±0.2	17±2	34±6	38±3	16±1	47±3
Volume: 10.4×10⁻⁴ mm³	0.7±0.1	0.8±0.5	17±1	44±3	34±4	18±2	43±4

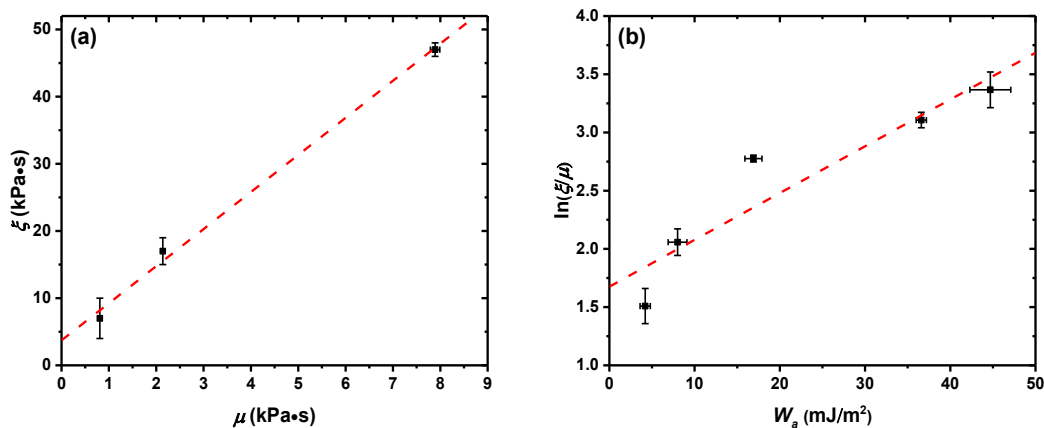


Figure 6-8: (a) Plot of ζ versus μ of oil based on the results of viscosity study and (b) plot of $\ln(\zeta/\mu)$ versus W_a obtained from wettability study, both showing anticipated relationship predicted by Blake's theory.

To evaluate the validity of the HD model, g functions of the extrapolated dynamic contact angles were plotted against the respective TPCL displacement speed. As shown by the solid line in **Figure 6-9**, two linear correlations between the g function and the TPCL velocity in the same oil receding process were found for the low and intermediate TPCL displacement velocity regimes. Such finding implies that the HD model could predict the experimental results reasonably well in these two regions. The interesting behavior associated with two HD model fitting regions for the same recession process has also been reported by Hua et al.[48] in a study on the ionic liquid retraction dynamics after removing applied electrical field. In comparison to their result, the HD fitting in this study failed to capture the data points at the high displacement velocity region, which could be attributed to the considerable unsteady flow at the corresponding early stage of drop displacement. More details regarding this region will be discussed later. Based on the length scale of this system and typical molecular size length scale of microscopic cutoff length, $\ln(L/L_s)$ is expected to be around 10. As indicated in **Table 6-3**, the values of $\ln(L/L_s)$ extracted from the slopes of the straight lines at the intermediate velocity range are closer to the expected values. This agreement implies that HD model may provide more reasonable physical description of oil receding over the intermediate TPCL velocity range. $\ln(L/L_s)$ is related to the viscous resistance at the moving TPCL. Contrast to the contact line friction in MK model, the $\ln(L/L_s)$ values extracted from intermediate velocity range decrease with increasing surface hydrophobicity or oil viscosity.

In addition, the $\ln(L/L_s)$ value is illustrated to increase with oil volume as the consequence of increasing macroscopic length scale. θ_m extracted from the intermediate velocity range was found to be systematically larger than the static contact angle.

It is noted that the HD model is incapable of predicting the oil receding behavior at early receding stage. In fact, the HD model is based on Cox's asymptotic expansion of hydrodynamic analysis for a steady meniscus shape near the moving TPCL. In reality, the spontaneous oil receding in this investigation is inherently unsteady. Yue et al.[167] suggested that an unsteady stress could arise from the temporal evolution of the contact angle. The experimental observation may deviate significantly from the steady state model if the condition that the unsteady stress is much smaller than the viscous stress at steady state is not satisfied. When the oil just starts to recede over the solid surface, the fast evolution of the contact angle caused by the sudden change in velocity of the TPCL could lead to a significant unsteady stress. The prevailing unsteady nature could be also implied by the negligible temporal evolution of the extrapolated dynamic contact angle in the initial stage as shown in **Figure 6-3**. Such unsteady stress arises from the delayed response of the interface shape at the apex to the sudden viscous flow generated near the TPCL. Due to prevailing unsteady nature, the classic dependence of the TPCL velocity on dynamic contact angle may be insufficient to predict the behavior of moving TPCLs. It appears that the dependence of the TPCL speed could be more complicated at this initial stage: both the local meniscus shape and nonlocal flow field near the TPCL should be involved. This observation could imply two intrinsically distinct types of common dynamic wetting phenomena, including the forced wetting with constant velocity and the spontaneous wetting with continuously changed velocity, which are usually believed to be identical in the theoretical description.[37] [39]

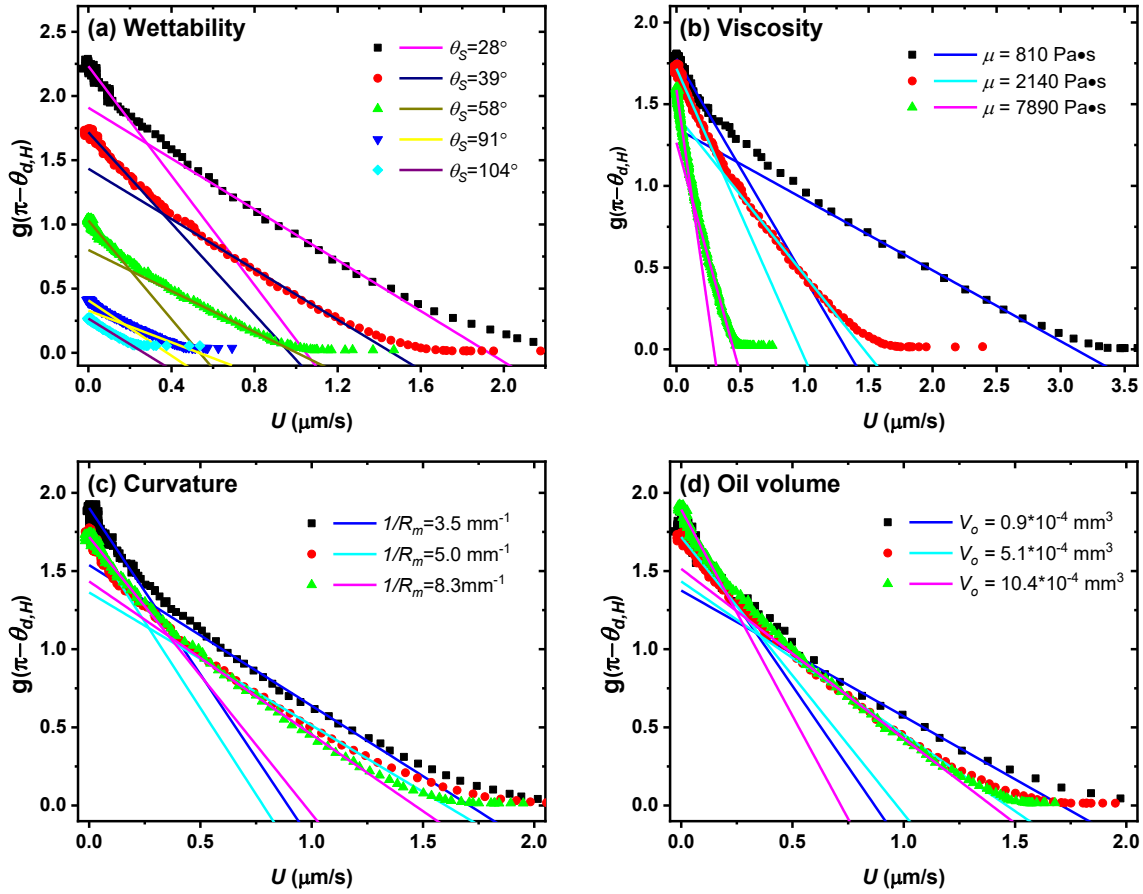


Figure 6-9: g function of extrapolated dynamic contact angles as a function of the TPCL speed at various surface (a) wettability, (b) oil viscosities, (c) surface curvatures and (d) oil volumes: symbols representing experimental results and lines the prediction by the HD model for comparison. The straight line represents the best fitting using the least square method on the data points over the velocity region where the data appeared visually linear.

Based on the previous discussions of the droplet shape deviation, three distinct stages could be summarized in a single oil displacement process. At the early stage with the significant variation in the deviation factor ε , the considerable unsteady stress caused by the fast contact angle relaxation could result in the dynamic behaviors beyond the consideration of either HD or MK wetting dynamic models. Over time, ε becomes stable but the deformation of the oil droplet remains pronounced. In this case, the HD model could provide reasonable prediction of oil receding dynamics. At the later stage when the oil droplet is close to the spherical cap shape which is characterized by small ε , the MK model could describe the dynamic behaviors well. Since the

intensity of the hydrodynamic viscous flow could be directly inferred from the extent of the droplet deformation, the applicable range of these two conventional models in this study is consistent with the prominent energy dissipation mechanisms considered in corresponding models. For the HD model the energy dissipation comes from the viscous flow in the bulk whereas for the MK model the energy dissipation originates from the TPCL.

6.3 Summary

The microscopic spontaneous displacement of high viscosity oil by aqueous media on curved surface was studied experimentally using an optical method. The experimental results revealed that a faster oil displacement and higher ultimate D_L could be observed on hydrophilic surfaces. The increase in oil viscosity, surface curvature or droplet volume has been shown to have an adverse effect on oil displacement dynamics but no considerable impact on the ultimate D_L .

The microscale experiment using high viscosity oil on a solid microsphere cap in water revealed a dynamic droplet with non-spherical cap shape, which is inconsistent with the thermodynamic consideration. This behavior is believed to arise from the relative significance of the viscous stress to the capillary stress on the interface near the TPCL. Such observation provides a direct experimental evidence of the viscosity-dominated intermediate region hypothesized in the Cox's hydrodynamic description of a moving meniscus. The results of the image analysis suggest that the extent of the droplet deformation from the spherical cap shape is strongly correlated to Ca . Due to the non-spherical cap shape, the dynamic contact angle evaluation by the "quasi-static spherical cap approximation" has been demonstrated to result in considerable errors. Further image analysis revealed that the dynamic contact angle is a rather complex concept, since the dynamic contact angle extracted experimentally from the local meniscus shape may exhibit a strong dependence on the scale of observation. Such finding led to developing new techniques to extract the experimental dynamic contact angle.

To perform the quantitative analysis of the dynamic contact angle-velocity dependence described in the MK and HD models, dynamic contact angles obtained using the image-based local and apex circle fitting methods were used in the respective approaches. The MK model was shown to produce a reasonable agreement with the dynamics of oil receding when the oil droplet shape is slightly deformed, whereas the oil receding behavior could be described only by the HD model as

the droplet deformation becomes more significant. The results collectively indicate that the applicability of these models relies on the dominant energy dissipation mechanism, a conclusion in line with those reported in previous studies.[57] [164] [168] The dynamic behavior at the initial stage was not predicted by the conventional models, which was attributed to the highly unsteady nature of these spontaneous wetting systems. The consideration of unsteadiness could potentially distinguish the dynamics of the spontaneous wetting from that of the forced wetting imbedded in the theoretical description.

Chapter 7

Oil displacement in surfactant aqueous solutions

7.1 Introduction

In numerous practical applications, chemical additives, especially surface-active agents (surfactants), are added into one fluid to modify the interfacial properties and control the displacement behavior. Thus, understanding displacement behavior in the presence of surfactant is essential for many industrial processes. Even though many recent investigations discussed in **Section 2.5** provided great insights into the influence of surfactants on fluid-fluid-solid systems from a thermodynamic point of view, they are inadequate to improve the understanding under dynamic conditions.

Up to date, most studies on the dynamics of wetting systems involving surfactants were concerned with aqueous solutions spreading over a flat solid surface in air.[103] [169] Despite these thorough investigations on spreading droplets, studies have rarely addressed the influence of surfactants on the dynamics of a receding droplet. For cleaning applications, the TPCL motion of an oil droplet displaced by aqueous solutions over a solid surface is considered one of the important mechanisms of the removal of oily contaminants from a surface.[170] This mechanism is frequently called “rollup”. Kolev et al. investigated the spontaneous oil drop detachment from a glass surface in anionic surfactant solutions.[171] Using a model that accounts for the line drag force to characterize the dynamic behavior of the oil displacement, they claimed that the behavior was mainly related to interfacial properties, but buoyancy was responsible for the ultimate detachment.

Aiming to have a more comprehensive understanding of the oil droplet receding process in surfactant solutions as well as get a better understanding on the effect of the released natural surfactant on the bitumen liberation, in this chapter, spontaneous displacements of high viscosity micrometer-sized oil droplets from curved glass substrates in aqueous surfactant solutions is experimentally examined and discussed. This study expanded the work of the same process in pure water solutions discussed in the previous chapter. Conventional anionic, cationic and nonionic

surfactant solutions in a wide range of concentrations were used for a systematic investigation. The high viscosity oil phase could inhibit oil emulsification in surfactant solutions.[172] The density of the oil was close to the aqueous solution and hence, in conjunction with the micrometer size of the oil droplet, the buoyancy effect could be neglected. The properties of the oil-water and water-solid interfaces, which are closely related to the oil displacement behavior, were investigated independently prior to the displacement experiments. Experimental observations of the oil displacement were analyzed and discussed to understand the contributing role of surfactants. Two types of quantitative analysis were performed to explore the dynamic behavior of oil displacement.

7.2 Results and discussions

7.2.1 Interfacial tension between oil and water

The surfactant-induced changes to the oil-water interfacial properties were directly reflected by the measured oil-water interfacial tension (γ_{ow}). The oil-water interfacial tensions in the presence of SDBS, CTAB, and TX-100 versus the surfactant concentrations are presented in **Figure 7-1**. As the concentration was increased, all the surfactants exhibited similar efficiency in lowering γ_{ow} . In addition, the CMC was a crucial shift point: γ_{ow} drastically diminished with an increase of surfactant concentration until the CMC, whereas the further increase of surfactant concentration beyond the CMC had a slight impact on γ_{ow} . Over the entire range of the surfactant concentration, the interfacial tension was always larger than 1mN/m. Thus, spontaneous emulsification regarded as another important mechanism for the removal of oily dirt in surfactant aqueous solutions was unlikely to occur here.[173] [174]

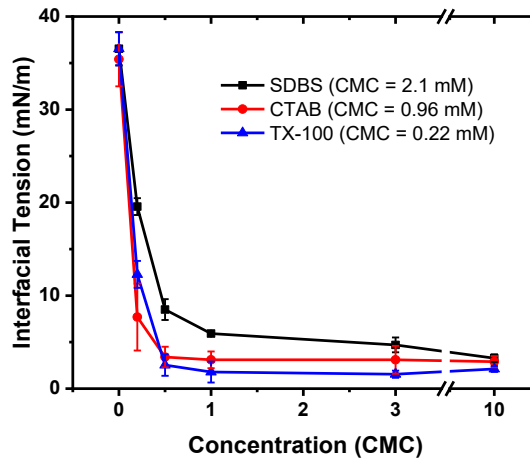


Figure 7-1: Interfacial tensions between high viscosity oil N190000 and surfactant aqueous solutions at different surfactant concentrations

7.2.2 Adsorption of surfactants at the solid-water interface

The influence of surfactants on the solid-water interfacial properties was characterized by adsorbed surfactant densities determined by the QCM-D technique. The typical raw QCM-D data of frequency and dissipation shifts at third overtone are shown in **Figure 7-2**. It was found that all the presented data satisfy the criterion of $\Delta D_n / (-\Delta f_n / n) \ll 4 \times 10^{-7} \text{ Hz}^{-1}$, thus the adsorbed surfactant molecules could be assumed to be a rigid layer on the surface.[175] With the assumption, **Equation (3-1)** can be applied to evaluate the surfactant adsorption density on the silica surface. The results of the corresponding evaluation of the adsorbed densities are given in **Table 7-1**. It is seen that these surfactants exhibit totally different adsorption behavior on the silica surface: a considerable amount of cationic CTAB molecules could preferably adsorb on the surface whereas few anionic SDBS molecules could deposit on it. Also, a sharp increase of the adsorption density from the low to the high concentration could be observed in the TX-100 solution.

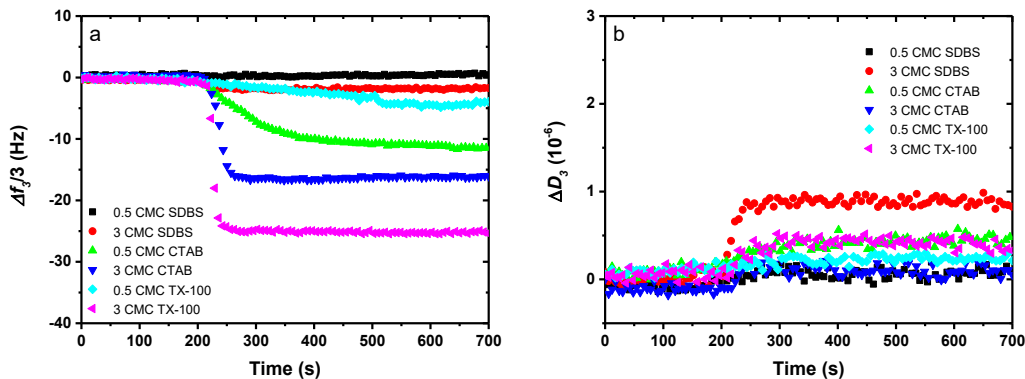


Figure 7-2: Monitored (a) frequency and (b) dissipation shifts of the QCM-D silica sensor at the third overtone caused by surfactant adsorption.

Table 7-1: Ultimate adsorbed surfactant densities (nmol/cm^2) on the silica sensor

Concentration	SDBS	CTAB	TX-100
0.5	-	0.52 ± 0.08	0.13 ± 0.06
3	0.09 ± 0.03	0.78 ± 0.05	0.7 ± 0.1

In fact, the adsorption process at the liquid-solid surface was shown to be driven by the interactions between surfactant molecules and the solid surface.[72] In this regard, apart from the adsorption caused by chemical reaction, several intermolecular forces, including electrostatic interactions, hydrophobic bonding, hydrogen bonding, and dispersion forces, are believed to be involved in the interaction during the adsorption.

The significant difference between anionic and cationic surfactant adsorption densities presented in **Table 7-1** should be mainly attributed to electrostatic interaction. The silica surface is negatively charged in the aqueous medium at a natural pH environment, so could lead to a strong attraction of cationic CTAB and repulsion of anionic SDBS. The slight adsorbed amount detected at high concentration of SDBS solution may be attributed to the extremely weak attractive force between siloxane groups on the silica and tails of SDBS molecules.[176] [177]

The hydrogen bonding between hydroxyl groups on the solid surface and polar ethylene oxide groups of individual surfactant molecule plays an important role in the adsorption of the nonionic surfactant TX-100 on the silica surface.[178] Compared to the electrostatic interaction, the

hydrogen bonding is much weaker, in that the low adsorption density was observed in the low concentration solution of TX-100. However, as the concentration was increased, a sharp increase of surfactant adsorption could emerge due to the formation of a complex structure via hydrophobic chain-chain interaction or direct adsorption of surfactant micelles.[179] [180] It is mentioned that the direct micellar adsorption to the surface was more likely to occur when the strength of the attraction between the headgroup of the surfactant and the surface is weak.[181] This could result in considerable enhancement of adsorption density from low to high concentration solutions of TX-100.

To sum up, the adsorption density of different surfactant at the solid-water interface displayed various features and hence led to a noticeable difference of solid surface energy alternation. Except for the adsorption amount, the orientation of adsorbed surfactant molecules on the surface could be another important factor affecting the alternation caused by the surfactant adsorption. More details will be discussed later.

7.2.3 Experimental result of oil displacement

Figure 7-3 depicts the temporal evolution of r_c normalized by its initial value (r_{c0}) in the course of the oil displacement in different aqueous solutions. It should be mentioned that the symbol r_c , which represents the radius of the wetted area on a flat surface, also denotes the half arc length of the wetted area in this study. The case of 0 CMC represents pure water solution without surfactant addition. It is seen that different surfactant solutions lead to diverse oil displacement behavior. In high concentration of SDBS solutions, spontaneous detachment of the oil from the glass surface could eventually occur at a certain moment. Such spontaneous detachment is indicated by the sudden disappearance of the r_c/r_{c0} evolution data in the time range of 10 s to 100 s as shown in **Figure 7-3a**. **Figure 7-3b** revealed that oil displacement barely occurred in CTAB solutions, as r_c/r_{c0} maintained its value close to 1 over time. The values of r_c/r_{c0} observed at the end of the experiments suggest that SDBS could promote the final configuration of oil displacement whereas CTAB and TX-100 could hinder it. However, from the dynamic perspective, all the surfactants, at any concentration, reduced the speed of the displacement process, since a slower decrease of r_c/r_{c0} with time was observed in the presence of surfactants.

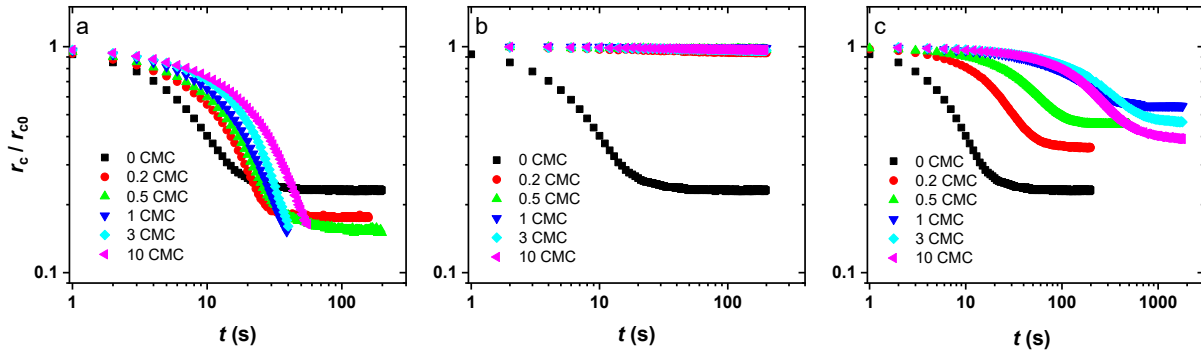


Figure 7-3: Temporal evolution of r_c/r_{c0} during oil displacement in (a) SDBS, (b) CTAB and (c) TX-100 solutions.

In what follows, our discussion is divided into static and dynamic sections to explore the effect of surfactants on the oil displacement behavior. For the dynamic behavior, we focus on the case of SDBS and TX-100, as no obvious dynamics was observed in CTAB solutions. The quantitative analyses of the temporal evolution behavior and the dependence of U on θ_d are performed to investigate the dynamics.

7.2.4 Final static contact angle

The effect of surfactants on the final status of the oil displacement can be characterized by comparing the static contact angles (θ_s) of the advancing aqueous phase, which were measured at the end of the experiments (where γ_{os} and γ_{sw} are the surface energy at the solid-oil and solid-water interfaces, respectively. Since the value of γ_{ow} is not sensitive to the surfactant type at the same concentration level of CMC, the substantial difference of θ_s could be mainly attributed to the modified surface energy (i.e., γ_{sw} or γ_{os}) caused by the different adsorption density on the solid surface as stated above.

Table 7-2). Depending on the surfactant type, the values of θ_s versus concentration displayed different tendencies. Here, the slight difference between θ_s in the experimental measurement and the equilibrium contact angle due to the hysteresis could be ignored for the prediction of the trend of θ_s at various experimental conditions. As a result, Young's equation was applicable to interpret the role of surfactant addition on the static behavior,

$$\cos(\pi - \theta_s) = \frac{\gamma_{sw} - \gamma_{os}}{\gamma_{ow}} \quad (7-1)$$

where γ_{os} and γ_{sw} are the surface energy at the solid-oil and solid-water interfaces, respectively. Since the value of γ_{ow} is not sensitive to the surfactant type at the same concentration level of CMC, the substantial difference of θ_s could be mainly attributed to the modified surface energy (i.e., γ_{sw} or γ_{os}) caused by the different adsorption density on the solid surface as stated above.

Table 7-2: Values of θ_s (deg) in SDBS, CTAB and TX-100 solutions at different concentrations

Concentration (CMC)	0	0.2	0.5	1	3	10
SDBS	30±2	24±1	21±2	-	-	-
CTAB	30±2	150±1	150±2	151±3	150±2	151±1
TX-100	30±2	56±1	66±5	89±4	65±5	58±3

In where γ_{os} and γ_{sw} are the surface energy at the solid-oil and solid-water interfaces, respectively. Since the value of γ_{ow} is not sensitive to the surfactant type at the same concentration level of CMC, the substantial difference of θ_s could be mainly attributed to the modified surface energy (i.e., γ_{sw} or γ_{os}) caused by the different adsorption density on the solid surface as stated above.

Table 7-2, it is shown that increasing the SDBS concentration could result in smaller θ_s . At the concentration beyond the CMC, θ_s was not defined due to the complete detachment of the oil from the glass surface. In such a case, θ_s could be regarded as a rather small contact angle (e.g., zero contact angle). In accordance with **Equation (7-1)**, the decreased θ_s in the presence of SDBS could be mainly attributed to the lower γ_{ow} as there was negligible adsorption of SDBS on the glass surface.

As mentioned earlier, significant surfactant adsorption on the solid could take place even at the low concentration of CTAB due to the stronger electrostatic interaction between the hydrophilic head group and the glass surface. The adsorbed CTAB molecules with hydrophobic tail group

oriented towards the aqueous phase could considerably enhance the hydrophobicity of the surface. As a result, θ_s exhibited rather large values in CTAB solutions.

For TX-100 solutions, a maximum θ_s appeared at the concentration of 1 CMC. The increase of θ_s over the low concentration range, which was less significant than that in CTAB solution, was attributed to the adsorption of TX-100 molecules on the solid surface via the weaker hydrogen bonding. With the further increase of the concentration of TX-100, the adsorption of surfactant molecules could occur via the chain-chain interaction between hydrophobic tails of adsorbed and free surfactants. The new adsorbed surfactant molecules could have a predominant orientation with hydrophilic part towards water and hence decrease θ_s at high concentrated solution due to the formation of a bilayer structure.[182] [80] In the literature[183] [177] [78], the appearance of a maximum contact angle of cationic surfactant solutions on silica surfaces as a function of surfactant concentration has also been attributed to the bilayer structure formation. However, it is interesting that the decrease of θ_s was not observed in high concentration solutions of CTAB in our study. According to Eq. **Equation (7-1)**, the slightly decreased γ_{sw} arising from the bilayer formation to lower θ_s might be compensated by the reduction of γ_{ow} at evaluated concentrations, as θ_s was around 150° in CTAB solution.

7.2.5 Temporal evolution behavior

In **Figure 7-3**, the different behavior of the temporal evolution at the beginning of the displacement process indicated that the influence of surfactants on the dynamic displacement could take place right after the immersion of the oil droplet into surfactant solutions.

To quantify the temporal evolution of the oil droplet receding process, **Equation (2-27)**, which was widely used for the dynamic analysis of droplet spreading, was modified. Here, we took an alternative considering that the aqueous phase was spreading on the surface. On the assumption that the spreading distance of the TPC line was $(r_{c0} - r_c)$ at t , the following equation was given,

$$\frac{r_{c0} - r_c}{r_{c0}} = B' \left(\frac{\gamma_{ow} t}{\mu r_{c0}} \right)^\alpha = B t^\alpha \quad (7-2)$$

where $\frac{\gamma_{ow} t}{\mu r_{c0}}$ is the dimensionless time and $B = B' \left(\frac{\gamma_{ow} t}{\mu r_{c0}} \right)^\alpha$ is the second fitting parameter other than wetting exponent α .

The plots of $(r_{c0} - r_c)/r_{c0}$ versus t as shown in **Figure 7-4** revealed that r_c and t could be correlated well by **Equation (7-2)** at the early stage. Based on the least-squares method over the data points at the early stage where the data appeared visually linear, B and α were determined (**Figure 7-5**).

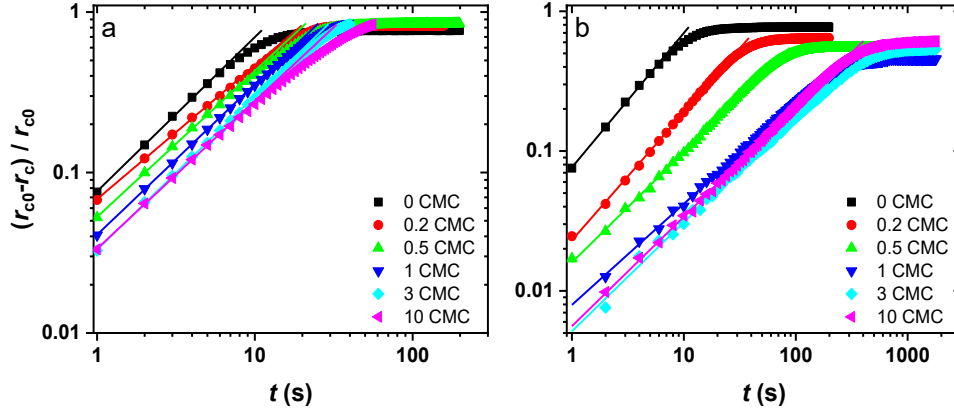


Figure 7-4: Temporal evolution of $(r_{c0} - r_c)/r_{c0}$ during oil displacement in (a) SDBS and (b) CTAB solutions. The straight lines indicate best fits to **Equation (7-2)** at the early stage.

Normally, the behavior of the coefficient B (or B') has attracted less attention and was barely discussed in the literature. Nevertheless, in light of the mathematical nature of **Equation (7-2)**, B quantifies the TPL line motion within the first second of the oil displacement, which could be interpreted as a short initial period in this study. Therefore, the extracted B is expected to provide some general knowledge of the oil displacement dynamics in surfactant solutions at the initial moment. For the case of CTAB solution, B is likely to be ~ 0 due to the negligible TPC line motion. As a result, all types of surfactants studied here could reduce the initial speed of the TPC line motion and the effectiveness followed the order: CTAB > TX-100 > SDBS. In addition, B tended to decrease with surfactant concentration over the low concentration range while only changed slightly as the concentration was increased beyond the CMCs in the solutions of SDBS and TX-100.

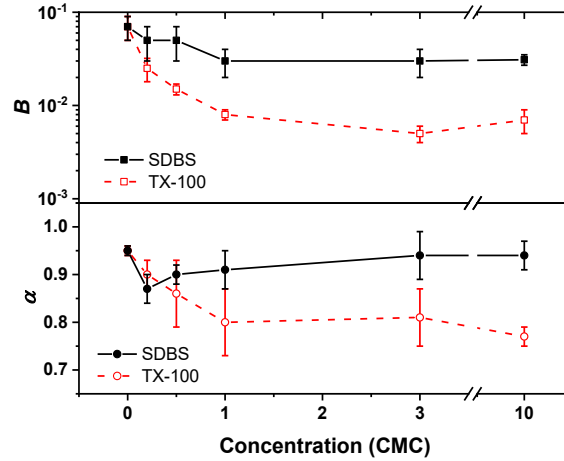


Figure 7-5: Coefficients B and α in Equation (7-2) extracted from the linear fit at the early stage of the oil displacement.

The major driving force (F_d) of the TPC line motion originates from the unbalanced horizontal interfacial tension acting on the TPC line,

$$F_d = \gamma_{os} - \gamma_{sw} + \gamma_{ow} \cos(\pi - \theta_d) \quad (7-3)$$

where θ_d is the dynamic contact angle. It is reasonable to conclude that a weaker F_d could be responsible for a slower motion of the TPC line. Consequently, a hindered TPC line motion within the first second (i.e., smaller B) is anticipated if the surfactant could lower F_d at initial stage due to the adjustment of interfacial tensions. At the beginning of the oil displacement, γ_{os} was unlikely to be significantly altered by surfactant due to non-direct contact of the oil-solid interface to the surfactant solution. The initial θ_d was equivalent to the contact angle of the air phase prior to displacement and stayed nearly identical on the same types of solid surfaces. Since the initial value of θ_d is much larger than 90° , the decrease of B in the presence of surfactants could be easily attributed to the reduction of γ_{ow} . Compared to B of the SDBS solutions, even smaller B of CTAB and TX-100 solutions arose from the increase of γ_{sw} due to the surfactant adsorption into the solid substrate.

In **Figure 7-5**, for the displacement in pure water solution, $\alpha \sim 0.95$ agreed well with the reported value at the early viscous regime.[107] In our study, the early viscous regime could last for a long time due to the extremely high viscosity of the oil.[107] The decrease of α observed in the presence of surfactants suggested that inhibiting mechanisms on the displacement dynamics at the early regime could be introduced by surfactant additions. However, the mechanisms could be different

in the case of SDBS and TX-100 additions, since different responses of α to the increase of the concentration of the corresponding solutions were shown in **Figure 7-5**. For SDBS additions, α slightly decreased to ~ 0.87 at the concentration of 0.2 CMC and then returned to the original value with increasing concentration; the more significant decrease of α was caused by TX-100 additions with increasing the concentration until CMC.

The expansion of the oil-water interface at the edge of the droplet arising from the TPC line motion could establish interfacial tension gradients along the oil-water interface and result in the well-known Marangoni effect. In fact, the Marangoni effect has been widely reported as a very promising mechanism for the enhanced droplet spreading, i.e., the increased wetting exponent in the spreading of surfactant solutions.[94] [98] [100] In our study of the oil droplet receding, as indicated by **Figure 7-6**, the potential Marangoni flow in the oil droplet was supposed to flow towards the TPC line zone (high surface tension zone), which was opposite to the direction of the TPC line motion. As a result, it could not dominate the motion of the TPC line but could introduce an inhibiting mechanism for the decrease of α .

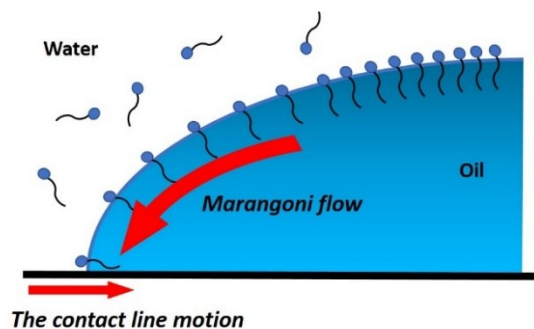


Figure 7-6: Schematic representation of the Marangoni flow in the oil droplet caused by a spatial variation of surfactant adsorption along the oil-water interface.

For the surfactant adsorption at the interface, neither insufficient reduction of the interfacial tension nor fast adsorption rate could contribute to a considerable interfacial tension gradient which is the key factor for the Marangoni effect.[94] In the SDBS solution at the concentration of 0.2 CMC, a remarkable reduction ($\sim 50\%$) of the interfacial tension was indicated in **Figure 7-1**. Referring to the data of the dynamic interfacial tension between hydrocarbon oil and SDBS aqueous solutions in **Figure 7-7a**, the characteristic timescale of the dynamic interfacial tension relaxation was close to that of the early-stage oil displacement in this solution. Thus, it was likely that the Marangoni effect was responsible for the slight decrease of α for SDBS solution at 0.2

CMC. However, the faster relaxation at higher concentration solutions could eliminate such effect on α .

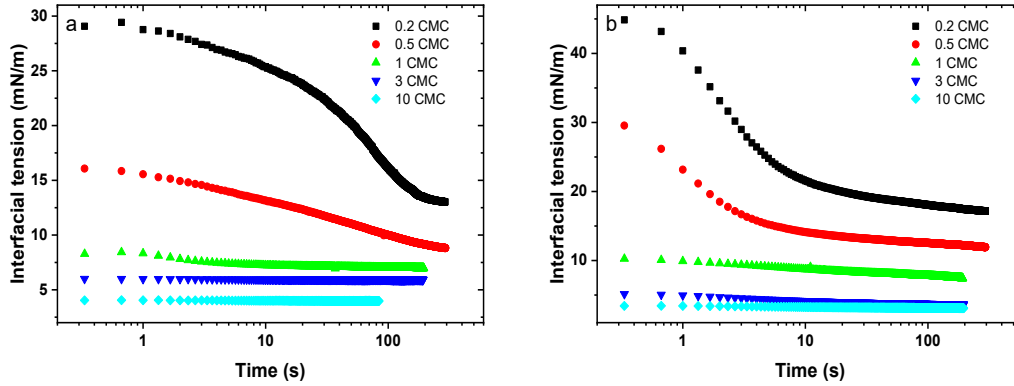


Figure 7-7: The dynamic interfacial tension of hydrocarbon oil (heavy paraffin oil) against (a) SDBS and (b) TX-100 aqueous solutions at various concentrations measured by the theta optical tensiometer using the pendant drop method.

It was found that TX-100 could lead to faster relaxation of the interfacial tension than SDBS (see **Figure 7-7b**). In addition, the lower interfacial expansion rate in TX-100 solutions could be the consequence of the slower oil displacement rate. These factors collectively implied that the Marangoni effect could not be a major contribution to the decreased α observed in TX-100 solutions. As mentioned earlier, the increase of θ_s was observed in TX-100 solutions due to the adsorption of TX-100 molecules on the solid surface. According to the report of Bird et al.[105], the surface hydrophobization could be a potential mechanism for the decreased α in TX-100 solutions. Because of the slow adsorption at the less concentrated solution of TX-100 as indicated by the frequency shifts in **Figure 7-2a**, the small reduction of α at 0.2 CMC TX-100 might be attributed to the less hydrophobized surface at the early stage.

7.2.6 Dependence of U on θ_d

Previous reports [111] [164] as well as the discussion in **Chapter 6** suggested that the dependence of U on θ_d for the oil displacement dynamics of surfactant free systems could be reasonably predicted by the MK and HD models at the regimes of low and relative high velocities, respectively. In this study, most data points were fell into the low velocity range because of the reduced TPCL speed in the presence of surfactant. Therefore, the MK model was expected to be more suitable for

such quantitative analysis. With using the contact angle of the oil phase ($\pi-\theta_d$) here, the MK and linear MK models were rewritten as following equations respectively:

$$U = 2K_0\lambda \sinh\left(\frac{\gamma_{ow}[\cos(\pi - \theta_d) - \cos(\pi - \theta_s)]\lambda^2}{2k_B T}\right) \quad (7-4)$$

$$U = \frac{\gamma_{ow}}{\xi} [\cos(\pi - \theta_d) - \cos(\pi - \theta_s)] = \frac{F_d}{\xi} \quad (7-5)$$

For the linear MK model of **Equation (7-5)**, it implies a simple correlation that cosine functions of experimental dynamic contact angles, $\cos(\pi-\theta_d)$, are proportional to the corresponding U , which is defined to be positive in the case of the oil droplet receding. In what follows, **Equation (7-5)** was extensively applied for the dynamic behavior analysis due to the more convenient form when compared to **Equation (7-4)**. In **Figure 7-8**, $\cos(\pi-\theta_d)$ were plotted against U at each corresponding time. If the dynamics of the displacement is governed by **Equation (7-5)**, the experimental data points on these plots can be fitted by a straight line with a positive slope. It is found that all the data points from low to intermediate velocity regime in each plot follow the linear trend of **Equation (7-5)**. U is observed to achieve the maximum value right after the immersion of the oil droplets into aqueous solutions and afterward decreases rapidly as time evolves. Thus, the MK model may provide a reasonable description of the dynamic behavior at the late stage of the oil displacement. We noticed that the full form of the MK model (**Equation (7-4)**) predicted slightly smaller $\cos(\pi-\theta_d)$ than **Equation (7-5)** at the same U and the difference could become more considerable with the increase of U . Therefore, applying **Equation (7-4)** was unlikely to improve the fit for most cases in **Figure 7-8** as the data points at high-velocity regime shifted above the linear fit of **Equation (7-5)**.

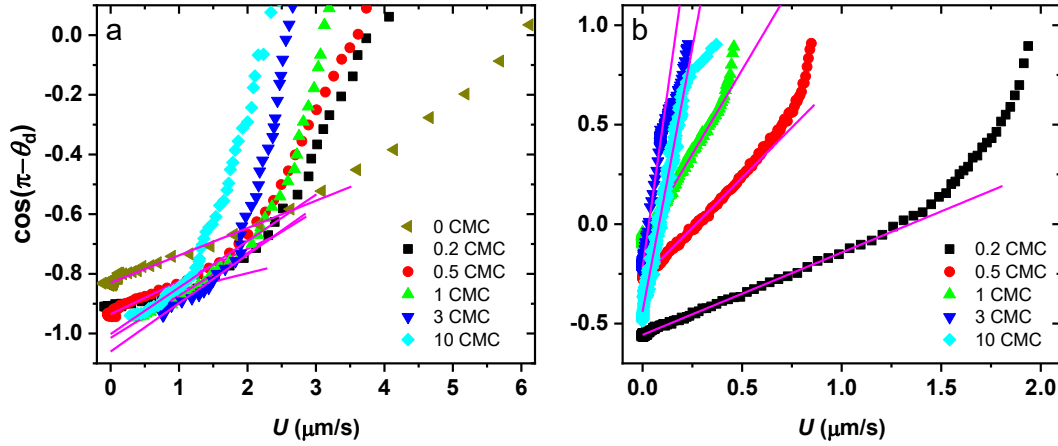


Figure 7-8: Cosine function of the experimental dynamic contact angle as a function of the TPC line velocity obtained from the oil displacement experiments with (a) SDBS and (b) TX-100 addition. The solid lines indicate the best fit of the data points which could be governed by the linear MK model.

It is clear that the deviation of data points with large U from the linear fit in **Figure 7-8** could be attributed to the velocity regime beyond the applicability of the MK model. Other than that, it is likely that surfactant addition could also contribute to the deviation. At the beginning of the displacement, the temporal relaxation of the interfacial energy caused by the kinetics of surfactant adsorption is rather considerable. It should be mentioned that the driving force used in these MK models derives from **Equation (7-3)**. Assuming constant interfacial tensions of all three relevant interfaces, the driving force can be expressed in terms of the static contact angle (θ_s) by combining with **Equation (7-1)**,

$$F_d = \gamma_{ow}[\cos(\pi - \theta_d) - \cos(\pi - \theta_s)] \quad (7-6)$$

However, without constant interfacial tensions, **Equation (7-6)** would no longer be valid. As a result, the linear correlation between $\cos(\pi - \theta_d)$ and U in **Equation (7-5)** could not be established for the data points obtained at the early stage. Over time, because of the nearly saturated surfactant at the interface, the satisfactory fit of the straight line on the data points obtained at the subsequent stage was found.

The contact line friction ζ was extracted from the best fit of these data points to **Equation (7-5)** and listed in **Table 7-3**. In general, surfactant addition could lead to smaller ζ despite larger ζ was observed in high concentration solution of TX-100. The reduction of ζ in SDBS solutions was

more effective than that in TX-100 solutions. Interestingly, ζ in the SDBS micellar solutions was close to the viscosity of the oil phase. According to Blake's theory, it was implied that the contribution from the solid-liquid interaction to ζ was negligible and the fluid viscosity might be the only dominant mechanism for the friction of the moving contact line.

Table 7-3: The ζ extracted by fitting **Equation (7-5)** to the experimental data points at the linear regime in **Figure 7-8**

Concentration (CMC)		0	0.2	0.5	1	3	10
ζ (kPa·s)	SDBS	6±1	3±1	1.4±0.4	1.0±0.3	0.9±0.2	0.5±0.2
	TX-100	6±1	5.9±0.7	1.9±0.4	3±1	9±2	9±1

Blake's theoretical correlation (**Equation (2-19)**) provides a linear dependence of $\ln(\zeta/\mu)$ on W_a if λ and V_L/λ^3 do not vary too much case by case in a specific system. As a result, to further explore the behavior of the TPC line motion in this study, the extracted parameters in **Table 7-3** were plotted in the form of $\ln(\zeta/\mu)$ as a function of the W_a predicted from θ_S through **Equation (2-3)** as shown in **Figure 7-9**. It should be mentioned that the points for SDBS micellar solution could not be plotted at the undefined θ_S .

In **Figure 7-9**, when the concentration is below the CMC, the data points (open red triangles) can be roughly fitted by a straight line with a positive slope (solid black line). In the MK model, λ is used to characterize the mean distance of a single thermally activated elementary jump due to adsorption-desorption process at the TPC line and hence it is typically a few angstroms in the molecular size scale. The estimation of λ from the slope of the linear regression was 1.10 nm. It could not accurately indicate the value of λ due to a rough approximation of **Equation (2-19)** in nature but was in agreement with the concept of λ on the order of magnitude. As the surfactant concentration was further increased beyond the CMC, the linear correlation could not be identified. In **Figure 7-9**, we could see that the point at the CMC (solid blue squares) was still close to the solid black line but solid green circles, which represent the concentration beyond the CMC, were significantly above the line. Thus, **Equation (2-19)** was incapable of describing the data points when a large number of surfactant micelles existed in the displacement system. Analogous

behavior has been reported in the study on the displacement over nano-rough surfaces: Blake's correlation predicted the behavior on smooth surfaces fairly well but failed for surfaces with nanoroughness.[152] It was claimed that the TPC line motion on nano-rough surfaces was still a thermally activated process as the MK model described. However, surface defects at the nanoscale could introduce an additional mechanism of the TPC line pinning-depinning events beyond the pure molecular adsorption-desorption mechanism considered in the MK model. As a result, W_a was inadequate to completely characterize the energy barrier of the thermal activation for the nano-rough surface and the contribution from surface pinning strength was suggested to be added.[14] In our case, when the surfactant concentration was further increased beyond the CMC, it was likely that the behavior of elementary jumps at the TPC line was somehow disturbed in the presence of surfactant micelles. Therefore, the significant deviation of data points from Blake's prediction mentioned above might be related to a mechanism induced by the supramolecular structure of surfactant micelles (e.g., steric hindrance).

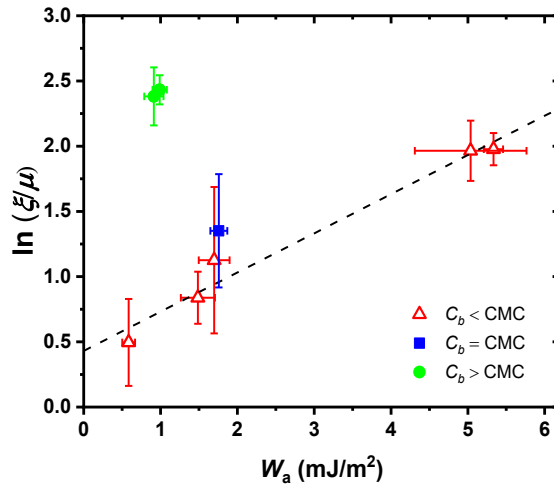


Figure 7-9: The logarithm of the contact line friction coefficients normalized by oil viscosity versus the reversible work of adhesion. The black dash line represents the best fit of Blake's correlation to the data points of surfactant concentration below the CMC.

7.3 Summary

The spontaneous displacement of high viscosity oil by three types of conventional surfactant aqueous solutions over the hydrophilic glass surface has been investigated. At the same

concentration level with respect to the corresponding CMCs, surfactant aqueous solutions studied here exhibited similar interfacial tension against the oil. Nevertheless, an outstanding difference of the interaction between surfactant molecules and the solid surface could lead to dramatically different ultimate extent of oil displacement as observed in our experiments: CTAB and TX-100 solutions were detrimental to the oil displacement, while smaller final oil-solid contact area could be achieved in SDBS solutions. The improved static displacement did not correspond to faster dynamics. In fact, the initial contact line motion was found to be inhibited by any type of surfactant additions.

Quantitative analysis of the dynamic behavior revealed that the oil displacement at the early stage could be described by a power law correlation of time-dependence. Surfactant-induced mechanisms could lead to the reduction of the wetting exponent α extracted from the early stage. For the late stage, the dynamic behavior of the dependence of U on θ_d satisfactorily agreed with the description of the MK model. Blake's theory could reasonably correlate the friction coefficient ζ in the MK model and the apparent adhesion energy until the surfactant concentration above the CMC where additional mechanism might be induced by surfactant micelles.

Chapter 8

Conclusions and implications

8.1 Conclusions

The phenomenon of spontaneous displacement of fluids is involved in many technical applications. This Ph.D. project was motivated by having an in-depth understanding of high viscosity bitumen displaced by aqueous solutions over sand grains during the industrial process of water-based oil sands extraction. The research focused on the spontaneous displacement of high viscosity micrometer-sized oil droplets from a curved solid in an aqueous environment.

The modified micropipette system was utilized for the experimental investigation. The oil displacement was recorded as sequential digital images, and quantitative characterizations of the process, such as the instantaneous oil-solid contact area, contact angle, velocity of the TPCL and deviation factor, were extracted via the digital image analysis. The image-based contact angle determination was extensively discussed, and the circle, local circle and apex circle fitting methods were adopted. The systematic error analysis on these methods suggested that the relative lower exposure time and exactly on-focus shot during the image acquisition were beneficial for gaining more reliable contact angle values.

The interfacial tension of the high viscosity sample oils against the aqueous phase, which is an important physicochemical property related to the displacement behavior, has been measured by the drop shape relaxation method due to the difficulty of the measurement using conventional techniques of tensiometry. For this measurement, the highly efficient BLS method was implemented to theoretically predict the drop shape during an axisymmetric relaxation. The corresponding experiments of micron size oil droplet relaxation were conducted using the micropipette experimental system. The interfacial tension was finally determined by matching the experimental data to the theoretical curve.

The investigation of the oil displacement in pure water suggested that a faster dynamics and higher final degree of oil liberation could occur on a more hydrophilic surface. On the other hand, the

increase in oil viscosity, surface curvature or droplet volume has an adverse effect on the oil displacement dynamics but a negligible impact on the final state. The image analysis has shown the non-spherical cap shape of the dynamic droplet, which is inconsistent with the thermodynamic consideration and may cause considerable errors in the dynamic contact angle determination by using the “quasi-static spherical cap approximation”. The relative significance of the viscous stress to the capillary stress on the interface near the TPCL was responsible for the peculiar droplet shape. The quantitative analysis of the dynamic process described in the MK and HD models was performed by applying experimental dynamic contact angles obtained from different methods. It has been found that the degree of droplet shape deviation from the spherical segment could indicate the applicability of each model: the MK model described the dynamic behavior fairly well for small departure from the spherical cap shape, while the HD model was more suitable for larger shape departures and at higher contact line velocities. The flow of the high viscosity oil at the initial receding stage could cause complicated dynamic behaviors beyond what is considered by conventional dynamic wetting models.

Further study of the oil displacement in surfactant aqueous solutions revealed that the final static configurations of the oil droplets could be considerably affected by the different adsorption behavior of surfactants at the water-solid interface. Moreover, surfactant additions could slow down the initial motion of the TPCL regardless of surfactant types. It was found that the dynamic behavior of the oil displacement could quantitatively agree with a power law correlation of time-dependence and the dependence of U on θ_d in the description of the MK model at the early and late stages, respectively. The modified dynamic behavior in the presence surfactant was attributed to several potential surfactant-induced mechanisms which are supposed to be elucidated in a future study.

8.2 Practical implications for water-based oil sands extraction

In this section, results from the investigation on the displacement of the model oil are correlated to the bitumen liberation in the practical process and hence expected to offer implications on the industrial operation.

According to this study, oil sand ores with more hydrophilic sand grain surfaces are favorably processed due to the enhanced bitumen liberation from both static and dynamic perspectives.

Generally, most sand grain surfaces in oil sands are intrinsically hydrophilic; however, some components in bitumen, such as asphaltenes and/or organic acids, may contaminate the sand grain surface via irreversible adsorptions and thereby increase the hydrophobicity of the surface.[184] [185] [186] Moreover, it was reported that the effect of weathering arising from the exposure of oil sands ores to an external environment could intensify such contamination.[187] Therefore, caution should be taken to alleviate the weathering effect during mining or storage of oil sands ores. On the other hand, feasible functional chemicals could be added to modify the wettability of the surface during processing.[188] [189]

As high viscosity of fluid was demonstrated to considerably slow down the oil displacement rate, reducing the bitumen viscosity could be an efficient way to speed up the bitumen liberation and save processing time. The viscosity of bitumen could be readily reduced by increasing temperature or diluting via the addition of low viscosity solvents. Because of the high energy cost of high operating temperature, solvent addition turns out to be a better choice in practice. In fact, the solvent-assisted bitumen extraction process has been proved to be a promising technology according to several lab scale studies.[190] [191]

The displacement over larger sand grains of less curved surfaces could lead to faster oil liberation. However, it was found that the effect of grain size is marginal. Thus, the corresponding control in the operation might not be an efficient way to improve bitumen liberation.

This study exhibits the benefit of a smaller volume of the receding oil droplet in shortening the liberation time. To decrease the volume of the receding bitumen droplet, in practice, the generation of more rupture points of the bitumen layer on the sand grain is expected prior to the displacement. In light of the literature reports [192] [193], the spontaneous rupture of a thin liquid film covered on solids is likely to occur when the thickness of the film is reduced to a critical value under the effect of film thinning caused by the hydrodynamic force. Thus, it is recommended to input more hydrodynamic energy into the slurry to generate more rupture points and hence speed up the bitumen liberation.

In contrast to the high viscosity model oil with a pure component used in this study, bitumen is a complex mixture with indigenous natural surfactants. Typically, naphthenic acids, sulfonate acids and asphaltenes are major sources of natural surfactants in crude bituminous oil. The dissociation of the acid groups in these sources could result in the release of the natural surfactants from the oil

bulk and hence lower the oil-water interfacial tension.[194] [195] Because of the anionic nature of most dissociated acidic molecules, the natural surfactant releasing could enhance the degree of the bitumen liberation due to the normally negatively-charged sand grain surface of the oil sands. Increasing the pH of aqueous solutions has been demonstrated to be an effective and convenient way to facilitate the release of the natural surfactant.[23] For the industrial process, the released natural surfactant in the process water may become gradually concentrated as part of the water comes from the recycling plant.[196] Although these natural surfactants could improve the degree of bitumen liberation, the recycled water enriched with surfactants may be added subsequent to fresh water to optimize the dynamic process since our study suggests surfactant additions could have a negative impact on the displacement speed at the early stage.

Besides the release of the indigenous surfactants, the addition of external surfactants with more interfacial activity could be another option in controlling the liberation process. However, the interaction between the externally added surfactant molecules and the solid surface should be carefully examined since unreasonable selections of external surfactants might be detrimental to the bitumen liberation and cause significant surfactant loss during processing.

Appendix A

Numerical implementation of the BLS method

To describe the axisymmetric drop shape in the numerical analysis, the profile was characterized by a series of closely spaced nodal points along the meridian curve in a cylindrical coordinate system (r, z) as shown in **Figure A-1**. Here the azimuthal angle in the coordinates was no longer required due to the axial symmetry. The completed surface could be formed by the rotation of the meridian curve around the z axis. The nodal point i (r_i, z_i) could be converted into the spherical coordinate (R_i, β_i) where the Happel's solutions are as

$$\beta_i = \cos^{-1}\left(\frac{z_i}{\sqrt{r_i^2 + z_i^2}}\right) \quad \text{or} \quad \beta_i = \sin^{-1}\left(\frac{r_i}{\sqrt{r_i^2 + z_i^2}}\right) \quad (\text{A-1})$$

$$R_i = \sqrt{r_i^2 + z_i^2} \quad (\text{A-2})$$

In addition, the mean curvature (J_c) at that nodal point could be estimated numerically with the following equation,

$$J_c = Fr_i \cdot Fzz_i - Fz_i \cdot Frr_i + \frac{Fz_i}{r_i} \quad (\text{A-3})$$

where

$$Fr_i = \frac{1}{2} \left(\frac{r_{i+1} - r_i}{\sqrt{(r_{i+1} - r_i)^2 + (z_{i+1} - z_i)^2}} + \frac{r_i - r_{i-1}}{\sqrt{(r_i - r_{i-1})^2 + (z_i - z_{i-1})^2}} \right)$$

$$Fz_i = \frac{1}{2} \left(\frac{z_{i+1} - z_i}{\sqrt{(r_{i+1} - r_i)^2 + (z_{i+1} - z_i)^2}} + \frac{z_i - z_{i-1}}{\sqrt{(r_i - r_{i-1})^2 + (z_i - z_{i-1})^2}} \right)$$

$$Frr_i = 2 \frac{\frac{r_{i+1} - r_i}{\sqrt{(r_{i+1} - r_i)^2 + (z_{i+1} - z_i)^2}} - \frac{r_i - r_{i-1}}{\sqrt{(r_i - r_{i-1})^2 + (z_i - z_{i-1})^2}}}{\sqrt{(r_{i+1} - r_i)^2 + (z_{i+1} - z_i)^2} + \sqrt{(r_i - r_{i-1})^2 + (z_i - z_{i-1})^2}}$$

$$Fzz_i = 2 \frac{\frac{z_{i+1} - z_i}{\sqrt{(r_{i+1} - r_i)^2 + (z_{i+1} - z_i)^2}} - \frac{z_i - z_{i-1}}{\sqrt{(r_i - r_{i-1})^2 + (z_i - z_{i-1})^2}}}{\sqrt{(r_{i+1} - r_i)^2 + (z_{i+1} - z_i)^2} + \sqrt{(r_i - r_{i-1})^2 + (z_i - z_{i-1})^2}}$$

According to Young-Laplace equation, T appearing in **Equation (5-16)** could be evaluated with the known J_c and resolved into two components (T_R and T_β) in the spherical coordinate system,

$$T_R = \gamma J_c \cos \varphi \quad (\text{A-4})$$

$$T_\beta = \gamma J_c \sin \varphi \quad (\text{A-5})$$

where γ is interfacial tension between interior and exterior fluid and φ is defined as the angle between the outward normal vector to the interface and the vector pointed to interface from the center of the spherical coordinate system as indicated in **Figure A-1**.

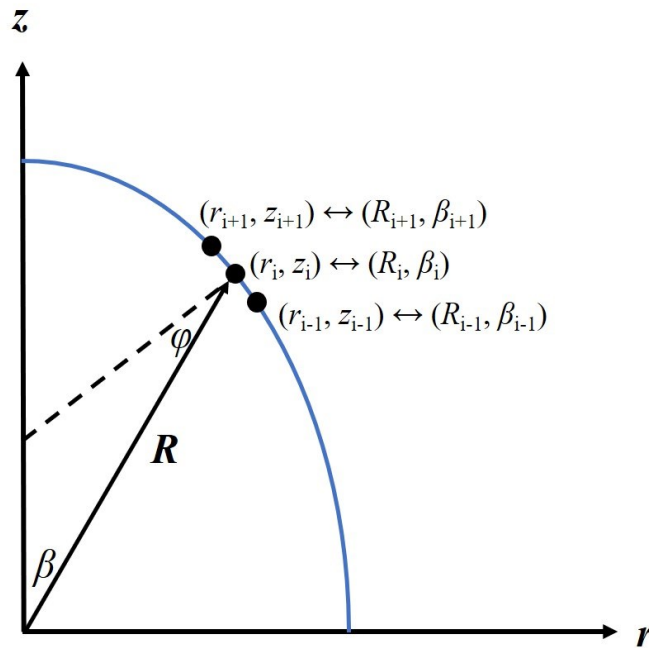


Figure A-1: The schematic of a drop profile (blue line) characterized by a series of nodal points in the numerical procedure.

As for σ in **Equation (5-16)**, the two resolved components (σ_R and σ_β) in the spherical coordinate system could be written as

$$\sigma_R = \tau_{RR} \cos \varphi + \tau_{R\beta} \sin \varphi \quad (\text{A-6})$$

$$\sigma_\beta = \tau_{R\beta} \cos \varphi + \tau_{\beta\beta} \sin \varphi \quad (\text{A-7})$$

where τ_{RR} , $\tau_{R\beta}$ and $\tau_{\beta\beta}$ are the stress tensor of fluid and could be evaluated with the following equations in the case of incompressible Newtonian fluid,

$$\tau_{RR} = -p + 2\mu \frac{\partial v_R}{\partial R} \quad (\text{A-8})$$

$$\tau_{\beta\beta} = -p + 2\mu \left(\frac{1}{R} \frac{\partial v_\beta}{\partial \beta} + \frac{v_R}{R} \right) \quad (\text{A-9})$$

$$\tau_{R\beta} = \mu \left(\frac{1}{R} \frac{\partial v_R}{\partial \beta} + \frac{\partial v_\beta}{\partial R} - \frac{v_\beta}{R} \right) \quad (\text{A-10})$$

To calculate the surface integration in **Equation (5-16)** numerically, the interface on the r - z plane was divided into subintervals by the nodal points. Using the simple trapezoidal rule at each subinterval, the integration could be approximated to be the following summation,

$$M_{\text{BLS}} = \frac{1}{2} \sum_{i=2}^{n_p-1} \left\{ \left[(\mathbf{v}_i(r_i, z_i) - \mathbf{v}_e(r_i, z_i))^2 + (\boldsymbol{\sigma}_i(r_i, z_i) - \boldsymbol{\sigma}_e(r_i, z_i) + \mathbf{T}(r_i, z_i))^2 \right] \right. \\ \left. \times \pi r_i \left[\sqrt{(r_{i+1} - r_i)^2 + (z_{i+1} - z_i)^2} + \sqrt{(r_i - r_{i-1})^2 + (z_i - z_{i-1})^2} \right] \right\} \quad (\text{A-11})$$

With the expressions regarding \mathbf{T} and $\boldsymbol{\sigma}$, the Happel's solutions could be substituted into **Equation (A-11)** step by step to form an equation of a_i . It is not difficult to see such equation is quadratic. Therefore, deriving the first derivative of M_{BLS} with respect to a_i as described in **Equation (5-17)** could yield linear equations of a_i . The unknown parameter of a_i could be readily determined by solving these simple linear equations. The velocity and pressure fields at that moment could be determined as well by substituting a_i back to the Happel's solutions.

Assuming the constant velocity of the interface within a short dimensionless time step (Δt_c), the Euler-type integration was conducted to simulate the temporal evolution of the drop shape,

$$R(t_c + \Delta t_c) = R(t_c) + v_R \Delta t_c \quad (\text{A-12})$$

$$\beta(t_c + \Delta t_c) = \beta(t_c) + v_\beta \Delta t_c \quad (\text{A-13})$$

Bibliography

- [1] T. F. Svitova, R. M. Hill, and C. J. Radke, “Spreading of Aqueous Dimethyldidodecylammonium Bromide Surfactant Droplets over Liquid Hydrocarbon Substrates,” *Langmuir*, 1999.
- [2] P. A. Ash, C. D. Bain, and H. Matsubara, “Wetting in oil/water/surfactant systems,” *Current Opinion in Colloid and Interface Science*. 2012.
- [3] T. Young, “An Essay on the Cohesion of Fluids,” *Philos. Trans. R. Soc. London*, vol. 95, no. 0, pp. 65–87, 1805.
- [4] M. A. Dupré, “Théorie mécanique de la chaleur.,” *Ann. Chim. Phys.*, vol. 4, no. 11, pp. 194–220, 1867.
- [5] W. A. Zisman, “Relation of equilibrium contact angle to liquid and solid constitution,” in *Contact Angle, Wettability, and Adhesion*, vol. 43, 1964, pp. 1–51.
- [6] C. Huh and L. E. Scriven, “Hydrodynamic model of steady movement of a solid / liquid / fluid contact line,” *J. Colloid Interface Sci.*, vol. 35, no. 1, pp. 85–101, 1971.
- [7] E. B. Dussan V. and S. H. Davis, “On the motion of a fluid-fluid interface along a solid surface,” *J. Fluid Mech.*, 1974.
- [8] F. Brochard and P. G. de Gennes, “Spreading laws for liquid polymer droplets : interpretation of the « foot »,” *J. Phys. Lettres*, vol. 45, no. 12, pp. 597–602, Jun. 1984.
- [9] R. L. Hoffman, “A study of the advancing interface. I. Interface shape in liquid-gas systems,” *J. Colloid Interface Sci.*, 1975.
- [10] L. H. Tanner, “The spreading of silicone oil drops on horizontal surfaces,” *J. Phys. D. Appl. Phys.*, 1979.
- [11] T. D. Blake and J. M. Haynes, “Kinetics of liquidliquid displacement,” *J. Colloid Interface Sci.*, vol. 30, no. 3, pp. 421–423, 1969.
- [12] R. G. Cox, “The dynamics of the spreading of liquids on a solid surface. Part 1. Viscous flow,” *J. Fluid Mech.*, vol. 168, pp. 169–194, 1986.

- [13] P. G. De Gennes, "Wetting: Statics and dynamics," *Rev. Mod. Phys.*, vol. 57, no. 3, pp. 827–863, 1985.
- [14] M. Ramiasa *et al.*, "Contact line motion on nanorough surfaces: A thermally activated process," *J. Am. Chem. Soc.*, vol. 135, no. 19, pp. 7159–7171, 2013.
- [15] G. McHale, M. I. Newton, and N. J. Shirtcliffe, "Dynamic wetting and spreading and the role of topography.," *J. Phys. Condens. Matter*, vol. 21, no. 46, p. 464122, 2009.
- [16] D. Brutin and V. Starov, "Recent advances in droplet wetting and evaporation," *Chemical Society Reviews*. 2018.
- [17] Y. Wei, E. Rame, L. M. Walker, and S. Garoff, "Dynamic wetting with viscous Newtonian and non-Newtonian fluids," *J. Phys. Condens. Matter*, 2009.
- [18] G. K. Seevaratnam, Y. Suo, E. Ramé, L. M. Walker, and S. Garoff, "Dynamic wetting of shear thinning fluids," *Phys. Fluids*, 2007.
- [19] K. Sefiane, J. Skilling, and J. MacGillivray, "Contact line motion and dynamic wetting of nanofluid solutions," *Advances in Colloid and Interface Science*. 2008.
- [20] A. Nikolov and D. Wasan, "Current opinion in superspreading mechanisms," *Advances in Colloid and Interface Science*, vol. 222. pp. 517–529, 2015.
- [21] J. Venzmer, "Superspreading - 20years of physicochemical research," *Current Opinion in Colloid and Interface Science*. 2011.
- [22] P. B. Madden and J. D. Morawski, "The Future of the Canadian Oil Sands: Engineering and Project Management Advances," *Energy Environ.*, vol. 22, no. 5, pp. 579–596, Jul. 2011.
- [23] L. L. Schramm, E. N. Stasiuk, and M. D. MacKinnon, "Surfactants in Athabasca Oil Sands Slurry Conditioning, Flotation Recovery, and Tailings Processes," in *Surfactants: Fundamentals and Applications in the Petroleum Industry*, 2000.
- [24] K. A. Clark and D. S. Pasternack, "Hot Water Separation of Bitumen from Alberta Bituminous Sand," *Ind. Eng. Chem.*, 1932.
- [25] J. Masliyah, Z. J. Zhou, Z. Xu, J. Czarnecki, and H. Hamza, "Understanding Water-Based Bitumen Extraction from Athabasca Oil Sands," *Can. J. Chem. Eng.*, vol. 82, no. 4, pp.

- 628–654, 2004.
- [26] V. Wallwork, Z. Xu, and J. Masliyah, “Processibility of Athabasca Oil Sand Using a Laboratory Hydrot ransport Extraction System (LHES),” *Can. J. Chem. Eng.*, 2004.
- [27] E. C. Sanford, “Processibility of athabasca oil sand: Interrelationship between oil sand fine solids, process aids, mechanical energy and oil sand age after mining,” *Can. J. Chem. Eng.*, 1983.
- [28] T. E. Havre, J. Sjöblom, and J. E. Vindstad, “Oil/water-partitioning and interfacial behavior of naphthenic acids,” *J. Dispers. Sci. Technol.*, 2003.
- [29] S. Ross and P. Becher, “The history of the spreading coefficient,” *J. Colloid Interface Sci.*, 1992.
- [30] D. Bonn, J. Eggers, J. Indekeu, and J. Meunier, “Wetting and spreading,” *Rev. Mod. Phys.*, vol. 81, no. 2, pp. 739–805, 2009.
- [31] A. Amirfazli and A. W. Neumann, “Status of the three-phase line tension: a review,” *Adv. Colloid Interface Sci.*, 2004.
- [32] M. Ramiasa, J. Ralston, R. Fetzer, and R. Sedev, “The influence of topography on dynamic wetting,” *Advances in Colloid and Interface Science*. 2014.
- [33] L. Gao and T. J. McCarthy, “Contact angle hysteresis explained,” *Langmuir*. 2006.
- [34] H. Hervet and P.-G. de Gennes, “The dynamics of wetting: Precursor films in the wetting of ‘dry’ solids,” *C. R. Acad. Sci.*, 1984.
- [35] P. A. Thompson and S. M. Troian, “A general boundary condition for liquid flow at solid surfaces,” *Nature*, 1997.
- [36] D. E. Weidner and L. W. Schwartz, “Contact-line motion of shear-thinning liquids,” *Phys. Fluids*, vol. 6, no. 4, p. 3535, 1994.
- [37] J. Ralston, M. Popescu, and R. Sedev, “Dynamics of Wetting from an Experimental Point of View,” *Annu. Rev. Mater. Res.*, vol. 38, no. 1, pp. 23–43, 2008.
- [38] A. Mohammad Karim, S. H. Davis, and H. P. Kavehpour, “Forced versus spontaneous spreading of liquids,” *Langmuir*, 2016.

- [39] T. D. Blake, “The physics of moving wetting lines,” *J. Colloid Interface Sci.*, vol. 299, no. 1, pp. 1–13, 2006.
- [40] O. V. Voinov, “Hydrodynamics of wetting,” *Fluid Dyn.*, vol. 11, no. 5, pp. 714–721, 1976.
- [41] Y. D. Shikhmurzaev, “Moving contact lines in liquid/liquid/solid systems,” *J. Fluid Mech.*, 1997.
- [42] T. D. Blake, M. Bracke, and Y. D. Shikhmurzaev, “Experimental evidence of nonlocal hydrodynamic influence on the dynamic contact angle,” *Phys. Fluids*, 1999.
- [43] D. Seveno, A. Vaillant, R. Rioboo, H. Adão, J. Conti, and J. De Coninck, “Dynamics of wetting revisited,” *Langmuir*, vol. 25, no. 22, pp. 13034–13044, 2009.
- [44] H. Eyring, “The activated complex and the absolute rate of chemical reactions,” *Chem. Rev.*, 1935.
- [45] T. D. Blake and J. De Coninck, “The influence of solid-liquid interactions on dynamic wetting,” *Adv. Colloid Interface Sci.*, vol. 96, pp. 21–36, 2002.
- [46] S. Glasstone, K. J. Laidler, and H. Eyring, *The theory of rate processes*. 1941.
- [47] D. Duivier, D. Seveno, R. Rioboo, T. D. Blake, and J. De Coninck, “Experimental evidence of the role of viscosity in the molecular kinetic theory of dynamic wetting,” *Langmuir*, vol. 27, no. 21, pp. 13015–13021, 2011.
- [48] H. Li, M. Paneru, R. Sedev, and J. Ralston, “Dynamic Electrowetting and Dewetting of Ionic Liquids at a Hydrophobic Solid–Liquid Interface,” *Langmuir*, vol. 29, no. 8, pp. 2631–2639, Feb. 2013.
- [49] M. J. Vega *et al.*, “Experimental investigation of the link between static and dynamic wetting by forced wetting of nylon filament,” *Langmuir*, vol. 23, no. 21, pp. 10628–10634, 2007.
- [50] M. Ramiasa, J. Ralston, R. Fetzer, and R. Sedev, “Contact line friction in liquid-liquid displacement on hydrophobic surfaces,” *J. Phys. Chem. C*, vol. 115, no. 50, pp. 24975–24986, 2011.
- [51] S. Goossens, D. Seveno, R. Rioboo, A. Vaillant, J. Conti, and J. De Coninck, “Can We Predict the Spreading of a Two-Liquid System from the Spreading of the Corresponding

- Liquid–Air Systems?,” *Langmuir*, vol. 27, no. 16, pp. 9866–9872, Aug. 2011.
- [52] P. Petrov and I. Petrov, “A combined molecular-hydrodynamic approach to wetting kinetics,” *Langmuir*, vol. 8, no. 7, pp. 1762–1767, 1992.
- [53] M. J. de Ruijter, J. de Coninck, and G. Oshanin, “Droplet Spreading–Partial Wetting Regime Revisited,” *Langmuir*, no. 20, pp. 2209–2216, 1999.
- [54] R. A. Hayes and J. Ralston, “Forced liquid movement on low energy surfaces,” *J. Colloid Interface Sci.*, 1993.
- [55] M. Schneemilch, R. A. Hayes, J. G. Petrov, and J. Ralston, “Dynamic Wetting and Dewetting of a Low-Energy Surface by Pure Liquids,” *Langmuir*, 1998.
- [56] C. F. Brooks, A. M. Grillet, and J. A. Emerson, “Experimental investigation of the spontaneous wetting of polymers and polymer blends,” *Langmuir*, vol. 22, no. 24, pp. 9928–9941, 2006.
- [57] R. Fetzer, M. Ramiasa, and J. Ralston, “Dynamics of liquid-liquid displacement,” *Langmuir*, vol. 25, no. 14, pp. 8069–8074, 2009.
- [58] J. Marsh, S. Garoff, and E. Dussan V., “Dynamic contact angles and hydrodynamics near a moving contact line,” *Phys. Rev. Lett.*, vol. 70, no. 18, pp. 2778–2781, 1993.
- [59] E. Ramé and S. Garoff, “Microscopic and macroscopic dynamic interface shapes and the interpretation of dynamic contact angles,” *J. Colloid Interface Sci.*, vol. 177, no. 0026, pp. 234–244, 1996.
- [60] T. F. Tadros, *Applied Surfactants: Principles and Applications*. 2005.
- [61] Z. Q. Li *et al.*, “Effect of zwitterionic surfactants on wetting of quartz surfaces,” *Colloids Surfaces A Physicochem. Eng. Asp.*, vol. 430, pp. 110–116, 2013.
- [62] F. M. Menger and C. A. Littau, “Gemini Surfactants: A New Class of Self-Assembling Molecules,” *J. Am. Chem. Soc.*, 1993.
- [63] R. G. Shrestha *et al.*, “Peptide-based gemini amphiphiles: Phase behavior and rheology of wormlike micelles,” *Langmuir*, 2012.
- [64] W. C. Griffin, “Classification of surface-active agents by "HLB",” *J. Soc. Cosmet. Chem.*,

- vol. 1, no. 5, pp. 311–326, 1949.
- [65] R. C. Pasquali, M. P. Taurozzi, and C. Bregni, “Some considerations about the hydrophilic-lipophilic balance system,” *Int. J. Pharm.*, 2008.
- [66] W. C. Griffin, “Calculation of HLB Values of Non-Ionic Surfactants,” *J. Soc. Cosmet. Chem.*, 1954.
- [67] D. Myers and John Wiley & Sons., *Surfactant science and technology*. J. Wiley, 2006.
- [68] B. Soediono, *Handbook of Surfactants*. 1989.
- [69] H.-J. H. Butt *et al.*, *Physics and Chemistry of Interfaces*. 2006.
- [70] J. N. Israelachvili, D. J. Mitchell, and B. W. Ninham, “Theory of self-assembly of hydrocarbon amphiphiles into micelles and bilayers,” *Journal of the Chemical Society, Faraday Transactions 2: Molecular and Chemical Physics*. 1976.
- [71] D. F. Evans and H. Wennerström, *The Colloidal Domain: Where physics, chemistry, biology and technology meet*. 1999.
- [72] R. Zhang and P. Somasundaran, “Advances in adsorption of surfactants and their mixtures at solid/solution interfaces,” *Advances in Colloid and Interface Science*, vol. 123–126, no. SPEC. ISS. pp. 213–229, 2006.
- [73] R. Miller, E. V. Aksenenko, and V. B. Fainerman, “Dynamic interfacial tension of surfactant solutions,” *Advances in Colloid and Interface Science*, vol. 247. pp. 115–129, 2017.
- [74] A. F. H. Ward and L. Tordai, “Time-dependence of boundary tensions of solutions I. The role of diffusion in time-effects,” *J. Chem. Phys.*, vol. 14, no. 7, pp. 453–461, 1946.
- [75] Y. He, P. Yazhgur, A. Salonen, and D. Langevin, “Adsorption-desorption kinetics of surfactants at liquid surfaces,” *Advances in Colloid and Interface Science*. 2015.
- [76] T. Horozov and L. Arnaudov, “Adsorption kinetics of some polyethylene glycol octylphenyl ethers studied by the fast formed drop technique,” *J. Colloid Interface Sci.*, 2000.
- [77] A. Marmur and M. D. Lelah, “The spreading of aqueous surfactant solutions on glass,”

Chem. Eng. Commun., 1981.

- [78] L. Zhang *et al.*, “Wettability of a quartz surface in the presence of four cationic surfactants,” *Langmuir*, 2010.
- [79] S.-S. Hu *et al.*, “Adsorption behaviors of novel betaines on the wettability of the quartz surface,” *Soft Matter*, vol. 11, no. 40, pp. 7960–8, Oct. 2015.
- [80] K. Szymczyk and B. Jańczuk, “Wettability of a glass surface in the presence of two nonionic surfactant mixtures,” *Langmuir*, 2008.
- [81] K. Szymczyk and B. Jańczuk, “The wettability of polytetrafluoroethylene by aqueous solution of cetyltrimethylammonium bromide and Triton X-100 mixtures,” *J. Colloid Interface Sci.*, vol. 303, no. 1, pp. 319–325, Nov. 2006.
- [82] K. Szymczyk and B. Jańczuk, “Wettability of a polytetrafluoroethylene surface by an aqueous solution of two nonionic surfactant mixtures,” *Langmuir*, 2007.
- [83] K. Szymczyk and B. Jańczuk, “The wettability of poly(tetrafluoroethylene) by aqueous solutions of ternary surfactant mixtures,” *Appl. Surf. Sci.*, vol. 256, no. 24, pp. 7478–7483, Oct. 2010.
- [84] A. Zdziennicka, B. Jańczuk, and W. Wójcik, “The wettability of polytetrafluoroethylene by aqueous solutions of sodium dodecyl sulfate and propanol mixtures,” *J. Colloid Interface Sci.*, vol. 281, no. 2, pp. 465–472, 2005.
- [85] N. Kumar, A. Couzis, and C. Maldarelli, “Measurement of the kinetic rate constants for the adsorption of superspreading trisiloxanes to an air/aqueous interface and the relevance of these measurements to the mechanism of superspreading,” *J. Colloid Interface Sci.*, 2003.
- [86] N. M. Kovalchuk, A. Trybala, O. Arjmandi-Tash, and V. Starov, “Surfactant-enhanced spreading: Experimental achievements and possible mechanisms,” *Adv. Colloid Interface Sci.*, vol. 233, pp. 155–160, Jul. 2016.
- [87] M. Mohammed and T. Babadagli, “Wettability alteration: A comprehensive review of materials/methods and testing the selected ones on heavy-oil containing oil-wet systems,” *Adv. Colloid Interface Sci.*, vol. 220, pp. 54–77, Jun. 2015.
- [88] S. Ma, X. Zhang, N. R. Morrow, and X. Zhou, “Characterization of wettability from

- spontaneous imbibition measurements,” *J. Can. Pet. Technol.*, 1999.
- [89] B. Hou *et al.*, “Mechanisms of Enhanced Oil Recovery by Surfactant-Induced Wettability Alteration,” *J. Dispers. Sci. Technol.*, vol. 37, no. 9, pp. 1259–1267, Sep. 2016.
- [90] D. C. Standnes and T. Austad, “Wettability alteration in chalk 2. Mechanism for wettability alteration from oil-wet to water-wet using surfactants,” *J. Pet. Sci. Eng.*, 2000.
- [91] T. Austad, B. Matre, J. Milter, A. Sævareid, and L. Øyno, “Chemical flooding of oil reservoirs 8. Spontaneous oil expulsion from oil- and water-wet low permeable chalk material by imbibition of aqueous surfactant solutions,” *Colloids Surfaces A Physicochem. Eng. Asp.*, 1998.
- [92] X. Xie, W. W. Weiss, Z. Tong, and N. R. Morrow, “Improved Oil Recovery From Carbonate Reservoirs by Chemical Stimulation,” *SPE J.*, 2005.
- [93] M. Salehi, S. J. Johnson, and J. T. Liang, “Mechanistic study of wettability alteration using surfactants with applications in naturally fractured reservoirs,” *Langmuir*, 2008.
- [94] A. D. Nikolov, D. T. Wasan, A. Chengara, K. Koczó, G. A. Policello, and I. Kolossvary, “Superspreading driven by Marangoni flow,” *Adv. Colloid Interface Sci.*, vol. 96, no. 1–3, pp. 325–338, 2002.
- [95] A. Patist, S. G. Oh, R. Leung, and D. O. Shah, “Kinetics of micellization: Its significance to technological processes,” *Colloids Surfaces A Physicochem. Eng. Asp.*, vol. 176, no. 1, pp. 3–16, 2001.
- [96] A. Patist, J. R. Kanicky, P. K. Shukla, and D. O. Shah, “Importance of micellar kinetics in relation to technological processes,” *Journal of Colloid and Interface Science*, vol. 245, no. 1, pp. 1–15, 2002.
- [97] V. B. Fainerman, V. D. Mys, A. V. Makievski, J. T. Petkov, and R. Miller, “Dynamic surface tension of micellar solutions in the millisecond and submillisecond time range,” *J. Colloid Interface Sci.*, vol. 302, no. 1, pp. 40–46, 2006.
- [98] X. Wang, L. Chen, E. Bonaccorso, and J. Venzmer, “Dynamic wetting of hydrophobic polymers by aqueous surfactant and superspreader solutions,” *Langmuir*, vol. 29, no. 48, pp. 14855–14864, 2013.

- [99] N. Kovalchuk, A. Trybala, F. Mahdi, and V. Starov, “Kinetics of spreading of synergetic surfactant mixtures in the case of partial wetting,” *Colloids Surfaces A Physicochem. Eng. Asp.*, vol. 505, pp. 23–28, 2016.
- [100] N. M. Kovalchuk, O. K. Matar, R. V. Craster, R. Miller, and V. M. Starov, “The effect of adsorption kinetics on the rate of surfactant-enhanced spreading,” *Soft Matter*, vol. 12, no. 4, pp. 1009–1013, 2016.
- [101] S. Rafai, D. Sarker, V. Bergeron, J. Meunier, and D. Bonn, “Superspreading: Aqueous surfactant drops spreading on hydrophobic surfaces,” *Langmuir*, vol. 18, no. 26, pp. 10486–10488, 2002.
- [102] T. Roques-Carmes, V. Mathieu, and A. Gigante, “Experimental contribution to the understanding of the dynamics of spreading of Newtonian fluids: Effect of volume, viscosity and surfactant,” *J. Colloid Interface Sci.*, 2010.
- [103] N. A. Ivanova and V. M. Starov, “Wetting of low free energy surfaces by aqueous surfactant solutions,” *Curr. Opin. Colloid Interface Sci.*, vol. 16, no. 4, pp. 285–291, 2011.
- [104] A.-L. Biance, C. Clanet, and D. Quéré, “First steps in the spreading of a liquid droplet,” *Phys. Rev. E*, vol. 69, no. 1, p. 016301, Jan. 2004.
- [105] J. C. Bird, S. Mandre, and H. A. Stone, “Short-time dynamics of partial wetting,” *Phys. Rev. Lett.*, vol. 100, no. 23, 2008.
- [106] A. Eddi, K. G. Winkels, and J. H. Snoeijer, “Short time dynamics of viscous drop spreading,” *Phys. Fluids*, 2013.
- [107] S. Mitra and S. K. Mitra, “Understanding the Early Regime of Drop Spreading,” *Langmuir*, 2016.
- [108] M. J. De Ruijter, M. Charlot, M. Voué, and J. De Coninck, “Experimental evidence of several time scales in drop spreading,” *Langmuir*, vol. 16, no. 5, pp. 2363–2368, 2000.
- [109] M. a. Cazabat, A. M., Cohen Stuart, “Dynamics of Wetting: Effects of Surface Roughness,” *J. Phys. Chem.*, 1986.
- [110] L. Chen, G. K. Auernhammer, and E. Bonaccorso, “Short time wetting dynamics on soft surfaces,” *Soft Matter*, 2011.

- [111] B. K. Primkulov, F. Lin, and Z. Xu, “Microscale liquid-liquid displacement dynamics: Molecular kinetic or hydrodynamic control,” *Colloids Surfaces A Physicochem. Eng. Asp.*, vol. 497, pp. 336–343, 2016.
- [112] B. Seed, “Silanizing Glassware,” in *Current Protocols in Immunology*, Hoboken, NJ, USA: John Wiley & Sons, Inc., 2001, p. A.3K.1-A.3K.2.
- [113] A. González-Mancera, V. K. Gupta, M. Jamal, and C. D. Eggleton, “Effects of a surfactant monolayer on the measurement of equilibrium interfacial tension of a drop in extensional flow,” *J. Colloid Interface Sci.*, vol. 333, no. 2, pp. 570–578, 2009.
- [114] U. Farooq, N. Asif, M. T. Tweheyo, J. Sjöblom, and G. Øye, “Effect of low-saline aqueous solutions and pH on the desorption of crude oil fractions from silica surfaces,” *Energy and Fuels*, 2011.
- [115] G. Sauerbrey, “Verwendung von Schwingquarzen zur Waegung duenner Schichten und zur Mikrowaegung,” *Zeitschrift fuer Phys.*, vol. 155, no. 2, pp. 206–222, 1959.
- [116] A. Yeung, T. Dabros, J. Czarnecki, and J. Masliyah, “On the interfacial properties of micrometre-sized water droplets in crude oil,” *Proc. R. Soc. London Ser. A Math. Phys. Eng. Sci.*, vol. 455, no. 1990, pp. 3709–3723, 1999.
- [117] T. Zhao and L. Jiang, “Contact angle measurement of natural materials,” *Colloids Surfaces B Biointerfaces*, 2018.
- [118] A. Bateni, S. S. Susnar, A. Amirfazli, and A. W. Neumann, “A high-accuracy polynomial fitting approach to determine contact angles,” *Colloids Surfaces A Physicochem. Eng. Asp.*, 2003.
- [119] G. Bracco and B. Holst, *Surface science techniques*. Berlin: New York : Springer, 2013.
- [120] M. Hoorfar and A. W. Neumann, “Recent progress in Axisymmetric Drop Shape Analysis (ADSA),” *Advances in Colloid and Interface Science*. 2006.
- [121] Y. Rotenberg, L. Boruvka, and A. W. Neumann, “Determination of surface tension and contact angle from the shapes of axisymmetric fluid interfaces,” *J. Colloid Interface Sci.*, 1983.
- [122] F. K. Skinner, Y. Rotenberg, and A. W. Neumann, “Contact angle measurements from the

- contact diameter of sessile drops by means of a modified axisymmetric drop shape analysis,” *J. Colloid Interface Sci.*, 1989.
- [123] A. Kalantarian, R. David, and A. W. Neumann, “Methodology for high accuracy contact angle measurement,” *Langmuir*, 2009.
- [124] A. Bateni, S. S. Susnar, A. Amirfazli, and A. W. Neumann, “Development of a new methodology to study drop shape and surface tension in electric fields,” *Langmuir*, 2004.
- [125] S. F. Chini and A. Amirfazli, “A method for measuring contact angle of asymmetric and symmetric drops,” *Colloids Surfaces A Physicochem. Eng. Asp.*, 2011.
- [126] Z. N. Xu, “A static contact angle algorithm for silicone rubber aging experiments,” *IEEE Trans. Power Deliv.*, 2013.
- [127] A. Fitzgibbon, M. Pilu, and R. B. Fisher, “Direct least square fitting of ellipses,” *IEEE Trans. Pattern Anal. Mach. Intell.*, 1999.
- [128] E. Atefi, J. A. Mann, and H. Tavana, “A robust polynomial fitting approach for contact angle measurements,” *Langmuir*, vol. 29, no. 19, pp. 5677–5688, 2013.
- [129] M. G. Cabezas, A. Bateni, J. M. Montanero, and A. W. Neumann, “A new drop-shape methodology for surface tension measurement,” in *Applied Surface Science*, 2004.
- [130] R. Fisher, S. Perkins, A. Walker, and E. Wolfart, “Hypermedia image processing reference,” *Dep. Artif. Intell. Univ. Edinburgh*, 1997.
- [131] N. Otsu, “A Threshold Selection Method from Gray-Level Histograms,” *IEEE Trans. Syst. Man. Cybern.*, 1979.
- [132] A. Mohammad Karim and H. P. Kavehpour, “Effect of viscous force on dynamic contact angle measurement using Wilhelmy plate method,” *Colloids Surfaces A Physicochem. Eng. Asp.*, vol. 548, pp. 54–60, Jul. 2018.
- [133] P. Xing, M. Bousmina, D. Rodrigue, and M. R. Kamal, “Critical experimental comparison between five techniques for the determination of interfacial tension in polymer blends: model system of polystyrene/polyamide-6,” *Macromolecules*, 2000.
- [134] A. Luciani, M. F. Champagne, and L. A. Utracki, “Interfacial tension coefficient from the retraction of ellipsoidal drops,” *J. Polym. Sci. Part B Polym. Phys.*, 1997.

- [135] C. J. Carriere and A. Cohen, "Evaluation of the interfacial tension between high molecular weight polycarbonate and PMMA resins with the imbedded fiber retraction technique," *J. Rheol. (N. Y. N. Y.)*, 1991.
- [136] A. Cohen and C. J. Carriere, "Analysis of a retraction mechanism for imbedded polymeric fibers," *Rheol. Acta*, 1989.
- [137] J. M. Rallison, "The Deformation of Small Viscous Drops and Bubbles in Shear Flows," *Annu. Rev. Fluid Mech.*, vol. 16, no. 1, pp. 45–66, Jan. 1984.
- [138] S. Guido and M. Villone, "Measurement of Interfacial Tension by Drop Retraction Analysis," *J. Colloid Interface Sci.*, vol. 209, no. 1, pp. 247–250, 1999.
- [139] J. Martin and S. Velankar, "Interfacial tension errors from the cohen and carriere analysis of imbedded fiber retraction," *Macromolecules*, 2005.
- [140] C. Pozrikidis, "Interfacial Dynamics for Stokes Flow," *J. Comput. Phys.*, 2001.
- [141] L. G. Leal and H. A. Stone, "Relaxation and breakup of an initially extended drop in an otherwise quiescent fluid," *J. Fluid Mech.*, 1989.
- [142] M. Tjahjadi, J. M. Ottino, and H. A. Stone, "Estimating interfacial tension via relaxation of drop shapes and filament breakup," *AIChE J.*, 1994.
- [143] V. Cristini, J. Blawdziewicz, and M. Loewenberg, "An Adaptive Mesh Algorithm for Evolving Surfaces: Simulations of Drop Breakup and Coalescence," *J. Comput. Phys.*, 2001.
- [144] P. D. Patel, E. S. G. Shaqfeh, J. E. Butler, V. Cristini, J. Bławdziewicz, and M. Loewenberg, "Drop breakup in the flow through fixed fiber beds: An experimental and computational investigation," *Phys. Fluids*, 2003.
- [145] R. Tran-Son-Tay, D. Needham, A. Yeung, and R. M. Hochmuth, "Time-dependent recovery of passive neutrophils after large deformation," *Biophys. J.*, 1991.
- [146] K. Moran, A. Yeung, and J. Masliyah, "Shape relaxation of an elongated viscous drop," *J. Colloid Interface Sci.*, vol. 267, no. 2, pp. 483–493, 2003.
- [147] J. Happel and H. Brenner, *Low Reynolds Number Hydrodynamics*. 1983.
- [148] T. P. Yin, "Kinetics of spreading," *J. Phys. Chem.*, vol. 73, no. 7, pp. 2413–2417, Jul. 1969.

- [149] L. M. Hocking, “A moving fluid interface. Part 2. The removal of the force singularity by a slip flow,” *J. Fluid Mech.*, vol. 79, no. 02, p. 209, Feb. 1977.
- [150] J. Den Chen, “Experiments on a spreading drop and its contact angle on a solid,” *J. Colloid Interface Sci.*, vol. 122, no. 1, pp. 60–72, 1988.
- [151] M. Kanungo, S. Mettu, K. Y. Law, and S. Daniel, “Effect of roughness geometry on wetting and dewetting of rough PDMS surfaces,” *Langmuir*, vol. 30, no. 25, pp. 7358–7368, 2014.
- [152] M. Ramiasa, J. Ralston, R. Fetzer, and R. Sedev, “Nanoroughness impact on liquid-liquid displacement,” *J. Phys. Chem. C*, vol. 116, no. 20, pp. 10934–10943, 2012.
- [153] R. A. Hayes and J. Ralston, “The dynamics of wetting processes,” *Colloids Surfaces A Physicochem. Eng. Asp.*, vol. 93, no. C, pp. 15–23, 1994.
- [154] B. Lavi and A. Marmur, “The exponential power law: Partial wetting kinetics and dynamic contact angles,” in *Colloids and Surfaces A: Physicochemical and Engineering Aspects*, 2004, vol. 250, no. 1-3 SPEC. ISS., pp. 409–414.
- [155] C. W. Extrand, “Spontaneous Spreading of Viscous Liquid Drops,” *J. Colloid Interface Sci.*, vol. 157, no. 1, pp. 72–76, 1993.
- [156] C. Liu, E. Bonaccorso, M. Sokuler, K. A. Günter, and H. J. Butt, “Dynamic wetting of polyisoprene melts: Influence of the end group,” *Langmuir*, vol. 26, no. 4, pp. 2544–2549, 2010.
- [157] Y. D. Shikhmurzaev, “Spreading of drops on solid surfaces in a quasi-static regime,” *Phys. Fluids*, vol. 9, no. 2, pp. 266–275, Feb. 1997.
- [158] S. Basu, K. Kandakumar, and H. J. Masliyah, “A study of oil displacement on model surfaces,” *J. Colloid Interface Sci.*, vol. 182, no. 1, pp. 82–94, 1996.
- [159] F. Lin, L. He, B. Primkulov, and Z. Xu, “Dewetting dynamics of a solid microsphere by emulsion drops,” *J. Phys. Chem. C*, vol. 118, no. 25, pp. 13552–13562, 2014.
- [160] E. B. Dussan, E. Rame, and S. Garoff, “on Identifying the Appropriate Boundary-Conditions At a Moving Contact Line - an Experimental Investigation,” *J. Fluid. Mech.*, vol. 230, pp. 97–116, 1991.
- [161] E. Ramé, S. Garoff, and K. R. Willson, “Characterizing the microscopic physics near

- moving contact lines using dynamic contact angle data,” *Phys. Rev. E - Stat. Nonlinear, Soft Matter Phys.*, vol. 70, no. 3 1, 2004.
- [162] M. J. De Ruijter, J. De Coninck, T. D. Blake, a Clarke, and a Rankin, “Contact Angle Relaxation during the Spreading of Partially Wetting Drops,” *Langmuir*, vol. 13, no. 26, pp. 7293–7298, 1997.
- [163] Z. N. Xu and S. Y. Wang, “A highly accurate dynamic contact angle algorithm for drops on inclined surface based on ellipse-fitting,” *Rev. Sci. Instrum.*, vol. 86, no. 2, 2015.
- [164] R. Fetzer and J. Ralston, “Dynamic dewetting regimes explored,” *J. Phys. Chem. C*, vol. 113, no. 20, pp. 8888–8894, 2009.
- [165] P.-G. de Gennes, F. Brochard-Wyart, and D. Quere, *Capillarity and Wetting Phenomena Drops, Bubbles, Pearls, Waves*. 2004.
- [166] H. Li, R. Sedev, and J. Ralston, “Dynamic wetting of a fluoropolymer surface by ionic liquids,” *Phys. Chem. Chem. Phys.*, vol. 13, no. 9, p. 3952, 2011.
- [167] Y. Suo, K. Stoev, S. Garoff, and E. Ramé, “Hydrodynamics and contact angle relaxation during unsteady spreading,” *Langmuir*, vol. 17, no. 22, pp. 6988–6994, 2001.
- [168] J. G. Petrov, J. Ralston, M. Schneemilch, and R. A. Hayes, “Dynamics of Partial Wetting and Dewetting in Well-Defined Systems,” *J. Phys. Chem. B*, vol. 107, no. 7, pp. 1634–1645, Feb. 2003.
- [169] K. S. Lee, N. Ivanova, V. M. Starov, N. Hilal, and V. Dutschk, “Kinetics of wetting and spreading by aqueous surfactant solutions,” *Advances in Colloid and Interface Science*, vol. 144, no. 1–2, pp. 54–65, 2008.
- [170] A. W. Rowe, R. M. Counce, S. A. Morton, M. Z.-C. Hu, and D. W. DePaoli, “Oil Detachment from Solid Surfaces in Aqueous Surfactant Solutions as a Function of pH,” *Ind. Eng. Chem. Res.*, vol. 41, no. 7, pp. 1787–1795, Apr. 2002.
- [171] V. L. Kolev, I. I. Kochijashky, K. D. Danov, P. A. Kralchevsky, G. Broze, and A. Mehreteab, “Spontaneous detachment of oil drops from solid substrates: Governing factors,” *J. Colloid Interface Sci.*, 2003.
- [172] S. Tcholakova *et al.*, “Efficient emulsification of viscous oils at high drop volume fraction,”

Langmuir, 2011.

- [173] L. Thompson, “The role of oil detachment mechanisms in determining optimum detergency conditions,” *J. Colloid Interface Sci.*, 1994.
- [174] J. C. Lapez-Montilla, P. E. Herrera-Morales, S. Pandey, and D. O. Shah, “Spontaneous emulsification: Mechanisms, physicochemical aspects, modeling, and applications,” *J. Dispers. Sci. Technol.*, 2002.
- [175] I. Reviakine, D. Johannsmann, and R. P. Richter, “Hearing what you cannot see and visualizing what you hear: Interpreting quartz crystal microbalance data from solvated interfaces,” *Anal. Chem.*, vol. 83, no. 23, pp. 8838–8848, 2011.
- [176] P. Li and M. Ishiguro, “Adsorption of anionic surfactant (sodium dodecyl sulfate) on silica,” *Soil Sci. Plant Nutr.*, vol. 62, no. 3, pp. 223–229, 2016.
- [177] R. Ghosh Chaudhuri and S. Paria, “Effect of electrolytes on wettability of glass surface using anionic and cationic surfactant solutions,” *J. Colloid Interface Sci.*, 2014.
- [178] D. M. Nevskaja, M. L. R. Cervantes, A. G. Ruíz, and J. de Dios López González, “Interaction of triton X-100 on silica: A relationship between surface characteristics and adsorption isotherms,” *J. Chem. Technol. Biotechnol.*, vol. 63, no. 3, pp. 249–256, 1995.
- [179] F. Tiberg, “Physical characterization of non-ionic surfactant layers adsorbed at hydrophilic and hydrophobic solid surfaces by time-resolved ellipsometry,” *J. Chem. Soc. Faraday Trans.*, vol. 92, no. 4, p. 531, 1996.
- [180] P. Somasundaran and S. Krishnakumar, “Adsorption of surfactants and polymers at the solid-liquid interface,” *Colloids Surfaces A Physicochem. Eng. Asp.*, vol. 123–124, pp. 491–513, 1997.
- [181] J. Brinck, B. Jönsson, and F. Tiberg, “Kinetics of Nonionic Surfactant Adsorption and Desorption at the Silica–Water Interface: One Component,” *Langmuir*, vol. 14, no. 12, pp. 1058–1071, 1998.
- [182] G. Gonzalez and A. M. Travalloni-Louvisse, “The effect of triton X-100 and ethanol on the wettability of quartz,” *Langmuir*, vol. 5, no. 1, pp. 26–29, Jan. 1989.
- [183] A. Zdziennicka, K. Szymczyk, and B. Jańczuk, “Correlation between surface free energy of

- quartz and its wettability by aqueous solutions of nonionic, anionic and cationic surfactants,” *J. Colloid Interface Sci.*, vol. 340, no. 2, pp. 243–248, 2009.
- [184] V. Gonzalez and S. E. Taylor, “Asphaltene adsorption on quartz sand in the presence of pre-adsorbed water,” *J. Colloid Interface Sci.*, vol. 480, pp. 137–145, 2016.
- [185] M. L. Chacón-Patiño, C. Blanco-Tirado, J. A. Orrego-Ruiz, A. Gómez-Escudero, and M. Y. Combariza, “High resolution mass spectrometric view of asphaltene-SiO₂ interactions,” *Energy and Fuels*, vol. 29, no. 3, pp. 1323–1331, 2015.
- [186] K. Kumar, E. Dao, and K. Mohanty, “Atomic Force Microscopy Study of Wettability Alteration by Surfactants,” *SPE J.*, 2008.
- [187] S. Ren, T. Dang-Vu, H. Zhao, J. Long, Z. Xu, and J. Masliyah, “Effect of weathering on surface characteristics of solids and bitumen from oil sands,” *Energy and Fuels*, 2009.
- [188] A. Karimi *et al.*, “Wettability alteration in carbonates using zirconium oxide nanofluids: EOR implications,” *Energy and Fuels*, vol. 26, no. 2, pp. 1028–1036, 2012.
- [189] W. Liu, Y. Jin, X. Tan, and A. Yeung, “Altering the wettability of bitumen-treated glass surfaces with ionic surfactants,” *Fuel*, 2011.
- [190] S. K. Harjai, C. Flury, J. Masliyah, J. Drelich, and Z. Xu, “Robust aqueous-nonaqueous hybrid process for bitumen extraction from mineable athabasca oil sands,” in *Energy and Fuels*, 2012.
- [191] Y. Zhu, C. Yan, Q. Liu, J. H. Masliyah, and Z. Xu, “Biodiesel-Assisted Ambient Aqueous Bitumen Extraction (BA3BE) from Athabasca Oil Sands,” *Energy and Fuels*, 2018.
- [192] A. Vrij, “Possible mechanism for the spontaneous rupture of thin, free liquid films,” *Discussions of the Faraday Society*. 1966.
- [193] E. Ruckenstein and R. Jain, “Spontaneous rupture of thin liquid films,” *J. Chem. Soc. Faraday Trans. 2 Mol. Chem. Phys.*, 1974.
- [194] R. G. Smith and L. L. Schramm, “The influence of mineral components on the generation of natural surfactants from Athabasca oil sands in the alkaline hot water process,” *Fuel Process. Technol.*, 1992.
- [195] L. He, F. Lin, X. Li, H. Sui, and Z. Xu, “Interfacial sciences in unconventional petroleum

production: from fundamentals to applications,” *Chem. Soc. Rev.*, 2015.

- [196] J. Anderson, S. B. Wiseman, A. Moustafa, M. Gamal El-Din, K. Liber, and J. P. Giesy, “Effects of exposure to oil sands process-affected water from experimental reclamation ponds on *Chironomus dilutus*,” *Water Res.*, 2012.